Rare-earth ion doped planar waveguides for integrated quantum photonics

Sara Marzban

A thesis submitted for the degree of
Doctor of Philosophy at
The Australian National University

January 2018

Declaration

This thesis is based on research undertaken at the Laser Physics Center, Research School of Physics and Engineering, The Australian National University, Canberra, Australia.

Except where otherwise indicated in the customary manner, the material presented in this thesis is, to the best of my knowledge, my own original work, and has not been submitted for another degree at any other institution or university.

January 2018

To my dearest mum and dad, Farzaneh Marzbanrad and Hussein Marzban, thank you for all your love and support.

Acknowledgments

I traveled a long way from Shiraz to Canberra for a Master of Engineering degree at the ANU in 2009. A friend of mine suggested we take the PHYS3031, the atomic physics course as one of our electives. I was really terrified and excited at the thought of taking an entirely new subject. The lecturers of the course were Professor Hans Bachor and Associate Professor Matthew Sellars. This is how I met Matt, a wonderful teacher and mentor. I really owe a great deal of thanks to Matt for trusting in my ability and giving me the opportunity to be his PhD student. Matt is an inspirational scientist and a wonderful person. He has guided and encouraged me through this long and sometimes difficult journey, and I truly appreciate all his support.

I would like to thank Dr Khu Vu for all his help with the thin film fabrication and for being there when ever I had any trouble or needed any help. His enthusiasm to make the thin films work and his excitement when it finally worked was really inspiring. I would also like to thank Dr Steve Madden for all the productive conversations we had about the thin film fabrication and other fabrication issues. Steve always had ideas about things I hadn't tried and suggested solutions when I was stuck.

I would also like to acknowledge the technical assistance of Mr John Botega and Mr Craig Macleod from the Laser Physics Center for all their support. I really appreciated their patience and assistance with making all the strange contraptions I needed during my work.

I would like to acknowledge the help of all the technical staff at the ANFF lab. Dr Fouad Karouta, Dr Kaushal Vora and specially Dr Li Li, who sat with me while we tried to figure out how to write a program for the FIB to write my gratings.

I would also like to thank the incredible people I've worked with at the Solid-State Spectroscopy group over the years, specially Dr John Bartholomew. He has helped me so much over the course of my PhD and I am so indebted to him. I had no experience in an optical spectroscopy lab, and John patiently answered all my questions and helped me learn so much. He is an incredible human being, always happy to lend a hand. I would also like to thank Professor Neil Manson and Dr

Marcus Doherty for their kindness and the wonderful conversations we have had through the years. I would like to acknowledge the rest of the group both past and present, Dr Morgan Hedges, Dr Sarah Beavan, Dr Rose Ahlefeldt, Dr Kate Ferguson, Manjin Zhong and Milos Rancic. I'd specially like to thank Kate and Rose for proof reading this work, I'm very grateful to you both. Members of this wonderful group have all been so friendly and welcoming, which is really important for an international student so far away from home and family.

I would also like to thank everyone else at the Laser Physics Center, I have enjoyed so many wonderful and sometimes weird conversations with them over tea and am so grateful for all their support.

This was my first experience living away from home, and I found out that it can be very lonely if you don't have the right group of people around you. I have to thank all my friends at Graduate House which has been my home for the last 7 years. They have always been really kind and caring and were there for me whenever I needed help or just to talk and complain about our PhDs!

My dear mum and dad, Farzaneh and Hussein, and my lovely sister and brother, Bahareh and Reza, I owe everything I have achieved to you. For all your unconditional love, support and encouragement over the years, I am eternally thankful. You have always believed in me and inspired me to be a better person and achieve my dreams. I am so lucky and blessed to have you in my life.

Lastly, I have always had faith in God and believed that he will help and guide me through life. We are now more and more beginning to see the universe as interlinked and intertwined. As the poet Sa'adi Shirazi from my home town has said about 700 years ago, "I am happy with the One whom the world is happy with, I am in love with the whole universe as the whole universe is in love with Him."

Abstract

This thesis presents a spectroscopic study of Pr^{3+} ions in a novel passive waveguide architecture. To make this structure, the high refractive glass TeO_2 was selected as the thin film and it was deposited on a Pr^{3+}:Y_2SiO_5 crystal. In this waveguide, the ${}^3H_4 \rightarrow {}^1D_2$ transition of Pr^{3+} ions were probed by the optical evanescent field extending into the substrate. The main concern in assessing the suitability of this material for quantum information applications was ensuring that the coherence properties of rare-earth ions, making them suitable for quantum information purposes, are preserved in this architecture. After which, to make low loss devices with these waveguides, efficient coupling techniques had to be developed.

To prove that the coherence properties of the rare-earth ion doped crystal were preserved, the critical parameters of inhomogeneous linewidth, the absorption of the ions, the coherence time and spin lifetimes of the Pr^{3+} ions were studied. The inhomogeneous linewidth of evanescent coupled ions was 10.0 ± 0.1 GHz, which was consistent with the linewidth of bulk samples with the same Pr^{3+} doping concentration [1]. The absorption due to the evanescent coupling was 9.38 dB, approximately 90% of what was expected with respect to the bulk crystal with the same doping concentration. Therefore, despite using the evanescent field, the absorption is high enough for quantum memory applications.

An optical coherence time (T_2) of 121 ± 1 μs was measured, which corresponded to a homogeneous linewidth of 2.6 ± 0.3 kHz. This is very close to bulk sample measurements of 111 ± 4 μs [2], with the same temperature and doping concentration. The spin state lifetime observed was about 9.8 ± 0.3 s, which is also very close to the bulk sample measurement of 8.67 s [3].

Initial Stark shifting experiments were performed to determine whether the active ions in the substrate of the passive waveguides could be electrically controlled by applying a small voltage to electrodes on the thin film. In these experiments with a voltage change of 100 mV, the measured holewidth broadening was increased by about 0.55 ± 0.2 MHz, which was similar to the calculated values of 0.45 ± 0.1 MHz. The Stark coefficient for site 1 was 51.6 ± 0.05 kHz/(V cm $^{-1}$) [4] along the D_2 axis of the crystal (site 1 will be explained in Section 4.3).

Prism coupling and grating coupling were used to couple light to the ions in the

substrate. Prism coupling is an easy and quick method to couple light into a waveguide and observe the properties of the system. However, grating coupling is much more practical when moving towards building a device using this method.

The measurements described above indicated that the properties of ions interacting with the evanescent tail of the waveguide mode were consistent with those of bulk ions. This investigation also showed that depositing a glass thin film on a rare-earth ion doped crystal did not affect the good coherence properties of the substrate. These results establish the foundation for large, integrated, controllable and high performance rare earth ion quantum waveguide systems.

Contents

Declaration iii

Acknowledgments v

Abstract vii

1 Introduction 1

1.1 Quantum communication . . . 1

1.1.1 Quantum repeater . . . 1

1.2 Rare-earth ion doped waveguides . . . 5

1.3 Thesis Outline . . . 9

2 Background Theory 11

2.1 Introduction . . . 11

2.2 Rare-earth ion doped crystals . . . 11

2.2.1 Intrinsic Hamiltonian . . . 13

2.2.1.1 Free ion Hamiltonian . . . 14

2.2.1.2 Crystal field Hamiltonian . . . 14

2.2.1.3 Magnetic hyperfine Hamiltonian . . . 15

2.2.1.4 Stark shift . . . 16

2.3 Broadening mechanisms . . . 16

2.3.1 Homogeneous broadening . . . 17

2.3.2 Inhomogeneous broadening . . . 19

2.3.3 Spectral diffusion . . . 20

2.3.4 Hyperfine broadening . . . 21

2.4 Spectroscopic techniques for studying broadening . . . 22

2.4.1 Spectral holeburning . . . 22

2.4.2 Coherent light-atom interactions . . . 23

2.4.2.1 Bloch vector description . . . 24

2.4.2.2 Coherent transients . . . 27

2.5 Observation of broadening associated with disorder in bulk samples . 32

2.5.1 TLS effect on disordered rare-earth crystals . . . 32

2.5.2 Intrinsic disorder of $LiNbO_3$ . . . 34

2.6 Broadening mechanisms in waveguides . . . 35
2.7 Linear coherent quantum memory techniques . . . 38
2.7.1 Photon echo based quantum memories . . . 39
2.7.1.1 Atomic Frequency Comb . . . 39
2.7.1.2 Controlled Reversible Inhomogeneous Broadening . . . 41
2.7.1.3 Rephased amplified spontaneous emission quantum memory . . . 43
2.7.2 Quantum memories using rare-earth ion doped waveguides . . . 45
2.8 Summary . . . 46

3 Proposed Linear Optics Quantum Processor Architecture 49
3.1 Introduction . . . 49
3.2 Waveguide design . . . 52
3.3 Time scale of operations . . . 53
3.4 Electronic control . . . 54
3.5 Elements of linear optical quantum processor chip . . . 55
3.5.1 Single photon source . . . 55
3.5.2 Quantum memories . . . 57
3.5.3 Passive elements . . . 58
3.5.4 Single photon detectors . . . 59
3.6 Summary . . . 59

4 Material Complexities and Fabrication of Rare-Earth Planar Waveguides 61
4.1 Introduction . . . 61
4.2 Thin films with rare-earth doped crystal as active core . . . 62
4.2.1 Eu^{3+}:Y_2O_3 . . . 63
4.2.2 Eu^{3+}:Y_2O_3 thin films . . . 63
4.2.2.1 Thin film growth method and results . . . 64
4.3 Thin films with rare-earth doped crystal as active substrate . . . 69
4.3.1 Pr^{3+}:Y_2SiO_5 . . . 69
4.3.2 TeO_2 thin films on Pr^{3+}:Y_2SiO_5 substrates . . . 72
4.4 Deposition of electrodes on TeO_2 thin films . . . 74
4.5 Summary . . . 75

5 Waveguide and Electrode Design 77
5.1 Introduction . . . 77
5.2 Waveguide theory . . . 78
5.3 Coupling methods . . . 83

5.3.1 Prism coupling . . . 84
5.3.2 Grating coupling . . . 87
5.3.2.1 Eigenmode expansion method . . . 90
5.3.2.2 Gaussian beams . . . 91
5.4 Design of electrodes on thin films . . . 92
5.5 Summary . . . 96

6 Waveguide Characterization and Experiments 97
6.1 Introduction . . . 97
6.2 Prism coupling . . . 98
6.2.1 Experimental setup . . . 98
6.2.2 Inhomogeneous profile of 0.005%Pr^{3+}:Y_2SiO_5 substrate . . . 99
6.2.3 Homogeneous profile of 0.005%Pr^{3+}:Y_2SiO_5 substrate . . . 101
6.2.4 Spin state lifetime of 0.005%Pr^{3+}:Y_2SiO_5 substrate . . . 103
6.3 Experimental setup for grating coupling . . . 105
6.3.1 Cold finger cryostat . . . 105
6.3.2 Thin film holder . . . 106
6.4 Grating coupling . . . 108
6.4.1 Writing binary gratings on TeO_2 thin film surface . . . 108
6.4.2 Performance of gratings . . . 111
6.4.3 Experimental setup . . . 113
6.4.4 Inhomogeneous profile of 0.05%Pr^{3+}:Y_2SiO_5 substrate . . . 114
6.4.5 Homogeneous profile of 0.05%Pr^{3+}:Y_2SiO_5 substrate . . . 116
6.4.6 Spin state lifetime of 0.05%Pr^{3+}:Y_2SiO_5 substrate . . . 118
6.5 Stark shift effect and electronic control . . . 120
6.6 Summary . . . 123

7 Discussion 125
7.1 Grating coupling efficiency . . . 129
7.2 Electronic control . . . 132

8 Conclusion 135

Bibliography 137

Chapter 1

Introduction

1.1 Quantum communication

In this era of on-line communications, the security of transmitted and received information is extremely important. Quantum communication is an absolutely secure method of communication between points A and B. However, building these secure quantum communication networks has proven to be difficult. In a quantum communication network, fragile quantum states are transmitted between a transmitter (point A) and a receiver (point B). During transmission, decoherence can be introduced into the system, either from losses in the transmission line, absorption in the system or from environmental contamination. Some of the losses occurring over the full length of the transmission line scale exponentially with distance and as a consequence, quantum communication is restricted to a range of about 200 km, beyond which quantum states can no longer be reliably measured [5, 6].

In the classical communication network, the problem of loss in the transmission line is resolved by placing amplifiers along the transmission line. Due to the no-cloning theorem, which states that it is impossible to create identical copies of unknown quantum states [7], it is not possible to simply amplify quantum information. Therefore, a quantum repeater protocol is used, which is able to establish entanglement between two quantum states that are spatially separated. The quantum repeater protocol and its essential components are explained in more detail in Section 1.1.1.

1.1.1 Quantum repeater

The"quantum repeater" protocol was initially proposed by Briegel *et al.* [8] in 1998. The protocol is based on dividing the transmission channel into many parts in such a way that the length of each division provides a high probability of transmission.

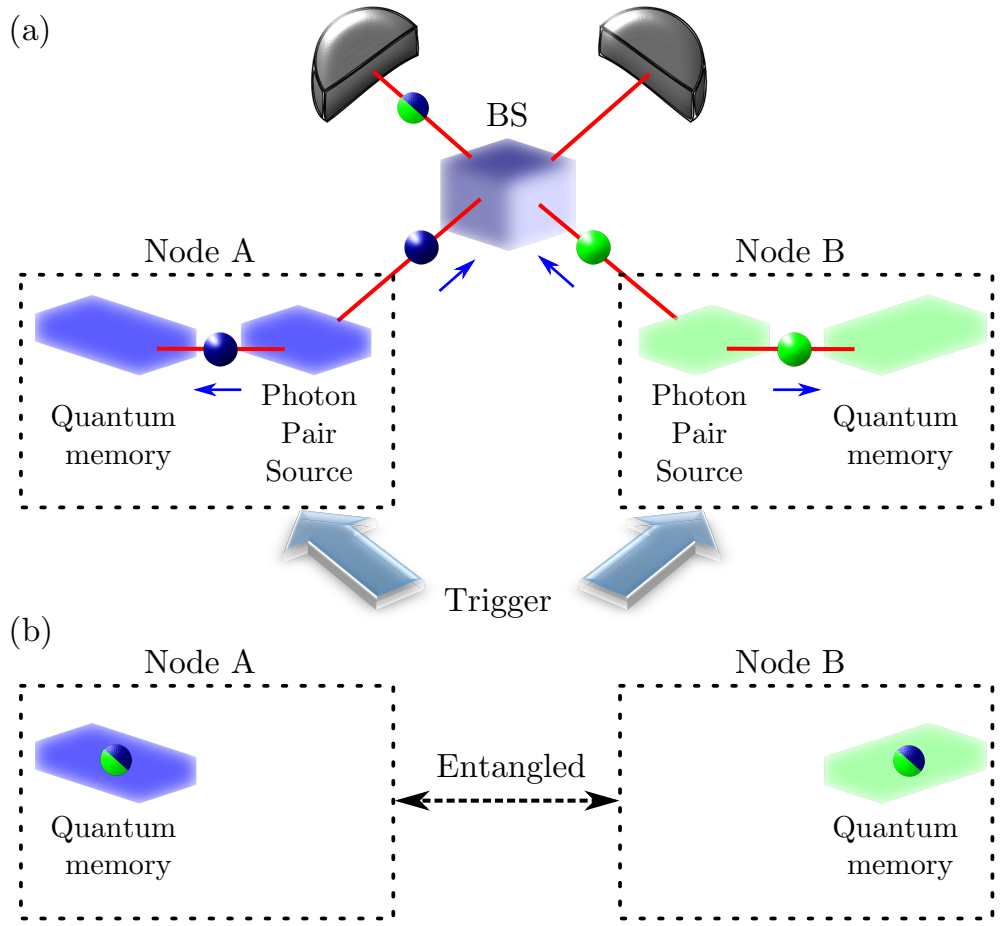

Figure 1.1: Basis of operation of a quantum repeater scheme. An entangled state is generated and shared between the two ends of the communication link. The link is divided into smaller parts, where each part has a photon source and a quantum memory. (a) Entanglement is established between two neighboring nodes. (b) Node A and node B are entangled, with the entangled state stored in the respective quantum memories.

A quantum repeater distributes entanglement across the network, allowing a state to be teleported from one side to the other without actually having to transmit the quantum state down the full length of the fiber. In this scheme, the creation of entanglement results from an interference and measurement operation. A simplified illustration of this method is shown in Figures 1.1 and 1.2. In these figures, BS is a beam splitter.

Each node in a quantum repeater contains an entangled light source and a quantum memory. To explain the protocol in more detail, as is observed in Figure 1.1, the two photon generators at the neighboring nodes of A and B are simultaneously triggered [6]. Each node has a local quantum memory which stores one of the two generated photons, while the other photon travels through a 50 : 50 beam-splitter.

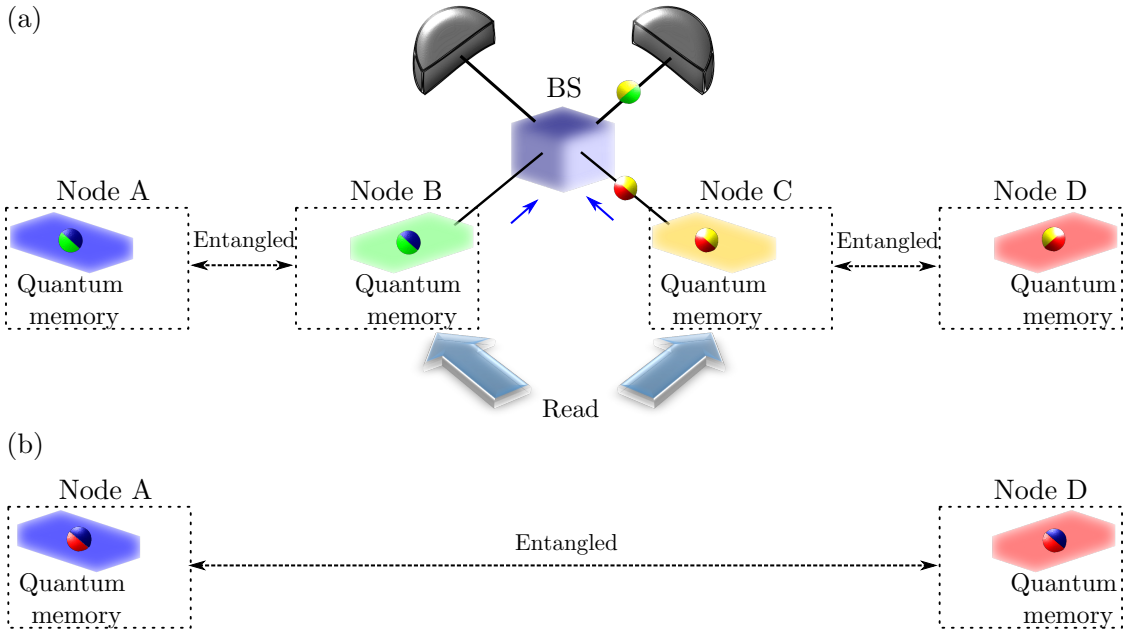

Figure 1.2: (a) Measurements are performed in a way such that the entanglement is swapped. (b) The entangled state is then shared between nodes that are further apart. This process is repeated until the entanglement is shared between the two ends of the link.

The probability of photon generation from each of the photon sources in the nodes is very small, therefore most of the time there are no photons detected. When a single photon is detected, it means that the pair of this generated photon is stored in one of the quantum memories of the neighboring nodes. But, since it is not possible to know which photon source generated the detected photon, it is not known which quantum memory is storing the pair photon. Hence, the single quantum state is spread throughout the neighboring node quantum memories, resulting in entanglement- via- indistinguishability.

Once entanglement has been generated in two neighboring links (A-B and C-D), it can be built up across the channel using entanglement swapping. Entanglement swapping is simply illustrated in Figure 1.2. In this part of the protocol, the quantum memories at two nodes which were not entangled together are read out at the same time, and again the detector cannot distinguish between the memories. In this situation, a single quantum state is shared between the two neighboring nodes, for example of nodes A and B, and also nodes C and D. When the two non-neighboring nodes of B and C are read out at the same time, the result can be zero, one or two photons.

If no photons are detected, then both of the photons must be in quantum memories of A and D. If two photons are detected, then both quantum memories

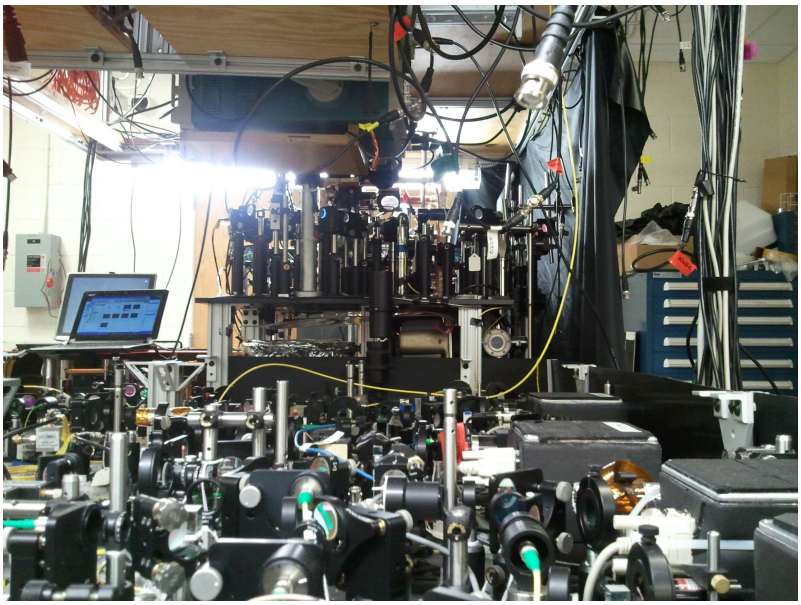

Figure 1.3: A photo representative of current quantum information implementations in photonic materials, using an entire table's worth of optical elements [9].

of A and D must be empty. In both of these cases, the entanglement swapping has failed and the generation of entanglement between the first nodes has to be repeated. However, if a single photon is detected, then there is one quantum state left in one of the memories. This remaining photon is either in the quantum memory of node A or node D. However, because there is no way of distinguishing which memory is holding the quanta of excitation, once again entanglement-via-indistinguishability has been established, in this instance between nodes A and D. This method of distribution spreads the created entanglement among distant nodes and ultimately between the first and last nodes in the transmission line. The quantum memory is an essential part of the quantum repeater protocol. If there was no storage of the quantum state, the generation of entanglement and swapping between nodes must be performed at the same time which is very improbable. Quantum memories with long storage times are required to hold the information until the whole entanglement is established, and the minimum time this is going to take is on the order of the transmission time.

To achieve high bandwidths and efficient quantum repeater circuits, the quantum repeater consists of complex photonic circuitry with many optical devices including entangled photon pair sources, on-demand quantum memories capable of achieving long storage times, optical modulators, optical switches, filters, and so forth. At the moment, these complicated circuits are parts of a bulky bench top setup in laboratories like that shown in Figure 1.3. To develop practical quantum communication circuits, it is necessary to minimize the loss due to coupling in and

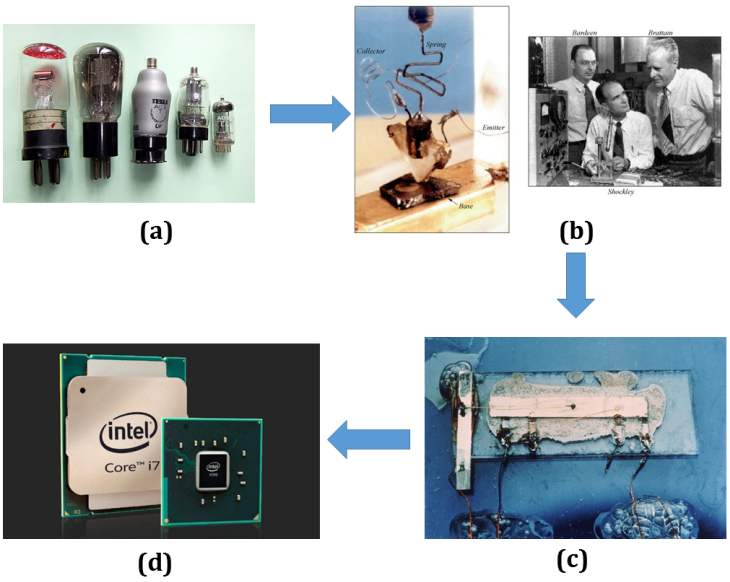

Figure 1.4: (a) Various triode vacuum tubes in chronological order: RE16, REN1004, AC2, 6F5M, EC81 from 1918 (left) to miniature tubes of the 1960s (right), [11], (b) the first point-contact transistor invented in the year 1947 [12], (c) the first working integrated circuit (IC) in the year 1958 [13], (d) The latest Intel Core i7 Extreme Edition is a 52.5 × 45.0 mm IC [10]

out of bulk devices. Therefore, to improve the performance and scalability of the system, it would be beneficial if all these components could be built on a integrated circuit using the same platform.

1.2 Rare-earth ion doped waveguides

Integrating all the required components of a quantum communication network on to the one platform presents a number of challenges similar to that faced by the electronics industry in the 1950s. To obtain the required stability and scalability electronic integrated circuits moved to one platform, the silicon chip, where all the components could be manufactured on a planar structure and all the required operations were performed. This breakthrough unleashed a rapid growth in the capacity of electronic devices that is continuing to this day. Figure 1.4 briefly shows the development of electronic devices. To give an example of this progress, the latest Intel Core i7 Extreme Edition consists of 2.6 billion 22 nm transistors packed in a 52.5 × 45.0 mm integrated circuit [10].

Finding an analogous solid-state platform for integrated quantum communication devices, where all the required operations can be performed, is a key issue

for the field. As quantum memories are an essential component for quantum communications, it is worth looking at systems that have the potential for solid-state quantum memories. To date, the only solid state systems with the long coherence times required for practical quantum repeaters are the rare-earth crystals [6, 14, 15]. As the memory is a core component of the repeater it will be necessary to investigate the fabrication of rare-earth waveguides and incorporate the rare-earth doped crystals into the integrated quantum communication platform.

A variety of materials have been suggested as the platform for quantum integrated circuits, including electro-optical crystals such as Lithium Niobate [16, 17] and rare-earth ion doped crystals such as YAG in lasers [18], but there hasn't yet been a demonstration of a complete integrated quantum photonic device with all the required components for a particular operation.

An appealing system for constructing a complete quantum communication integrated circuit consists of ensembles of rare-earth ion optical centers in a transparent rare-earth crystal. These crystals have a unique property where light can be strongly coupled to densely packed ions in the structure, while the ions are isolated from environmental perturbations. This results in strong coupling to the ensemble and leads to long coherence times on the optical and hyperfine transitions, long storage times [6, 15] and low loss compared to other solid state platforms [14].

Rare-earth ion waveguide systems have been previously fabricated in $LiNbO_3$ using proton-exchange [19] or Ti^{4+} in-diffusion [16, 17, 20]. A notable accomplishment of this research direction was the achievement of atomic frequency comb (AFC) storage of photon entanglement in a Ti^{4+}:Tm^{3+}:$LiNbO_3$ waveguide [16] and more recently an integrated processor for photonic quantum states [17]. Although this demonstration brings integrated quantum optical devices one step closer to reality, the total efficiency of the system and the storage times have to be significantly increased to build practical devices.

To make best use of the unique properties of rare earths in waveguide systems, it would be advantageous to do two things. First, direct electronic control of the rare-earth ions rather than switching light fields would be beneficial. Second, it would be valuable to disconnect the waveguide fabrication process from the rare-earth ion crystal, separating the challenges of waveguide fabrication from optimizing the optical coherence properties. It would be ideal to focus separately on improving the waveguide, and on optimizing the rare earth material to enhance the quantum memory performance. Therefore, it would be beneficial to have a way of fabricating waveguides that is not dependent on a single rare-earth material in the way that the

experiments presented above are dependent on $LiNbO_3$.

Direct electronic control can be achieved in rare-earth ions using the Stark shift, which can be used to move the transitions in an electric field. This would allow the control of the various components required in an integrated quantum device by fast and local electronic manipulation of rare-earth ion ensembles, bringing the ions in and out of resonance with the laser source rather than modulating this source itself. Furthermore, with the fast switching available in electronic circuits, the ensemble frequency can be Stark shifted quickly with low optical losses.

Using Stark shifts to electrically control the rare earth ions provides a way to create and manipulate quantum waveguide devices. The next question to consider is how suitable waveguides will actually be created. A conceptually simple way of making a waveguide is to grow single crystalline thin films doped with rare-earth ions on lower refractive index substrates to form waveguides. However, this shares the same problem as the $LiNbO_3$ waveguides described earlier in that it is difficult to construct a material capable of guiding light that also maintains good optical properties for the rare earth ions it contains. Achieving the desired crystal quality in a sub-wavelength thickness film has proven to be difficult. For example, the 3 μm thick 2%Eu^{3+}:Y_2O_3 film grown by Flinn et al. via metal-organic chemical vapor deposition possessed an inhomogeneous linewidth of 90±20 GHz and a homogeneous linewidth of 12.1 MHz [21]. Whereas a 2% bulk sample of the same material has an inhomogeneous linewidth of 8 GHz and a homogeneous linewidth of 760 Hz [22]. To date, there has been no report of a successfully grown rare-earth ion doped thin film with properties approaching the bulk.

In this thesis, I investigate the possibility of constructing integrated quantum communication devices, with a focus on quantum memories, utilizing rare-earth ion based planar waveguides and electrical control. The two main objectives of this project were, first, to investigate whether it was possible to fabricate waveguiding structures using rare-earth ion doped crystals while preserving the novel coherent properties of these ions and second, to achieve a method of controlling the fabricated device.

In the work presented in this thesis, two planar waveguide systems based on active and passive waveguides were examined. The active planar waveguide involved growing single crystalline rare-earth ion doped thin films on suitable substrates. These thin films were manufactured in-house by Paulraj *et al.* using pulsed laser deposition [23]. The coherent optical properties of the fabricated rare-earth ion thin films were not preserved.

The second approach was to disconnect the waveguide and its fabrication from the rare-earth crystal coherence properties. In this method, passive planar waveguides designed to preserve the coherence properties available in high-quality single crystals were fabricated. Thin films of a high-refractive-index glass were deposited on single crystalline rare-earth ion doped crystal substrates. The optically active rare-earth ions were probed by the evanescent field extending into the substrate as light was guided in the glass thin film. This approach aims to combine the superior properties of rare earth ion dopants in high-quality single crystals with the excellent performance offered by a glass waveguide, the manufacture of which has been well-mastered in the optical communications industry [24]. Also, by depositing electrodes on top of the thin film, electrical control of the ions was achieved.

In the proposed method of this thesis, the rare-earth ion doped crystal is used as the substrate rather than the guiding media. With this method, the expertise and knowledge available in growing high quality single rare-earth ion doped crystals with narrow inhomogeneous lines [25] and long coherence times [14] can be combined with the capability of fabricating high quality waveguides [24]. The other advantage is that the technique is largely sample independent. Any high refractive index glass used as the thin film could be combined with any rare-earth ion doped crystal as the substrate.

There were a few unknown parameters in this configuration. The ions that were probed by the evanescent field were less than about 200 nm from the surface, and it was not known how these ions would behave compared to the bulk ions. Also, the effect of depositing a glass film on the single crystalline material was not clear in terms of static and dynamic strain on the crystal. These factors will be presented throughout the performed experiments.

In addition, we will be investigating increasing the bandwidth of quantum memories using the proposed architecture, through the use of the small size of the device and also the fact that the electrodes, used to Stark shift the excited ions, can be much closer to the active ions as observed in Figure 1.5.

By preserving the rare-earth ion properties in the proposed architecture it can be envisaged that by using this method passive components such as optical filters, switches and modulators, combined with active components such as the high efficiency quantum memory demonstrated by Hedges *et al.* [26], and also single photon sources based on the rephased amplified spontaneous emission (RASE) scheme [27, 28, 29, 30], can be placed on the same chip. This would allow the design of more sophisticated components for quantum repeater or quantum computer

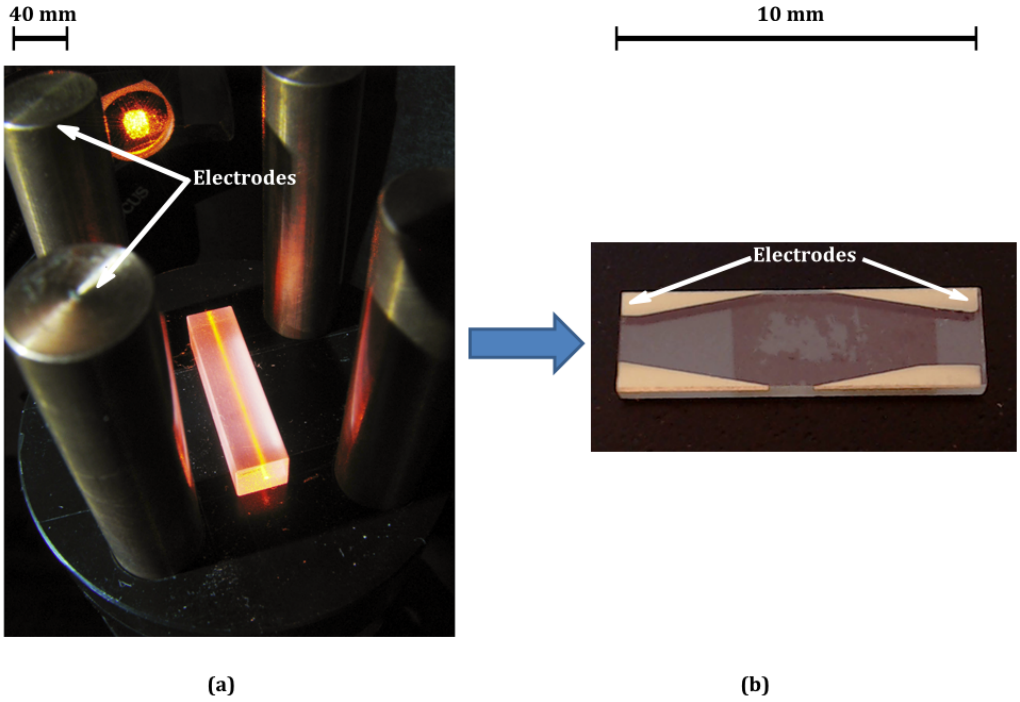

Figure 1.5: Comparison of electrode arrangements for gradient echo memory experiments in (a) Bulk Pr^{3+}:Y_2SiO_5 [1], (b) Thin film of TeO_2 on Pr^{3+}:Y_2SiO_5 substrate.

applications.

1.3 Thesis Outline

Chapter 2 briefly introduces the rare-earth ion doped elements and their optical coherence properties. After which, coherent light-atom interactions are studied using a two-level system interacting with a coherent light field. The Bloch vector and Bloch sphere are then introduced as a tool to further study the interactions between the ions and light fields. Using these tools, two coherent transients that can produce different pulse sequences are described. These techniques form the basis of the quantum memories investigated at the end of the chapter.

To build a complex integrated quantum repeater, it would be ideal to combine active elements such as single photon sources and quantum memories, with passive devices like beam splitters and amplitude modulators, all on the same platform. Chapter 3 presents the proposal of an architecture for an integrated linear optics quantum processing unit, which is the building block for a quantum repeater circuit on chip.

Chapter 4 describes the investigated method for the fabrication of rare-earth ion doped thin films. Thin films with the rare-earth ion doped crystal as the active layer are described and fabricated. As is explained in this Section, the growth of single crystalline rare-earth ion doped thin films, that preserve the bulk qualities, proved to be very challenging.

The main focus of this thesis was to implement integrated quantum information devices with passive waveguides. In this approach, high quality bulk crystals were used as the waveguide substrate and a thin layer of a high refractive index glass was deposited on top of the rare-earth ion doped substrate to form the guiding medium. The optically active ions were then accessed via the evanescent field that extended into the substrate as light in the glass was guided by total internal reflection. The rare-earth ion doped crystal and its properties are discussed and the feasibility of this method to construct thin film waveguides using rare-earth ion doped crystals as the substrate is investigated. This chapter finishes by discussing modeling and depositing electrodes for Stark shift effects on thin films.

Chapter 5 gives a compact introduction to waveguide theory, and then follows on to introduce two methods of coupling to waveguides, namely the prism coupling method and grating coupling.

The experiments performed during this project are introduced in chapter 6. The initial experiments were performed using prism coupling. These experiments showed promising results, showing the coherence properties of the waveguide had not changed much compared to bulk sample experiments. After which, an in-house designed cold finger cryostat, used in the next set of experiments, is briefly introduced. Then the experiments with grating coupling in this cold finger cryostat are described. After this, initial experiments were carried out to determine whether the active ions in the substrate of the proposed waveguides could be electrically controlled by applying a small voltage on the electrodes of the thin film.

In Chapter 7, the prospects of the future direction of the designed waveguide structure are presented. Some of the unresolved issues like the grating efficiencies and electrode deposition are further investigated. Finally, Chapter 8 concludes the thesis with an overall discussion of the results.

Chapter 2

Background Theory

2.1 Introduction

In this chapter, an overview of the spectroscopy of rare-earth ion doped crystal, relevant to producing rare-earth waveguides for quantum information applications, is presented. The key properties of interest are the broadening mechanisms of the optical and hyperfine transitions that can potentially be encountered in a waveguide structure. The techniques used for studying these broadening mechanisms are described. Previous studies of broadening in disordered bulk and waveguide structures are described. At the end of this chapter, a brief summary of quantum memory techniques that can be used for waveguide quantum memory devices is also presented.

2.2 Rare-earth ion doped crystals

The 15 elements starting from lanthanum ($Z = 57$) to lutetium ($Z = 71$) are known as the Lanthanide group or the rare-earth elements. In these elements, 14 electrons are added to the $4f$ electronic orbital, consecutively. The $4f$ electron shell is filled from cerium with 1 electron in this shell to lutetium with a full shell of 14 electrons [31].

The two elements scandium and yttrium are also commonly included in the rare-earth group, due to their trivalent ions having filled electron shells. The rare-earth's oxidation state is usually dominated by the trivalent state. The trivalent structure of rare-earth ions is described by $[Xe]4f^N$, with N increasing from 1 to 14. The interesting optical, magnetic and chemical properties of the rare-earths are due to their unique electronic structure. The spectra and energy levels of rare earth ions in crystals is shown in Figure 2.1.

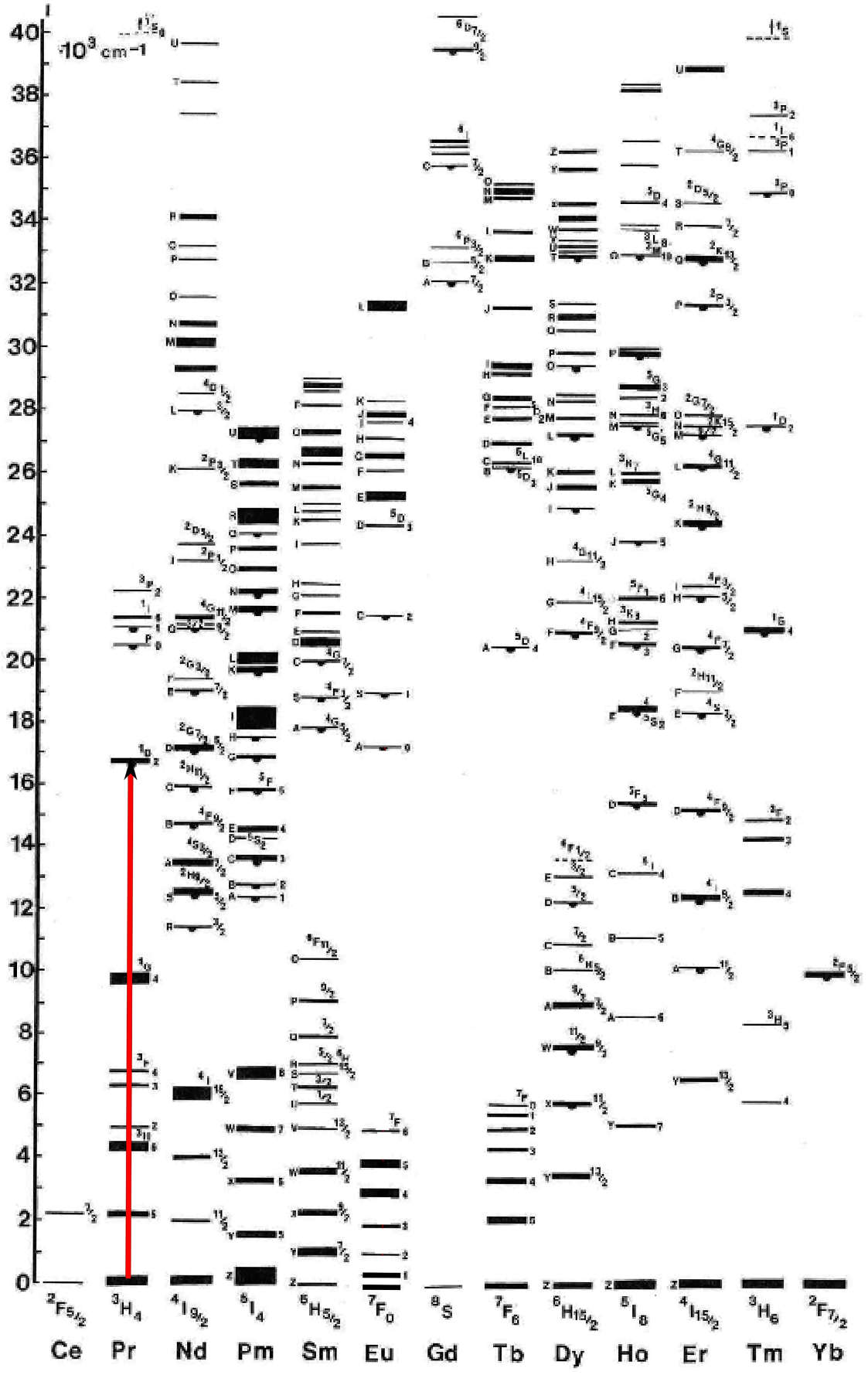

Figure 2.1: Dieke diagram of energy levels of RE^{3+}:$LaCl_3$ [32]. The red arrow indicates the ${}^3H_4 \rightarrow {}^1D_2$ transition of Pr^{3+}, studied in this thesis.

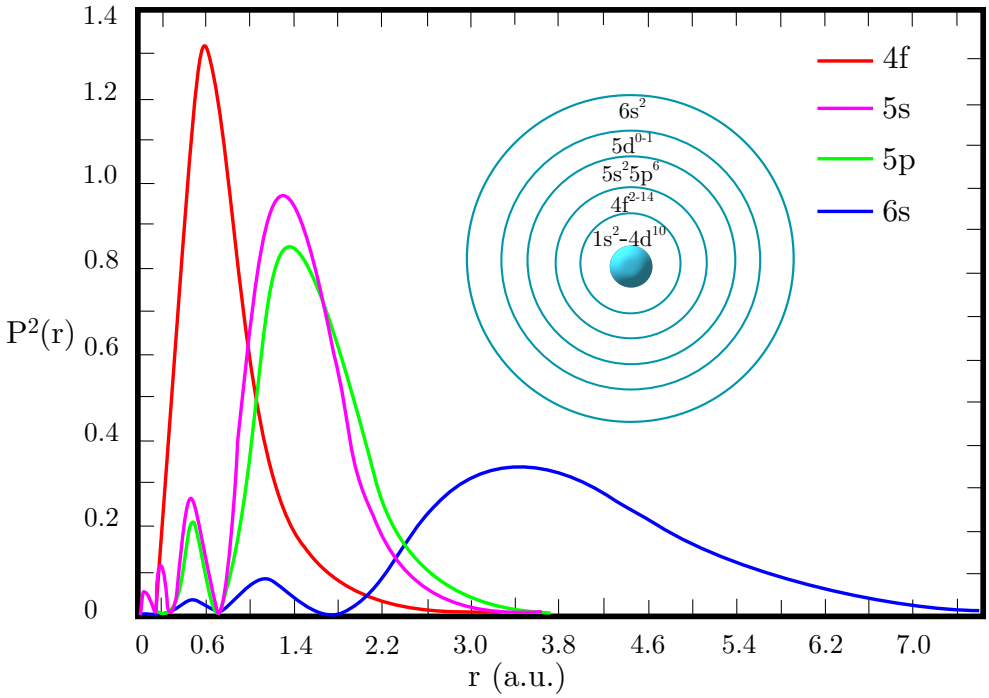

Figure 2.2: Radial probability distribution for the $4f$, $5s$, $5p$ and $6s$ electron subshells of Gd^{+} [33].

The $4f^N \rightarrow 4f^N$ transitions are the transitions that are relevant to this thesis in the rare-earth elements. The unique electronic structure of the rare-earth elements causes them to exhibit interesting optical properties. The approximate radial probability distributions of the electronic orbitals of rare-earth ion structures are shown in Figure 2.2. From Figure 2.2, it can be observed that the electrons in the $4f$ shell, are mostly within the filled $5s$ and $5p$ shells. The outer shells protect the $4fs$ from environmental perturbations, forming a strong Faraday cage around the electrons in the $4f$ shell.

The rare-earth elements can also be divided depending on whether their trivalent ion has an odd (Kramers) or even (non-Kramers) number of electrons. Whether the trivalent ion is a Kramers or not greatly affects the energy structure of the rare-earth.

2.2.1 Intrinsic Hamiltonian

The intrinsic Hamiltonian, as shown in Equation 2.1, consists of energy terms due to the free ion ($\widehat{H}_{\text{f.i.}}$), the crystalline field ($\widehat{H}_{\text{c.f.}}$), the magnetic hyperfine interactions ($\widehat{H}_{\text{m.h.}}$), and the quadrupole interactions ($\widehat{H}_{\text{q.}}$) [34, 35]. These terms have been

extensively discussed in References [34, 35].

$$\widehat{H}_I = \widehat{H}_{\text{f.i.}} + \widehat{H}_{\text{c.f.}} + \widehat{H}_{\text{m.h.}} + \widehat{H}_{\text{q.}} \tag{2.1}$$

When explaining the terms in Equation 2.1 in the following Sections, the focus is on the Pr^{3+} ion in Y_2SiO_5 crystal, which is the crystal used in this thesis. Pr^{3+} ion in Y_2SiO_5 is a non-Kramers ion in a non-axially symmetric site.

2.2.1.1 Free ion Hamiltonian

Because of the strong shielding of the $4f$ electrons, their energy levels are similar to the free ion energy levels, making the crystal field act as a perturbation to the free-ion Hamiltonian.

In the central field approximation, the free-ion Hamiltonian is made up of the Coulomb attraction between the nucleus and the electrons of an electronic system and the Coulomb repulsion of electrons that are close to the nucleus, reducing the attraction of electrons to the nucleus. In this first approximation, the N = 4 energy levels are degenerate.

Beyond this approximation, the other important interaction in the free-ion Hamiltonian is the Coulomb repulsion of electrons not close to the nucleus, lifting the degeneracy in N. Another contributing factor is the spin-orbit interaction that is a function of the position of the electron and the angular momentum of the electron orbit and spin, lifting the degeneracy of the 4f levels. This interaction is caused by the combination of states with different spins (S) and orbital angular momentum (L), while preserving the total angular momentum (J). The spin-orbit interaction results in (2J+1) degenerate multiplets.

2.2.1.2 Crystal field Hamiltonian

The crystal site symmetry lowers the symmetry of the free ion in the solid, partially lifting the LSJ manifolds degeneracy. The crystal field interaction is much less than the spin-orbit interactions, therefore it can be considered as a perturbation on the free-ion Hamiltonian.

For Pr^{3+} ion in Y_2SiO_5, the degeneracy is completely lifted which results in $2J+1$ crystal field levels for each J manifold. In these sites, the angular momentum

(J) is quenched which results in the states having no first order electronic magnetic moment. Hence, non-Kramers ions in low symmetry sites have relatively low sensitivity to magnetic field.

2.2.1.3 Magnetic hyperfine Hamiltonian

The interaction between the electronic and nuclear magnetic moments is described by the magnetic hyperfine Hamiltonian. Due to the quenching of the electronic angular momentum (J) in Pr^{3+} ion in Y_2SiO_5, the magnetic hyperfine interaction vanishes to first order, but it's still present in second order.

Quadrupole Hamiltonian

The true quadrupole interaction is the electric quadrupole coupling at the nucleus caused by the electric field gradient. The charges in the lattice of the crystal, the anti-shielding of the electrons close to the nucleus and the effect of the 4f electrons produces the electric field gradient.

Another contributing factor to the quadrupole Hamiltonian term is a second order magnetic hyperfine interaction coupling neighboring states inside the LSJ manifold. This second order magnetic dipole interaction is called the pseudo-quadrupole. These two terms look similar mathematically and can be treated together as one single quadrupole interaction. In the case of the Pr^{3+} ion in Y_2SiO_5, this Hamiltonian term causes the electronic singlets to split into three doubly degenerate levels.

Zeeman shift

The Zeeman interaction consists of the nuclear Zeeman and the electronic Zeeman terms. For Pr^{3+} ion in Y_2SiO_5, the first order term of the electronic Zeeman term vanishes because the orbital angular momentum (J) is quenched. The second order term of the electronic Zeeman is similar in size to the nuclear Zeeman term and can be combined to form the enhanced nuclear Zeeman term [36].

In the current work, the Zeeman interaction is important in understanding decoherence mechanisms for both the hyperfine and optical transitions.

Rare-earth ion system	Site symmetry	Wavelength (nm)	Linear shift MHz V^{-1} cm
$0.1\%Pr^{3+}:Y_2SiO_5$	C_1	607.77	0.0929
$0.1\%Pr^{3+}:Y_2SiO_5$	C_1	605.81	0.1116
$Eu^{3+}:YAlO_3$	C_s	581.6	0.0335

Table 2.1: Stark coefficients for $0.1\%Pr^{3+}:Y_2SiO_5$ and $Eu^{3+}:YAlO_3$ bulk crystals, obtained using photon echo experiments [4].

2.2.1.4 Stark shift

The optical Stark shift $\delta(f)$, the frequency change of an optical transition in the presence of an external electric field E_0, is given by Equation 2.2 [37]. In this equation, the change in the electric dipole moment between the excited and ground states is given by $\delta\mu$ and α is the electric polarizability of the ion.

$$\delta(f) = -L\delta\mu E_0 - 0.5L^2 E_0 \delta\alpha E_0 \tag{2.2}$$

where L is the local field correction which is usually approximated by the following equation:

$$L = (\epsilon_1 + 2)/3 \tag{2.3}$$

Where ϵ_1 is the low frequency dielectric constant.

For non-centrosymmetric sites a static dipole moment is observed and the linear form typically dominates for moderate fields. In rare-earth systems, for the $4f^N \rightarrow 4f^N$ transitions, the linear Stark shifts are approximately in the range of 0.002 to 0.2 MHz V^{-1} cm. Table 2.1 shows Stark coefficients for $0.1\%Pr^{3+}:Y_2SiO_5$ and $Eu^{3+}:YAlO_3$ bulk crystals, obtained using photon echo experiments [4].

2.3 Broadening mechanisms

The development of many applications of rare-earth doped crystals, like real time high frequency signal processing, storage of information in computers or communications networks [38, 39, 40, 41, 42, 43, 44] or frequency stabilizing lasers for spectroscopy of materials or quantum information applications, require narrow homogeneous broadening and low spectral diffusion. As a result, there has been a significant effort over the last 30 years to understand and control mechanisms caus-

ing broadening on the optical transition.

Mechanisms causing broadening in rare-earth ion doped crystalline structures are typically categorized into three groups based on the time scale of the broadening. Static disorders cause a broadening called "inhomogeneous broadening", which results in a large spread of the ions' center frequencies over the ensemble. "Homogeneous broadening" is due to dynamic coupling to the environment that occurs on a time scale that is short compared to the coherence time (T_2). "Spectral diffusion", is due to dynamic coupling to the environment occurring on a time scale that is long compared to T_2. The mechanisms commonly responsible for these categories of broadening are described in further Sections.

2.3.1 Homogeneous broadening

Broadening mechanisms influencing the homogeneous linewidth include broadening due to the lifetime of the excited ions, magnetic and phonon broadening, broadening due to interaction with Two-Level Systems and other effects due to the crystalline environment. These mechanisms are discussed in further Sections.

The homogeneous broadening consists of two parts as shown in Equation 2.4. The first term in this equation describes the decoherence caused by population decay and the second part demonstrates the influence of pure dephasing mechanisms.

$$\Gamma_h = \frac{1}{\pi T_2} = \frac{1}{2\pi T_1} + \Gamma_\phi \tag{2.4}$$

Lifetime broadening

Lifetime broadening creates a lower limit on the homogeneous linewidth (Γ_h). The relationship between the excited state lifetime (T_1) and the homogeneous broadening is given by Equation 2.5.

$$\Gamma_h \geq \frac{1}{2\pi T_1} \tag{2.5}$$

The homogeneous broadening caused by the spontaneous decay of the optical dipole creates a Lorentzian line shape with a Full-Width at Half-Maximum (FWHM) shown in Equation 2.5 [45].

The decay out of the excited state can be due to radiative and multi-phonon non-radiative processes. For the ${}^3H_4 \rightarrow {}^1D_2$ transition in Pr^3:Y_2SiO_5 the measured

optical lifetime was 164 μs [2], giving a lower limit of about 970.45 Hz for its homogeneous linewidth. For the lowest crystal field level of the $^1D_2$ transition, the lifetime is radiative limited.

Magnetic broadening

Host ions in rare-earth ion doped crystals create magnetic fluctuations due to spin flips with other host ions in the structure. In many rare-earth ion crystalline systems, these fluctuation limit both the optical and hyperfine transition coherence times. Different methods of reducing this broadening effect have been investigated [14, 46, 47, 48, 49, 50, 51, 52, 53, 54, 55, 56, 57]. In bulk crystals, at temperatures below 4 K, the major contributing factor for dephasing the rare-earth ion's optical transitions are generally the fluctuations in the magnetic or electric field.

The magnetic broadening mechanisms are intrinsic to the crystal and are not expected to be significantly affected when moving to waveguides and therefore were not the focus of this thesis.

Phonon broadening

Phonon processes are the dominant homogeneous broadening mechanism at room temperature. In bulk crystals, this temperature dependence scales with T^7, therefore is usually negligible at temperatures of 4 K and below.

When moving towards nano scale materials like nano-crystals or thin films, the temperature dependence of phonon processes changes. For example, in the research performed by Meltzer *et. al* on Eu_2O_3 nano particles, the temperature dependence was found to be scaling with T^3 rather than T^7 [58]. This shows that phonon broadening can be a major contributing factor when moving towards smaller structures.

Two-level system broadening

In samples with poor crystal structure a major contributing mechanism to homogeneous linewidths is the coupling between energy levels of rare-earth ions with Two Level Systems (TLS) in the disordered lattice structure. TLS can be explained as one or many ions which can tunnel between two energy minima that are near each other in configuration space [59]. The effect of TLS is very important in rare-earth

ion irregular crystalline structures, glasses and nano-crystals [58]. An issue for the current work is the possibility that the fabrication of waveguides in the rare-earth ion crystals will create disorder into the crystalline environment, introducing TLS broadening.

Instantaneous spectral diffusion

Instantaneous Spectral Diffusion (ISD) is a mechanism that happens when the optical excitation of a neighboring ion causes magnetic, electric field fluctuations [60] or phonon induced interactions.

For non-Kramers dopant ions in low symmetry crystalline sites, such as Pr^{3+} ions doped in Y_2SiO_5, ISD can be caused by electric dipole-dipole interactions [61].

ISD can also be due to phonon interactions. In Pr^{3+} ions doped in crystalline structures the phonons are a result of excitation of neighboring Pr^{3+} ions from their ground state to a close by Stark level, due to the non-radiative decay of other Pr^{3+} optically excited ions decaying down to the ground state. This mechanism only happens in Pr^{3+} ions, due to their optical ground state being close to the lowest Stark level (1.5 THz).

Instantaneous spectral diffusion is caused by the interaction between neighboring ions. Therefore, most of the time, homogeneous broadening caused by these effects can be reduced by lowering the concentration of the dopant ion in the crystal.

2.3.2 Inhomogeneous broadening

Variations in the crystal lattice and inhomogeneous broadening effects result in the ensemble being broadened by orders of magnitude compared to the homogeneous broadening observed in these structures. On the optical transitions, this broadening mechanism could result in a crystal linewidth on the order of 0.1 GHz to 100 GHz. For example, for the $0.05\%Pr^3{:}Y_2SiO_5$ crystal which was used in this thesis, the inhomogeneous linewidth has been reported to be 10 GHz [1].

The spectrum in Figure 2.3 illustrates an overall and common image of the inhomogeneous line of the rare-earth crystals. Although each ion has a narrow linewidth, the optical transitions of each ion in the crystal happens at a slightly detuned frequency, due to variations in the crystalline structure. This causes the spectrum of the crystal as a whole to look much broader.

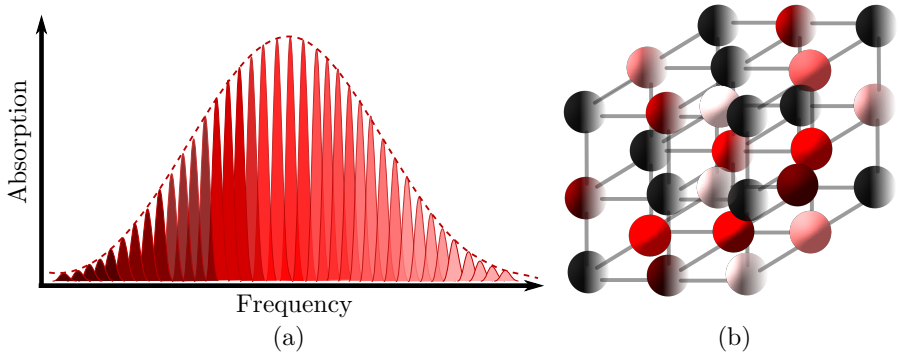

Figure 2.3: Inhomogeneous broadening on an optical transition caused by random defects in the crystal structure, (a) Inhomogeneous spectrum showing packets of homogeneous lines much smaller than the inhomogeneous broadening, (b) Randomly distributed defects in the crystalline structure.

Defects in the crystal lattice such as misplaced or missing ions contribute to this broadening. Ions in highly disordered crystalline structures or amorphous materials such as glass experience quite different local and surrounding environments and this results in highly broadened inhomogeneous linewidths. The broadening of these linewidths can be used to characterize the disorder and amount of defects due to strain and stress in a crystal [59].

Doping the host crystalline structure with the doping ion results in inhomogeneous broadening. This is due to the size mismatch between the host and dopant ions resulting in increased strain in the crystalline lattice. By lowering the doping concentration the inhomogeneous linewidth can be reduced. In ppm (parts per million) doped crystalline structures, an inhomogeneous linewidth of about 10 MHz has been observed in Nd^{3+} ions in $YLiF_4$, isotopically pure in ^7Li [62].

In another study, an optical inhomogeneous linewidth was measured in a stoichiometric $EuCl_3.6H_2O$ crystal. This crystal was isotopically pure in ^{35}Cl. A very narrow optical inhomogeneous linewidth of 25 MHz was reported [25].

2.3.3 Spectral diffusion

Spectral diffusion is caused by dynamic coupling to the environment that happens on a long time scale compared to the coherence time (T_2). As time passes, the frequency shifts of the ions produce small random walks, or "diffusion", in frequency space across the optical spectrum. The importance of the decoherence which results from spectral diffusion has been investigated in the field of optical spectroscopy of solids [63, 64, 65, 66, 67].

Spectral diffusion in a rare-earth crystalline material happens when an interaction causing a big frequency shift and a mechanism which modulates the magnitude of the interaction occurs in the structure. A significant mechanism causing spectral diffusion in rare-earth ion doped crystalline systems is due to the magnetic dipole-dipole interactions of the active ions in the crystal and the electronic nuclear flips of the host material.

2.3.4 Hyperfine broadening

In rare-earth ion doped crystals, the hyperfine transitions can experience much longer lifetimes and coherence times compared to the optical transitions. The very long lifetimes in hyperfine transitions are due to these transitions being less sensitive to the crystal environment compared to optical transitions, and also because at these very low energies, very few phonons can exist [68]. Therefore, to be able to build a practical quantum information device, these states can be used for long-term storage of the quantum information. In a rare-earth ion doped crystal, the inhomogeneous broadening of the hyperfine transition could be on the order of 10 kHz to 100 kHz.

Hyperfine lifetimes are quite strongly dependent on temperature, magnetic field and dopant concentration. In Pr^{3+}:Y_2SiO_5, the hyperfine lifetime was reported to be about 200 s at 1.6 K [69]. The coherence time in zero magnetic field was reported to be about 0.5 ms [70]. In these crystals, the main decoherence is caused by the magnetic interaction between the host (Y) spins and the Pr^{3+} dopant ion, hence by applying a magnetic field the coherence time can be considerably increased.

The magnetic moment of the dopant ion of Pr^{3+} is larger than the host Y magnetic moment [35, 71]. The presence of the dopant ion detunes the neighboring ions in the crystalline structure, which can decouple these ions from the rest of the crystalline environment. Hence, the neighboring Y ions no longer exchange spins with each other, which is referred to as a "frozen core". By applying a magnetic field to the crystal, a larger magnetic dipole moment is produced, which is used to increase the frozen core effect and reduce the spin-flips in the crystal further.

Furthermore, the transition frequency sensitivity can be adjusted to magnetic fluctuations by applying an external magnetic field. A magnetic field can split the doubly degenerate hyperfine states. At a particular magnetic field, the transition frequency goes through a critical point, at which point the transition is not sensitive to magnetic field perturbations in any direction. This method is the zero first-order

Zeeman (ZEFOZ) technique, which has been used to extend coherence times in Pr^{3+}:Y_2SiO_5 to 1.4 s in a particular critical point [49].

2.4 Spectroscopic techniques for studying broadening

2.4.1 Spectral holeburning

Spectral holeburning is used to observe the spectroscopic properties of rare-earth ion doped crystals. It is also used to tailor the absorption line and prepare groups of ions perform certain operations.

To optically select one pack of ions with a certain frequency, a laser beam tuned to that particular frequency is applied to the crystal. The laser excites the ions, therefore pumping them from their ground state to the excited state. After which, the excited ions spontaneously emit a photon and fall back down to any ground state, depending on the oscillator strength of that transition. If the laser is left on for long enough, all the ions are pumped out of that particular ground state, and hence a " hole " is created. A simple spectral holeburning scheme is illustrated in Figure 2.4.

During the spectral holeburning process, some hyperfine levels which have been used to pump the ions out of another level will end up with an increased population of ions. This creates an increase in the absorption profile called an anti-hole. Therefore, the real structure of an absorption profile during spectral holeburning, is much more complex than what is shown in Figure 2.4, with holes and anti-holes, which are present around the created hole.

Spectral holeburning can be used to study the Stark field interactions with the ions in a rare-earth ion doped crystal. If an electric field is applied to a hole, due to the stark shift effect explained in Section 2.2.1.4, the hole can move in frequency space.

Spectral holeburning can also be used to tailor the inhomogeneous linewidth which is the basis for the Atomic Frequency Comb and the Gradient Echo memory schemes [72]. In this process, a wide hole called a "trench", that is much wider than the homogeneous linewidth, is created in the absorption line by scanning the laser. Then, a narrow hole is burnt back at a different frequency from the center of the

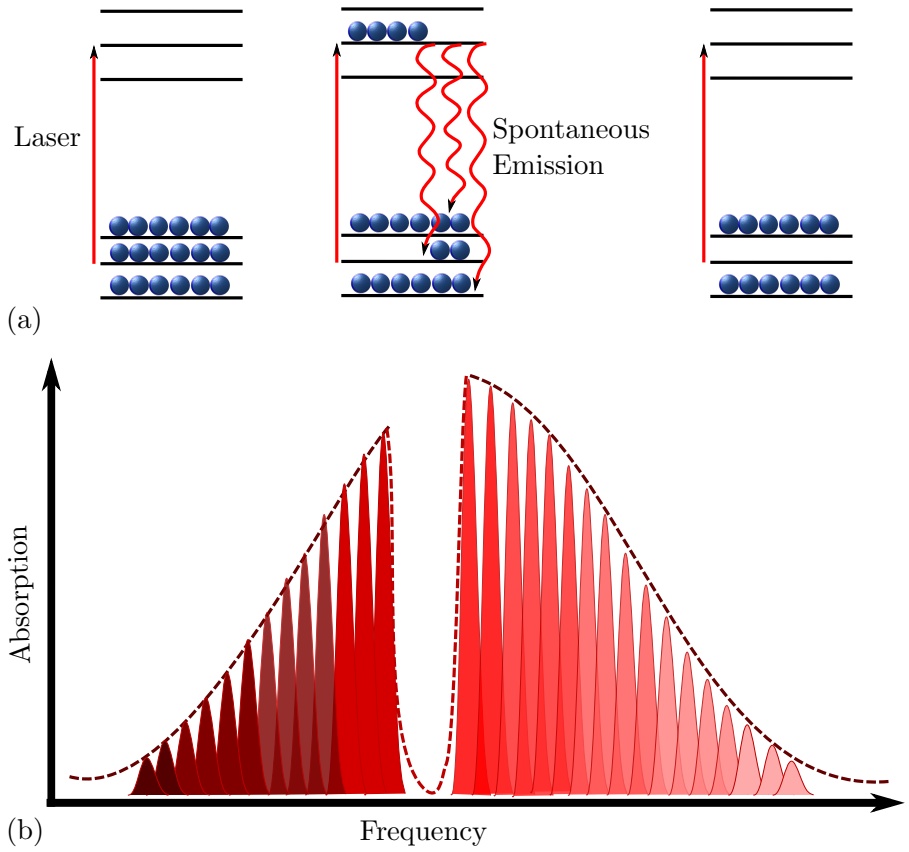

Figure 2.4: Spectral holeburning, (a) Energy level diagram of spectral holeburning, (b) Inhomogeneous line spectrum with burnt hole.

trench. Some of the absorption from the created hole will create an anti-hole in the center of the trench. The resultant absorption line with the burnt trench and the created narrow line is shown in Figure 2.5. By applying an electric field to the crystal, causing a Stark shift, the trench and the created antihole can be moved to different frequencies.

2.4.2 Coherent light-atom interactions

An ensemble of atoms interacts with any externally applied electromagnetic field, resulting in a coherent emission of light from these atoms. Two phenomena that can be described by this interaction are photon echoes [73] and free induction decay [74]. Photon echoes are the basis for many coherent transient experiments, and are discussed in this thesis.

Rare-earth ion doped materials provide a good system for photon echo techniques. Atoms have a large number of eigenstates, but for the purpose of explaining photon echoes in a rare-earth ion doped material, it is sufficient to consider a two-

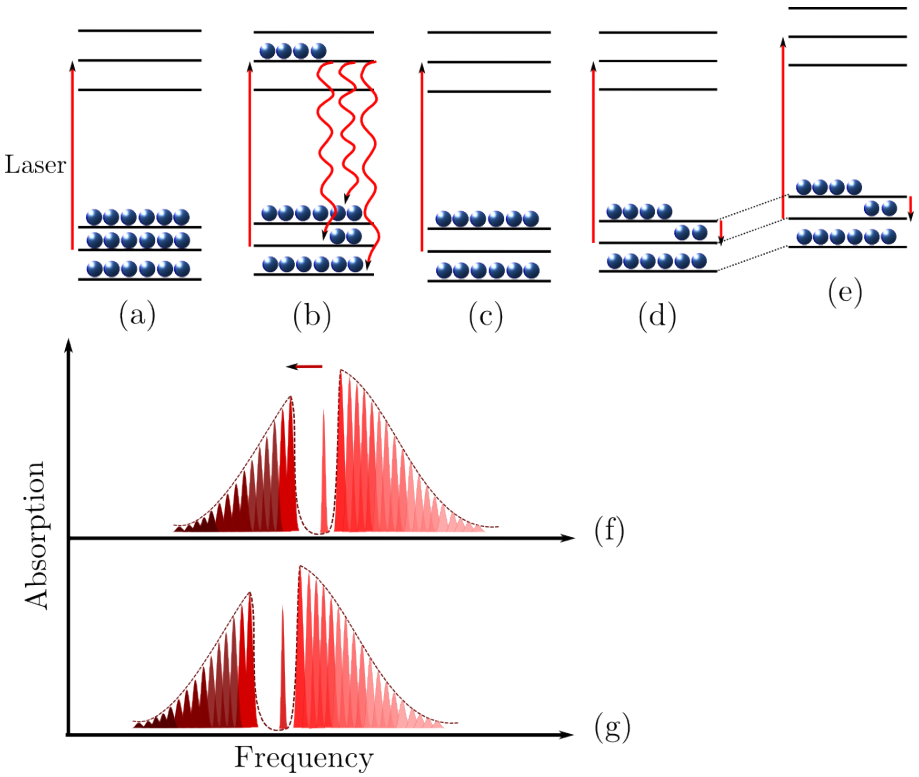

Figure 2.5: Tailoring the inhomogeneous absorption profile, (a) Laser resonant with specific transition, (b) Spontaneous emission down to all ground states, (c) Selected transition emptied, hole burnt, (d) Specific amount of ions placed in empty state using another laser source, narrow linewidth created, (e) Electric field turned on, narrow linewidth of ions moved in frequency space. (f) Inhomogeneous linewidth spectrum, with burnt hole and narrow linewidth of ions created in hole, (g) Packet of selected ions moved using electric field.

level system, i.e. one optical ground and one optical excited state [75, 76, 77]. In this case, the external electromagnetic field is chosen such that it has an energy close to the difference between these two states.

2.4.2.1 Bloch vector description

The Bloch vector and equations are used to explain the state of a two-level atom and its interactions and evolutions. The Bloch vectors are introduced in a new coordinate system, with the the coordinates u, v and w.

The Bloch equation can be generally utilized to explain any two-level energy system. This new system can be expressed in terms of the probability amplitudes $C_g(t)$ and $C_e(t)$ as in Equation 2.6. In Equation 2.6 $\boldsymbol{C_g(t)}$ and $\boldsymbol{C_e(t)}$ are the

probability vectors.

$$\begin{cases} u(t) - iv(t) = 2\boldsymbol{C_g(t).C_e^*(t)} \\ w(t) = |C_e(t)|^2 - |C_g(t)|^2 \end{cases} \quad (2.6)$$

The Bloch vector is a vector from the origin (0,0,0) to the point (u, v, w). This vector can be used to characterize the atomic state. If the atom is in a pure quantum state, the vector will be normalized as described by Equation 2.7.

$$u^2 + v^2 + w^2 = 1 \quad (2.7)$$

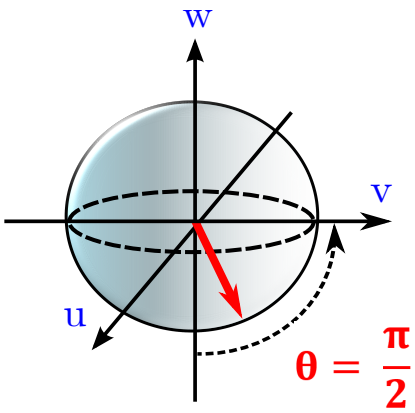

Figure 2.6: Bloch sphere used to visualize the atomic state

A unit sphere called the Bloch sphere can be used to visualize the atomic state as shown in Figure 2.6. The relaxation and dephasing of an ensemble average of atoms can be displayed with a Bloch vector pointing at different positions inside the sphere. For example, an excited state of an atom can be represented by $w = 1$ and $u = v = 0$. This is due to the fact that there is no coherent superposition (u, v) between the excited and ground states.

Also, a vector with $u = 1$, $v = w = 0$ demonstrates a 50/50 superposition state and the atoms would be at the equator of the sphere. These atoms oscillate in phase $(u = 1)$ with the applied electric field. Furthermore, a vector with $u = v = w = 0$ displays a completely mixed state and the probability of finding atoms in any state is equal.

By applying pulses of light to the Bloch vector, it can be rotated in the Bloch sphere. The phase of the applied pulse gives the axis of rotation in the uv plane of the sphere. The angle by which the rotation occurs is given by the area of the pulse given by Ωt. The angular Rabi frequency Ω, measures the strength of the

interaction between a laser field, resonant with the atomic transition, and the atoms shown in Equation 2.8.

$$\Omega = \frac{\boldsymbol{E}.\boldsymbol{\mu_{ge}}}{\hbar} \tag{2.8}$$

In the equation given above, the strength of the transition is given by μ_{ge}, which is the transition dipole moment. $\boldsymbol{E}$ is the applied field.

The transition strength can be measured by calculating the optimum length of a pulse that rotates the Bloch vector by 180^o. This pulse is called a π pulse. The transition strength is usually given by a term called the oscillator strength, which is the strength of the transition compared to an electron that is oscillating and is given by Equation 2.9.

$$f = \frac{8\pi^2 m_e c}{3e^2 h\lambda}|\omega_{ge}|^2 \tag{2.9}$$

Where e and m_e are the charge and mass of the electron, respectively.

The difference between the resonance frequency of the atomic transition (ω_{ge}) and the laser frequency (ω_L) is characterized by the detuning (Δ) in the system shown in Equation 2.10. Hence, the generalized Rabi frequency, the rate that the phase of the atomic state changes relative to the phase of the laser field, can be calculated using Equation 2.11.

$$\Delta = \omega_{ge} - \omega_L \tag{2.10}$$

$$\Omega_G = \sqrt{\Omega^2 + \Delta^2} \tag{2.11}$$

The optical Bloch equations which describe the dynamics of the atomic state in a rotating reference coordinate system are expressed as Equation 2.12.

$$\begin{cases} \frac{\partial u}{\partial t} = -\Delta v - \frac{u}{T_2} \\ \frac{\partial v}{\partial t} = \Delta u + \Omega w - \frac{v}{T_2} \\ \frac{\partial w}{\partial t} = -\Omega v - \frac{w - w_{eq}}{T_1} \end{cases} \tag{2.12}$$

$\frac{1}{T_1}$ is the rate that the atoms relax towards equilibrium. $\frac{1}{T_2}$ is the rate at which

decoherence or random dephasing of the interactions occur.

The finite amount of decoherence (T_2) causes the Bloch vector to decrease in amplitude towards the w axis. The relaxation lifetime (T_1) causes the Bloch vector to descend towards the equilibrium state of $w_{eq} = -1$. If the coherence of the atomic state is only limited by the natural lifetime decay, an upper limit can be applied to the coherence time (T_2). This would result in the inequality $\mathrm{T}_2 \leq 2T_1$.

2.4.2.2 Coherent transients

Two coherent transients, the free induction decay and photon echo effects, will be explained in this Section. The Bloch formalism can be used to describe these two effects. These two phenomena are useful tools in the field of spectroscopy [77, 78].

Free induction decay

An inhomogeneously broadened ensemble of atoms can be excited from their ground state by applying a short strong pulse of light. Atoms with a certain frequency interval Δf are excited, which can be approximated by inversing the duration of the applied pulse of light as given by Equation 2.13.

$$\Delta f \propto \frac{1}{\tau_p} \tag{2.13}$$

Where τ_p is the duration of the applied pulse of light. In this case, it is assumed that the duration of the pulse is shorter than the coherence time T_2 and the pulse is monochromatic.

If the pulse area θ is not an even multiple of π, the Bloch vectors of the atoms will have a component in the $u - v$ plane. This can be pictured as an oscillating dipole moment and the atoms will radiate. Atoms that are excited with a pulse area of $\frac{\pi}{2}$ experience maximum dipole emission and end up on the equator of the Bloch sphere ($u - v$ plane). Right after the excitation pulse is applied, a strong coherent emission in the direction of the input pulse occurs, which is due to the atoms oscillating with the same phase. Groups of atoms have different frequencies, hence they start to dephase. This dephasing decreases the emission rate of the atoms, this phenomenon is called the free induction decay (FID) [74] and is depicted in Figure 2.7. In ensembles where atoms have a large frequency difference, this

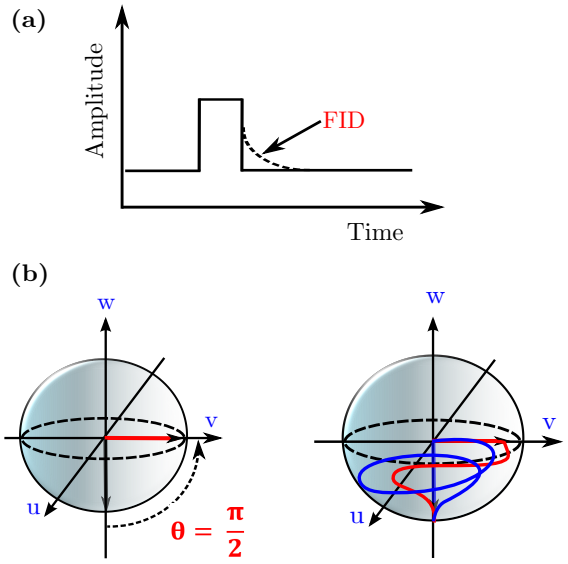

Figure 2.7: Free induction decay after a $\frac{\pi}{2}$ pulse is applied.

reduction in the emission happens faster. Hence, the duration and shape of the FID can give information about the shape and linewidth of the excited atoms in the ensemble [74, 79].

The decay time of the FID can be approximated by Equation 2.14. In this equation Δf is the spectral width of the emitting atoms in the ensemble. If the Fourier width of the excited pulse is much narrower than the inhomogeneous linewidth absorption of the atoms, the duration of the FID is similar to the length of the input pulse of light.

$$\tau_{FID} \propto \frac{1}{\Delta f} \tag{2.14}$$

The two-pulse photon echo

In an ensemble with radiating atoms, a coherent emission of light is produced when quantum oscillations are rephased in the time domain. This phenomena was first used, in bulk NMR, in the form of spin echoes [80]. An optical analogue of the bulk NMR spin echo, the photon echo, was first demonstrated in ruby crystals [73]. If an inhomogeneously broadened ensemble of atoms is excited by a coherent laser with a fixed frequency, the Bloch sphere and the Bloch formulas can be used to describe the photon echo process. Other descriptions of the photon echo process can be found in [81, 82, 83, 84].

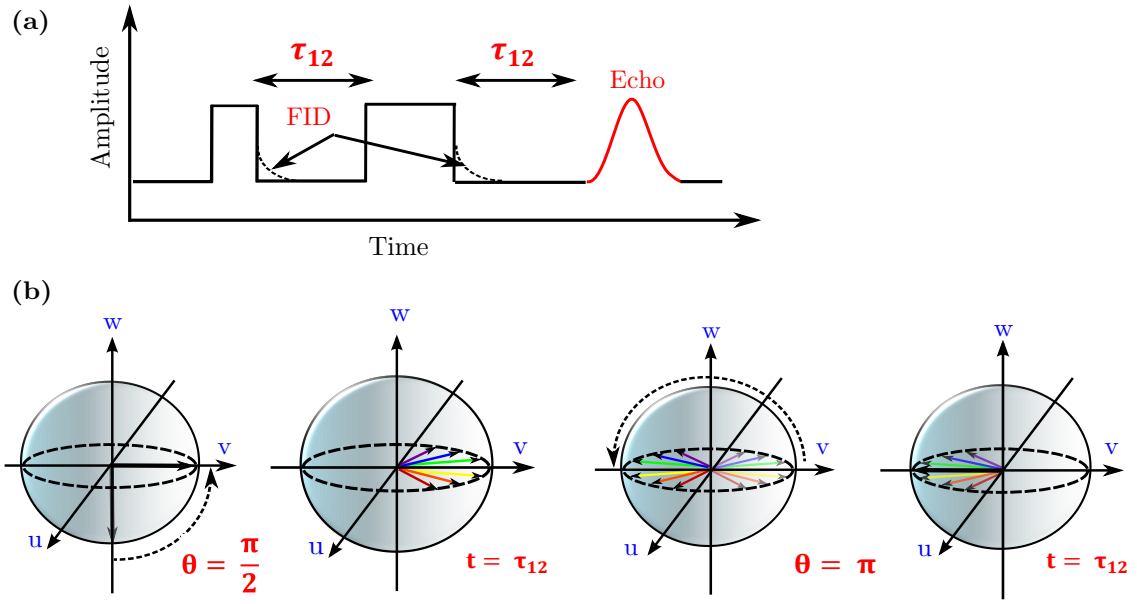

Figure 2.8: Two-pulse photon echo, (a) Two-pulse photon echo sequence, (b) Bloch vector demonstration of two-pulse photon echo.

A typical two-pulse photon echo sequence is shown in Figure 2.8. The photon echo technique is a method to obtain the coherence time, which is then used to calculate the homogeneous linewidth. In this method, two co-linear laser pulses, which are in resonance with the optical transition frequency of the rare earth ion, are applied to the crystal. The echo sequence consists of a $\pi/2$ pulse, which takes the ions into a superposition state on the equator of the Bloch sphere. After which, the system is allowed to evolve freely for time τ. Since each ion has a slightly different resonant optical transition frequency, after the first pulse is applied, the ions start to evolve with different frequencies. Then, a π pulse is applied to the system, to effectively reverse the Bloch vector components' phase evolution. After a further time τ, an echo of the original signal is emitted.

The homogenous linewidth is calculated by measuring the echo intensity as a function of the pulse delay τ. Equation 2.15 usually describe this relationship.

$$\begin{cases} I_{echo} = exp(-4\tau/T_2) \\ \\ Amp_{echo} = exp(-2\tau/T_2) \end{cases} \tag{2.15}$$

As stated before, atoms in an ensemble emit photon echoes coherently, therefore this emission depends on the coherence time (T_2) of the atoms. Hence, for a two-pulse photon echo to be emitted by the ensemble, the atomic coherence must last until the emission of the echo.

The three-pulse photon echo

A three-pulse photon echo is similar to a two-pulse photon echo, where the second pulse is split into two halves. Figure 2.9 shows the three-pulse photon echo sequence. Similar to a two-pulse photon echo, the first pulse creates a coherence between the ground and excited states. This rotates the Bloch vectors from the ground state up to the equator, $u-v$ plane. The second pulse is a $\pi/2$ pulse which rotates the Bloch vectors around the u axis by 90°. This pulse moves atoms with a positive v component to the ground state and atoms with a negative v component will move towards the excited state. The phase of the atoms depends on their relative frequencies with respect to the laser frequency ($\Delta = (\omega_{ge} - \omega_L)$). During the delay time between the first and second pulse, τ_{12}, the phase of the atoms is accumulated. Therefore, the atoms moved towards the excited state satisfy the condition in Equation 2.16.

$$\frac{-\pi}{2} < \Delta.\tau_{12} + 2\pi n < \frac{\pi}{2} \tag{2.16}$$

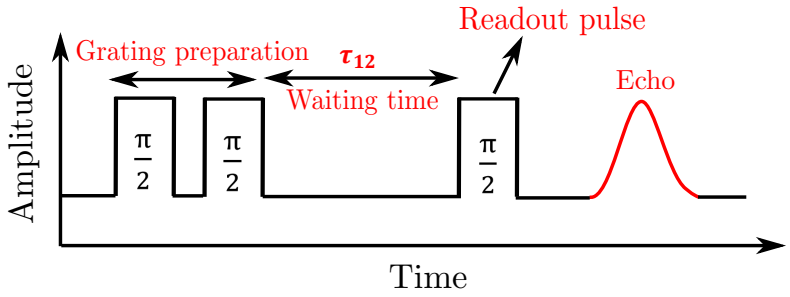

Figure 2.9: Three-pulse photon echo sequence.

The two $\pi/2$ pulses effectively create a frequency- dependent periodic phase modulation on the atoms in the ground and excited states. This sequence creates a population grating in the ensemble and the relative phase information is maintained. After the population grating is created, a third pulse is applied to stimulate the atoms to emit a photon, the echo pulse.

In an ensemble, it is assumed that all the atoms contribute towards emitting the echo pulse. The intensity of the three-pulse photon echo can be calculated as Equation 2.17, assuming all the atoms encounter the same pulse area.

$$I_e \propto sin^2\theta_1.sin^2\theta_2.sin^2\theta_3 \tag{2.17}$$

Where θ_1, θ_2 and θ_3 are the pulse areas of the first, second and third pulses,

respectively. If the pulse areas are small, it can be concluded that the echo intensity is proportional to the product of the three pulse intensities ($sin\theta \approx \theta \propto E \propto \sqrt{I}$). The echo amplitude can be calculated from Equation 2.18 in the time domain, and from Equation 2.19 in the frequency domain [85, 86].

$$E_{echo}(t) \propto E_1(t) \otimes (E_2(t) * E_3(t)) \tag{2.18}$$

$$E_{echo}(t) \propto \int_{\infty}^{\infty} E_1(\omega)^* E_2(\omega) E_3(\omega) e^{-i\omega t}\, \mathrm{d}\omega \tag{2.19}$$

Where $\otimes$ symbolizes a correlation and the $*$ denotes a convolution operator. Equation 2.19 is basically a Fourier transform.

The excited state lifetime (T_1) is the limit for maintaining the population difference between the ground and excited states. If the excited atoms have the opportunity to be transferred down to a metastable state, the population difference can be maintained for a longer time than the T_1 of the excited state. Therefore, the frequency-dependent modulation of the population can be preserved for longer times. In this configuration, the first two pulses can be thought of as *write pulses* and the third pulse can be a *read out pulse*. In a rare-earth crystal for example, the first two pulses would be used to modulate the inhomogeneous absorption profile in the frequency domain. The third pulse can then be used to stimulate the atoms and produce an emitted echo signal, carrying the spectrally programmed information.

The Three-pulse photon echo was the basis for classical optical data storage [85, 87]. The first two pulses are not typically strong enough to produce a population grating that can be maintained for long. Therefore, they are often repeated many times in order to produce a coherent accumulation of the population grating. This sequence is used in an atomic frequency comb (AFC) memory, which will be introduced in Section 2.7.1.1. If N preparation pulse pairs are directed at the sample, the echo signal intensity can be calculated from Equation 2.20. Figure 2.10 shows a typical sequence of the accumulated photon echo.

$$I_e \propto N^2 \tag{2.20}$$

According to the theory presented in previous Sections, it can be concluded that by applying suitable laser pulses to an ensemble, any desired rotation on the Bloch sphere can be obtained. These light pulses can be single pulses or a sequence

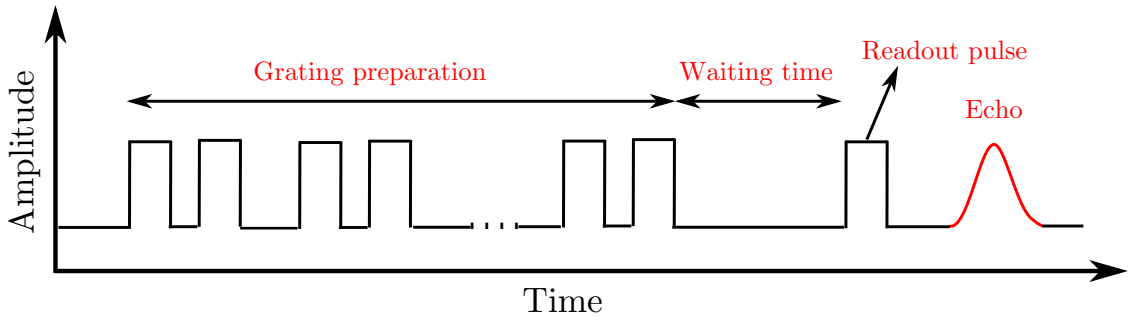

Figure 2.10: Accumulated photon echo sequence.

of pulses, with any duration, phase or frequency. In the quantum information science field using an ensemble of identical ions, a two-level system can be used as one bit of quantum information. In this system, the rotation of the Bloch vector resembles quantum logic operations. Therefore theoretically, by applying different pulse sequences, different logic operations can be obtained in a two-level system. For example, in a rare-earth ion doped crystal, the atoms can be transferred between the different hyperfine levels efficiently through the excited state. Producing coherence between two hyperfine ground states can increase the quantum memory storage time.

2.5 Observation of broadening associated with disorder in bulk samples

In this Section broadening mechanisms that can be significant to waveguide fabrication processes are discussed. Fabrication of waveguides has the potential to introduce disorder into the crystal, and introduce excess broadening onto optical and hyperfine transitions. In this Section, I review linewidth broadenings in bulk as a background to broadening in waveguides.

2.5.1 TLS effect on disordered rare-earth crystals

Fiber samples of Eu^{3+}:Y_2O_3 grown by laser-heated pedestal growth and flame fusion were studied using the optical hole burning technique [88]. This study is the most relevant study of TLS for the current work. The optical dephasing of the $^7F_0 \rightarrow {}^5D_0$ transition was analyzed and compared to previous optical photon echo results. Hole burning experiments at low temperature with these samples demonstrated a

diverse range of results that agreed quite well with coherence times observed with the two-pulse photon echo experiments. 10 s after burning a hole, slow and continuous broadening of the spectral hole from 130 kHz to 900 kHz was observed, in which the additional broadening could have been related to disorder modes in the crystalline structure.

The echo decays for Eu^{3+}:Y_2O_3 were not exponential showing that the linewidth increased in the measured μs time domain, which was the photon echo time domain [88]. In the hole burning experiments , the time domain of the experiments were on the scale of 10 ms, and the results were compared with photon echo results. An ultra narrow optical hole with a linewidth of 3.5 kHz was reported in the flame-fusion sample [88].

The hole burning linewidth results in these fiber samples were found to be larger than those obtained from the photon echo experiments. This increase in the linewidth could indicate spectral diffusion, due to the longer time scale of the hole burning experiments. From hole burning experiments performed on one of the fiber samples, a continuous and monotonic increase in the linewidth was observed with increasing the delay between the burn and read pulses. The frequency scale of the spectral diffusion was 2 orders of magnitude higher than what would have been possible if the magnetic interactions with the ^{89}Y nuclear moments were taken into account. The obtained results from these experiments indicated the presence of an additional dynamic process in the fiber samples, which was related to some form of low energy excitation occurring over a long time scale. Comparing the narrow homogeneous linewidths in the fiber samples with glass, could be an indication that the density of two-level systems (TLS) was much less in these crystalline materials or that the average Eu^{3+} ion was a long way away from any localized dynamic center.

When one moves away from bulk crystal structures to two dimensional systems like nano-crystals or thin films, the properties of the rare-earth may change. One path that was taken in this thesis was to try to grow rare-earth ion single crystalline thin films [23]. The resultant thin films were polycrystalline thin films, and so they may be comparable to nano-crystalline structures.

A study of electron and phonon interaction was carried out by Meltzer *et. al*, which resulted in the conclusion that the situation changes in nano-crystals where the size of the crystal is extremely small [89]. The particle size and temperature dependency of spectral hole linewidths were examined. The experiments were performed on the $^7F_0 \rightarrow {}^5D_0$ transition of Eu^{3+} in Eu_2O_3. It was observed that for

nano-particles, the well known T^7 low temperature dependency of the homogeneous linewidth was reduced to T^3. The experimental results showed that the phonon modes broaden with respect to frequency as ω^2. Assuming the nano-particles were spherical, and with $\omega = 25$ cm^{-1}, coherence times of $T_2 = 40$ ns were obtained. The linewidth of the phonon interactions in these nano-particles were determined by comparing the results obtained from experiments and theory calculations. It was predicted, and later shown by experiments, that the hole linewidth is dependent on the size by $\approx D^{-2.5}$.

2.5.2 Intrinsic disorder of $LiNbO_3$

When doping rare-earth ions into $LiNbO_3$, additional defects are introduced in the lattice that can cause additional strain, change the symmetry of the lattice and alter the coherence properties of the doped rare-earth ion. Furthermore, additional intrinsic disorder arises from the growth process of bulk $LiNbO_3$ single crystals [90, 91]. These intrinsic defects and disorder of the $LiNbO_3$ crystal lattice lead to a large inhomogeneous broadening of the optical and hyperfine transitions. For example in a Tm^{3+}:$LiNbO_3$ crystal, the inhomogeneous broadening was reported to be 300 GHz [92, 93]. And for a Pr^{3+}:$LiNbO_3$ bulk crystal, the combined inhomogeneous linewidth of the two sites of Pr^{3+} was reported to be about 1500 GHz, which is 1000 times larger than the observed linewidth of Pr^{3+}:Y_2SiO_5 [94].

Furthermore, the lattice disorder and strain in rare-earth ion doped $LiNbO_3$, can result in glass like behavior causing a dynamic disorder in these crystals [95, 96, 97]. Also, the nuclear spins in the $LiNbO_3$ crystal lattice results in dynamic magnetic disorder causing additional decoherence in the lattice [65, 98, 99]. It was approximated that the magnetic fluctuations caused by the host ion spins in the crystalline lattice was 30 times higher than Y_2SiO_5 [94]. This magnetic disorder, can lead to additional spectral diffusion and cause large homogeneous linewidths. For example, the observed homogeneous linewidth in Tm^{3+}:$LiNbO_3$ was increased from 28 KHz to about 50 KHz [94]. Also, the homogeneous linewidth reported in a Pr^{3+}:$LiNbO_3$ bulk crystal, was observed to be about 80 kHz, which is about 10 times larger than in Pr^{3+}:Y_2SiO_5 [94].

From the large inhomogeneous and homogeneous linewidth reported in rare-earth ions of Tm^{3+} and Pr^{3+} doped in $LiNbO_3$ crystals, it can be observed that although high quality waveguides can be fabricated using $LiNbO_3$, it may not be the best host crystal for quantum information devices. The large inhomogeneous linewidths observed in these crystals results in low optical depths compared to rare-

earth ions doped in Y_2SiO_5, which results in lower absorption. The high optical depths and high absorption obtained in rare-earths doped in Y_2SiO_5 host crystals means that the fabricated waveguide devices can be shorter in length, which is important when moving towards integration of a lot of different devices onto a single platform. Furthermore, Tm^{3+} has a nuclear spin of $\frac{1}{2}$ compared to Pr^{3+} with a nuclear spin of $\frac{5}{2}$, which means that the long coherence times of the hyperfine structure of Pr^{3+} can be used to stored quantum information. Hence, waveguides using Tm^{3+}:$LiNbO_3$ experience some intrinsic host crystal difficulties that are not present in Pr^{3+}:Y_2SiO_5.

2.6 Broadening mechanisms in waveguides

Ions near the surface in waveguide interfaces may introduce new broadening mechanisms not present in the bulk. The size of waveguide devices are usually on the order of a few wavelengths. Therefore, the perturbed ions in a rare-earth ion waveguide structure are in close proximity to the surface, or at least an interface, of the sample. The first step to ensure miniaturization can be achieved using rare-earth crystals is to determine whether these near surface ions behave the same as bulk crystals.

In 2007 Bartholomew [100] investigated the dynamic disorder in near surface ions of rare-earth ion crystals, using evanescent field hole-burning experiments conducted on 0.5% Eu^{3+}:Y_2SiO_5. The results showed that ions within 200 nm from the surface had similar properties to bulk samples. Good agreement was observed from hole-burning experiments at both the surface and in the bulk samples. However, in these experiments at zero magnetic field, the zero-power linewidth of the spectral holes for the surface and bulk ions was approximately 70 kHz in contrast to the 250 Hz observed in the same material [68], using photon echoes. This indicated that the experiments didn't have enough resolution to decisively conclude that the near surface ions behaved the same as bulk sample ions.

In 2011, photon echo experiments in a Pr^{3+}:Y_2SiO_5 whispering gallery mode resonator were performed by McAuslan *et al.* [101]. The fundamental mode of the resonator was excited which meant that the ions about 5 μm from the surface had been probed. The coherence times in the resonator were similar to the bulk of the resonator and the longest reported coherence time in this crystal [2].

The before mentioned experiments are a strong indication that the properties of the near surface ions are similar to the bulk sample measurements and therefore the coherence properties of these crystals are preserved at the surface. By

2011 these promising results seemed to indicate that rare-earth ion waveguides seem feasible.

However, for coherent applications, other than the behavior of near surface ions, the properties of highly stressed regions due to the waveguide fabrication method could also limit the prospect of building rare-earth ion waveguide quantum hardware. To determine how these factors can affect the rare-earth ion waveguide properties, a number of groups have investigated the coherence of rare-earth ions in a range of waveguide structures.

Flinn *et al.* [21] studied the effect of crystal growing techniques in the year 1994. A planar waveguide was constructed by depositing a thin film of $2\%Eu^{3+}:Y_2O_3$, with a thickness of 3 μm, on a sapphire substrate using the MOCVD(Metal-Organic Chemical Vapor Deposition) technique [102]. The homogeneous linewidth of the thin film was 12.1 MHz, which is four orders of magnitude larger than the bulk sample measurement [22]. The developed thin film had a polycrystalline structure which caused substantial excess broadening, and performed similar to a Eu doped glass structure [103]. Although many groups have been trying to grow single crystalline thin films with good coherence properties, the demonstration of acceptable film quality has not been reported to date.

Sinclair *et al.* [16, 20] demonstrated a $Ti:Tm^{3+}:LiNbO_3$ waveguide in 2010. This waveguide is one of the most studied rare-earth ion quantum devices. Ti^{4+} ions were diffused into the $Tm^{3+}:LiNbO_3$ crystal creating the guiding region of the waveguide [20]. The resulting inhomogeneous linewidth of $Tm^{3+}:LiNbO_3$ was about 300 GHz, similar to the bulk $Tm^{3+}:LiNbO_3$ [92]. Although the diffusion of a high concentration of Ti^{4+} into the crystal lattice induces an even larger stress field in the lattice causing more distortion in the structure, the inhomogeneous linewidth in the waveguide structure was still similar to the bulk $Tm^{3+}:LiNbO_3$. This indicated that the diffusion of Ti^{4+} into the lattice didn't cause a significant excess distortion. The zero magnetic field coherence time in the fundamental mode of the $Ti^{4+}:Tm^{3+}:LiNbO_3$ waveguide at 3 K was 1.6 μs [20]. The coherence time didn't show a substantial increase with an applied magnetic field of 250 G. The coherence times of these waveguides were much lower than bulk sample measurements of about 63 μs (50 kHz) that were observed at similar temperatures of about 1.6 K.

In 2016, Sinclair *et al.* demonstrated that by lowering the temperature to 800 mK, the optical coherence time and hyperfine lifetime can be increased to 117 μs and 2.5 hours, respectively [104]. These results match those of bulk $Tm^{3+}:LiNbO_3$, under the same conditions. The results of this experiment shows the potential of

rare-earth ion doped waveguides designed with industry standard Ti in-diffusion in $LiNbO_3$ for on-chip quantum hardware applications. The coherence properties of these waveguides seem to be temperature dependent, meaning that at higher temperatures the observed coherence times are much lower compared to bulk measurements, but at lower temperatures of about 800 mK they seem to be comparable.

In 2014, we reported the measurement of the inhomogeneous linewidth, homogeneous linewidth and spin state lifetime of Pr^{3+} ions in a novel waveguide architecture [105]. Before this publication, there had not been a successful demonstration of a rare-earth ion waveguide which preserved the unique optical coherence properties of the rare-earth ion. The TeO_2 slab waveguide deposited on a bulk Pr^{3+}:Y_2SiO_5 crystal allowed the $^3H_4 \leftrightarrow {}^1D_2$ transition of Pr^{3+} ions to be probed by the optical evanescent field that extended into the substrate. The 2 GHz inhomogeneous linewidth, the optical coherence time of 70 ± 5 μs, and the spin state lifetime of 9.8 ± 0.3 s indicated that the properties of the near surface ions interacting with the waveguide mode were consistent with those of bulk ions. Also, the fabrication of the waveguide had not caused additional broadening.

After the publication of the observation of photon echoes from evanescently coupled rare-earth ions in a planar waveguide [105], coupling of an ensemble of the rare-earth ion Nd to photonic nano-cavities that were fabricated in a Y_2SiO_5 crystal was demonstrated in the year 2015 by Zhong *et al.* [106]. Photon echo experiments showed coherent optical control of the Nd ion that was coupled to the cavity structure. Long optical coherence times of 100 μs and narrow inhomogeneous linewidths were measured for the Nd ions that were coupled to the cavity. This demonstration showed that the near surface rare-earth ions behave similar to rare-earth ions in bulk crystals. The results obtained in this research show the potential of these cavity coupled rare-earth ions to be used for on-chip quantum light-matter interfaces.

A femto-second laser written waveguide, in a 10 mm long 0.05%Pr^{3+}:Y_2SiO_5 crystal at 3 K, was demonstrated by Corrielli *et al.* in 2016 [107]. Single mode waveguides working at 606 nm were fabricated by writing pairs of damage lines. The distance between the tracks were about 25 μm and they were about 100 μm deep. They showed that their waveguide fabrication technique didn't affect the coherence properties of the Pr^{3+} ions significantly. The $^3H_4 \leftrightarrow {}^1D_2$ transition of Pr^{3+} ions was probed and the observed inhomogeneous linewidth in these waveguides was about 20 GHz, which is comparable with the bulk sample measurements with the same doping concentration. The observed coherence time was about 49.9 μs, which is smaller than the measured 120 μs coherence times observed in bulk samples with

similar experimental conditions.

One of the advantages of the TeO_2 slab waveguide deposited on a bulk Pr^{3+}:Y_2SiO_5 crystal over other rare-earth waveguides is that it is largely independent of a particular rare-earth ion doped crystal. Hence, the same waveguide system can be fabricated using other host crystals and rare-earth ion dopants such as Er^{3+} doped crystals, which work at the communication wavelength of around 1550 nm.

2.7 Linear coherent quantum memory techniques

A quantum memory is used to temporarily store the quantum state of a photon, as well as other quantum states of optical fields, in an efficient and reliable manner, and then release the quantum information on demand. This device is essential in all quantum repeater complex protocols, which involve the creation of the photons, processing the information and transmission to the receiver.

In the pursuit of implementing quantum memories, two general approaches are being investigated: single-site [108, 109] and ensemble-based [26, 110, 111]. The ensemble approach has the advantage that coupling in and out of such devices is much easier and can be performed with relatively common optical elements, due to the size of input and output beams. It is the ensemble approach that is the motivation for the current work.

In the ensemble approach solid state systems and hot and cold atomic gases are widely researched. Solid state systems are particularly appealing because integration is more practical in these systems. Progress in the field has been rapid, with demonstrations of long storage times [14, 54, 112, 113, 114], high efficiencies [26, 115, 116], highly multimode quantum memories [117] and different experiments including entangled states [16, 60, 118, 119, 120].

An important parameter in quantum memories is their efficiencies. The efficiency of a quantum memory is described by the energy ratio of the input (stored) and output (recalled) light pulses. The highest measured efficiency in a rare-earth ion doped quantum memory is 69% achieved in a Pr^{3+}:Y_2SiO_5 [26] crystal.

Two other important criteria for the implementation of the quantum memory are the bandwidth and the longest time interval that the signal can be stored. This gives the time-bandwidth product. The spectral bandwidth where the memory operates efficiently is the memory bandwidth. The bandwidth of the memory determines the amount of quantum information that can be stored in the memory. The band-

width is referred to as the multimode capacity of the memory. Also, the upper limit for the longest time interval that a signal can be held is the coherence time of the optical transition.

A quantum memory should be able to hold quantum information long enough to perform a certain task. In rare-earth ion doped crystals, the storage time can be extended to quite long times on the order of hours if the coherence between the states is transferred to the hyperfine levels [14]. This is due to the long coherence times between the ground state hyperfine levels in these materials.

2.7.1 Photon echo based quantum memories

There are numerous techniques for implementing quantum memories in solid state ensembles. Some of these coherent quantum memory protocols, which use photon echos to operate, are Controlled Reversible Inhomogeneous Broadening (CRIB) [26, 121, 122, 123]; Rephased Amplified Spontaneous Emission (RASE) [27, 29, 30, 111]; Hybrid Photon-Echo Rephasing (HYPER) [124]; Revival Of Silenced Echo (ROSE) [125, 126]; Atomic Frequency Comb (AFC) [110, 117, 127, 128].

The photon echo based memory depends on a procedure that rephases the atoms and emits an echo of the input light at a later time, which recreates the initial coherence in the ensemble. In this procedure, the atoms are re-phased at a later time by applying a sequence of pulses to the ensemble. This re-phasing of the atoms causes the emission of the input absorbed light carrying quantum information. The photon echo based quantum memories which will be discussed further are the atomic frequency comb (AFC), the controlled reversible inhomogeneous broadening (CRIB), and the Rephased Amplified Spontaneous Emission (RASE) techniques.

2.7.1.1 Atomic Frequency Comb

In the atomic frequency comb (AFC) protocol, the atoms in the media are distributed over the detuning δ on a periodic comb like structure, which has the absorption lines in the material spaced by Δ as shown in Figure 2.11. In this case, re-phasing is repeated at times of $2\pi/\Delta$. Therefore, the accumulated phases by atomic dipoles in different comb structures are separated by multiples of 2π. If long term storage and on demand read out is required, the excited optical coherence can be transferred to hyperfine ground levels in the atomic system [110]. This can be achieved in rare earth ion doped crystals. The AFC protocol is based on the three

pulse photon echo sequence which was discussed in Section 2.4.2.2 [129, 130, 131].

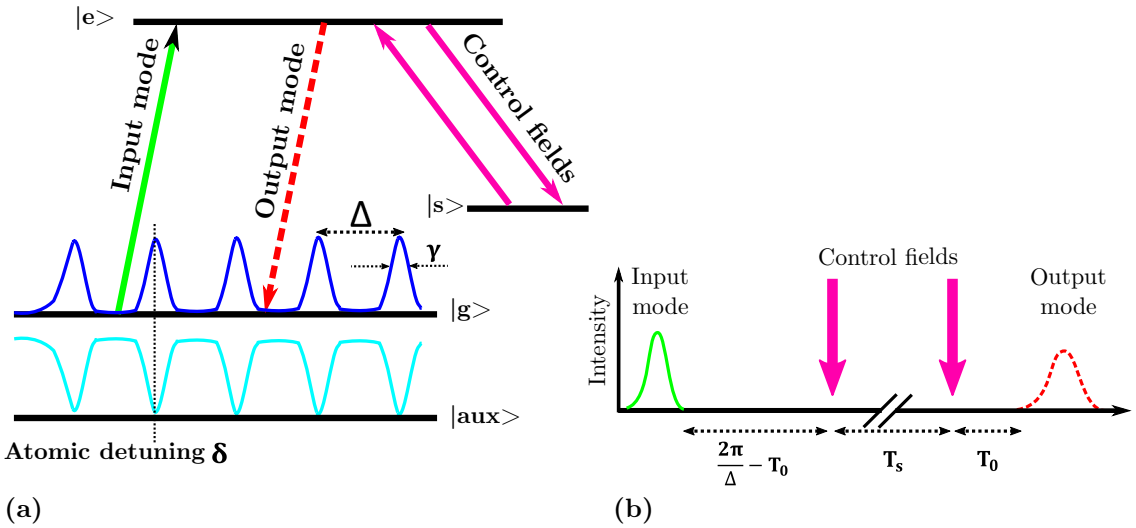

Figure 2.11: Atomic frequency comb quantum memory, (a) A pattern shaped like a comb is prepared on the inhomogeneous line by optical pumping at certain frequencies. The peaks are spaced by Δ and their width is γ. (b) The absorbed input mode goes out of phase very quickly and due to the comb like structure, it then rephases after a time $2\pi/\Delta$. This rephasing causes the input light to re-emit. The two control fields are at opposite directions so that long storage times of T_s and efficient readout is made possible in the backwards direction [110].

The atomic frequency comb based quantum memory was proposed by Afzelius *et al.* in 2008 [110]. The storage times in the original AFC experiments were fixed and limited by the optical coherence times of the material which was typically shorter than milliseconds.

In an effort to overcome the predetermined nature of the scheme, experiments were performed by Afzelius *et al.* [127], which proposed and demonstrated an extension to the scheme, where the excitation was transferred to the spin state, hence achieving longer storage times. Optical pulses with a duration of 450 ns were stored in a Pr^{3+}:Y_2SiO_5 crystal. The storage time was increased up to 20 μs. The total efficiency in these experiments was 2.8%. The bandwidth was about 2 MHz for input pulses of about 450 ns.

Gündoğan *et al.* [132] have demonstrated a solid state optical quantum memory with on-demand read-out. This experiment was performed on a Pr^{3+}:Y_2SiO_5 crystal using the AFC protocol. They have been able to store weak coherent pulses at the single-photon level and the achieved signal to noise ratio was more than 10. A second Pr^{3+}:Y_2SiO_5 crystal was used to filter out the excess noise created by the control

pulses, by narrow-band spectral filtering based on spectral hole burning techniques. The storage times obtained in these experiments were about 7.8 μs. The total efficiency in these AFC memories was about 5.3%.

2.7.1.2 Controlled Reversible Inhomogeneous Broadening

Another quantum memory protocol based on photon echos is the controlled reversible inhomogeneous broadening (CRIB) [133]. In the CRIB protocol, the inhomogeneous detunings in an ensemble can be controlled. In general for CRIB the inhomogeneous broadening can be randomly distributed.

The CRIB protocol can be explained by the time-reversal symmetry property in the Maxwell-Bloch equations. This can be used to describe the evolution of an atomic system interacting with an input light field, when absorbing or emitting the initial photon [121]. In this case, similar to photon echoes described in previous Sections, the detuning of all the atoms has to be inverted. Furthermore, a phase shift of e^{-2ikz_j} is applied to the atomic system. During the absorption of light by the atomic system, a collective coherence is created. This atomic coherence on the forward traveling optical field has to be mapped onto a backward traveling light field, which causes the coherent photon echo to be emitted from the atomic system. This method requires high absorption in the medium, therefore high optical depth in the material is required.

In CRIB, the atomic absorption for each position along the direction of propagation (z) in the medium is narrow and therefore the resonance frequency throughout the medium can be written as $\delta_j = \chi z_j$ and varies monotonically through the medium. Here χ is a proportionality coefficient. This broadening generates an efficiency of $\eta^{(t)} = (1 - exp(-(\alpha L)_{eff}))^2$. In this equation the effective optical depth of the medium is $(\alpha L)_{eff} \propto \chi^{-1}$. It can be observed that the efficiency of the forward traveling pulse can reach 100%, while the the re-emitted output pulse, which is a time reversed image of the input light pulse [134], is emitted in the forwards direction.

If the broadening is correlated with the spatial position in the storage medium, the protocol is known as the gradient echo memory (GEM) [134]. For a gradient echo memory to operate, the conditions of atomic inversion, large optical depth and phase matching are essential. The optical depth of the medium determines the efficiency of the obtained quantum memory using this protocol.

In the GEM protocol, the evolution of the absorbing ions in a rare-earth crystal

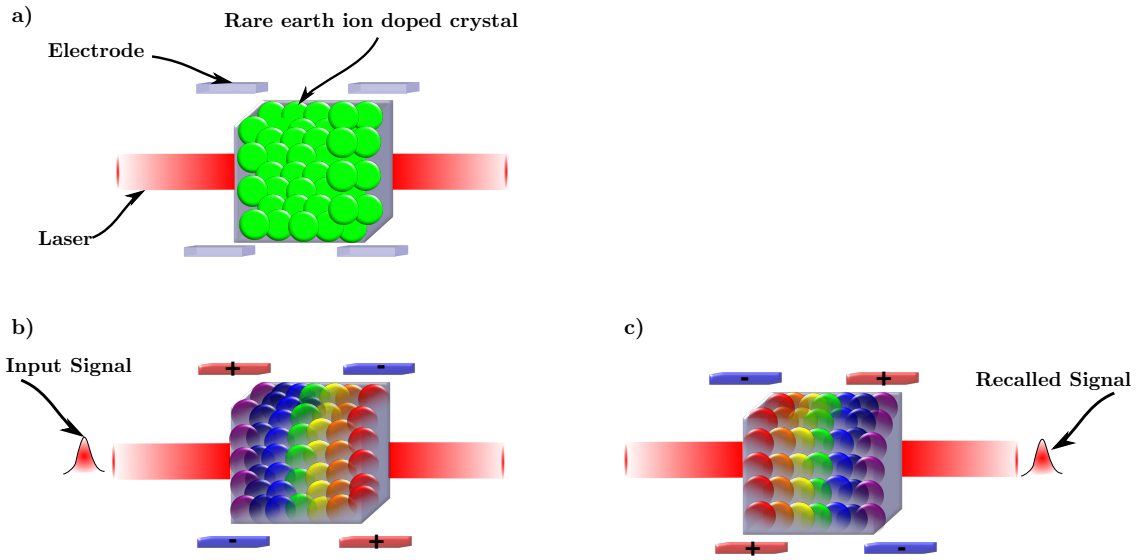

Figure 2.12: Gradient echo memory, (a) A rare-earth ion ensemble with a large inhomogeneous linewidth and four electrodes placed around the crystal, (b) Electrodes are turned on, hence the ions with the selected frequency form a linear frequency gradient that can absorb an input signal, (c) The voltage polarity is exchanged, causing the gradient to flip and an echo of the signal is emitted. Note that the colors are exaggerated for clarity.

can be controlled by an external electric field. A broad trench is initially created by linearly detuning a narrow absorption line with respect to the propagation depth, creating a detuning gradient. If this detuning gradient is reversed, an echo of the absorbed radiation by the created spectrum is produced. This is in fact reversing the evolution of the absorbing ions. The initial spectrum's shape is very important in the GEM protocol, because the efficiency and storage time of the quantum memory is dependent on the spectral sharpness and optical thickness of the medium, respectively. A GEM is simply illustrated in Figure 2.12.

Furthermore, the bandwidth of the stored light pulse is determined by the extent of the broadened line, which has to be very large. Initial large optical broadening of the absorption line reduces the optical depth, but by moving the coherence between the optical states to the hyperfine levels in the ground state, the initial line can be broadened and the storage time is increased without affecting the optical depth of the material.

The first experimental demonstration of CRIB was achieved by Alexander *et al.* in 2006 in a Eu^{3+}:Y_2SiO_5 crystal [135]. Due to the low optical depth of the crystal, the output emitted light pulse was six orders of magnitude smaller than the input light pulse. In the next year, Alexander *et al.* demonstrated that the phase

and amplitude of the input information carried by the light field can be stored in the crystal [136].

In 2008, Hétet *et al.* [137] demonstrated a CRIB based quantum memory with total and recall efficiencies of 15% and 26%, respectively. In this experiment a 0.05%Pr^{3+}:Y_2SiO_5 crystal was used. It was shown that an efficiency of 100% was possible by Stark shifting an ensemble of two level atom systems using an externally applied electric field. It was suggested that the no-cloning limit can be exceeded by improving the experiment.

In 2010, Hedges *et al.* demonstrated a gradient echo quantum memory, with record efficiency of 69% and low noise, in a Pr^{3+}:Y_2SiO_5 crystal [26]. The maximum achievable bandwidth was about 1.6 MHz. The storage times achieved were about 1.3 μs.

Another demonstration of CRIB was performed by Lauritzen *et al.* in an Er^{3+}:Y_2SiO_5, which has a transition wavelength at 1536 nm, close to the communication wavelength of 1550 nm [138]. However, the tailoring of the absorption line in these crystals is not as easy as in Pr^{3+} or Eu^{3+} doped crystals. The efficiency of the retrieved pulses in these experiments was below 1% for storage times up to 650 ns. The bandwidth in these experiments was about 1 MHz.

2.7.1.3 Rephased amplified spontaneous emission quantum memory

The rephased amplified spontaneous emission (RASE) scheme was first proposed in 2010 by Ledingham *et al.* [30]. In this protocol, the detected amplified spontaneous emission (ASE) of an ensemble is used to produce a collective atomic state. The RASE scheme can be used to build the entangled photon pair generator with built in quantum memory that is required for a quantum repeater node. It can also be used as a single photon source, and combined with other quantum optical devices to create a quantum information device.

A basic schematic of the RASE scheme is illustrated in Figure 2.13. At first, all the atoms in the two-level system are in the ground state of $|g\rangle$. An inversion pulse, resonant with the transition frequency, is then applied to drive all the atoms to the excited state of $|e\rangle$. After some time has passed, a photon is emitted from the atom that has spontaneously decayed down to the initial ground state. A collective state of the ensemble of atoms is heralded by the detection of the amplified spontaneous emission (ASE) photon. The created collective excitation of atoms is read out at a later time by applying a rephasing pulse resonant with the transition

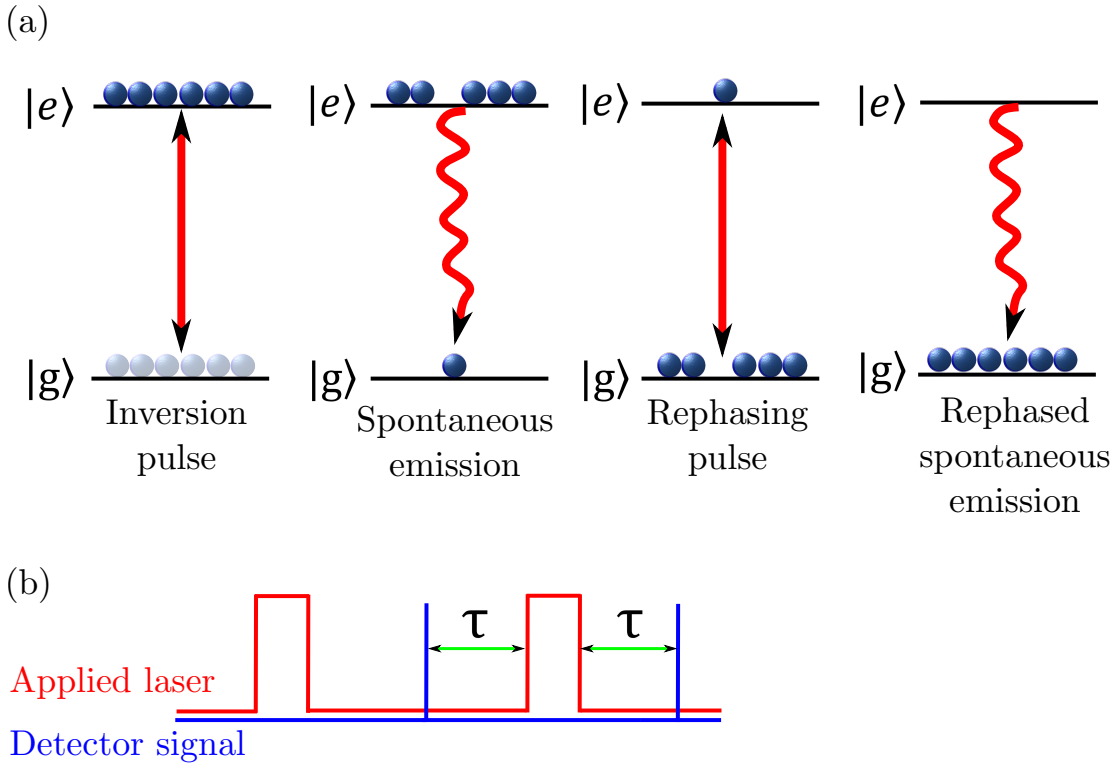

Figure 2.13: Rephasing spontaneous emission protocol, (a) An ensemble of atoms are driven to the excited state by an inversion pulse resonant with the transition frequency. A collective state of the ensemble is created by the detection of the spontaneously emitted photon. Then, the created collective excitation is read out by applying a rephasing signal. A rephased spontaneous photon entangled with the first spontaneously emitted photon, is then emitted. (b) The applied pulse sequence in time. [139]

frequency. After which, another photon is emitted after the atoms decay back down to the ground state. The rephased amplified spontaneous emission (RASE) photon is emitted symmetrically in time relative to the applied rephasing pulse. The ASE and RASE photons have been shown to be entangled[30, 139].

In 2016, Ferguson *et al.* demonstrated entanglement generation and storage in a Pr^{3+}:Y_2SiO_5 spin-wave quantum memory using the RASE protocol. In this experiment, an ensemble of Pr^{3+} ions in Y_2SiO_5 was inverted producing the amplified spontaneously emitted photon (ASE). The ensemble was rephased at a later time with a four-level photon echo pulse sequence. In this experiment, entanglement was demonstrated between the ASE and RASE photons, and after storage of the RASE photon, as a spin wave, for up to about 5 μs, the inseparability violation was maintained. It was shown that RASE is multimode in time and the two modes can be distinguished extremely well. This experiment paves the way towards the potential for multimode rare-earth quantum memories that can be used in scalable

quantum networks [111].

All these described quantum memory protocols, store quantum information in a collective atomic coherence in an ensemble. Hence, the storage times of all these schemes depend on the coherence times of their respective atomic systems. Recently, Zhong *et al.* have demonstrated storage times of up to 6 hours in Eu^{3+}:Y_2SiO_5 using a superconducting magnet cryostat and by applying a particular magnetic field to the crystal [14].

At the moment, the different quantum memory protocols are being investigated in various atomic and solid state systems. There has been a lot of progress in this field, very long storage times [14, 140, 141], high efficiencies [116, 142] and multimode quantum memories [117] have been experimentally demonstrated. The next Section describes some of the progress towards making quantum memory waveguides using rare-earth ion systems.

2.7.2 Quantum memories using rare-earth ion doped waveguides

In the pursuit of solid state integrated quantum communication devices, a waveguide of Tm^{3+}:Ti^{4+}:$LiNbO_3$ was designed and combined with the photon-echo quantum memory protocol based on an Atomic Frequency Comb(AFC) to obtain a quantum memory [16]. In this device, the memory bandwidth was increased from 100 MHz to 5 GHz. This experiment showed evidence that Bell's inequality had been violated, and hence entanglement had been preserved in these quantum memory waveguides. The storage time obtained in these waveguides was about 7 ns, which is pre-determined by the separation between the teeth in the AFC which is about 143 MHz. This quantum memory doesn't have on demand readout.

In an experiment performed by Sinclair *et al.* [104], a Tm^{3+}:Ti^{4+}:$LiNbO_3$ waveguide was examined at a temperature of 800 mK. The bandwidth in these AFC waveguides was about 0.1 GHz with a storage time of 100 ns which has to be further increased for quantum repeater applications.

Laser written waveguides using Pr^{3+}:Y_2SiO_5 were demonstrated by Corrielli *et al.* [107]. Storage of light pulses using the AFC protocol were performed in these waveguides. The obtained storage times were about 15 μs. The maximum efficiency of the spin-wave signal is about 2%.

Cavity QED experiments using an Er^{3+}:Y_2SiO_5 crystal were demonstrated by

Probst *et al.* [143]. In this experiment, a cylindrical copper waveguide resonator was magnetically coupled to the electronic spins of Er^3. Superconducting quantum processors could be achieved using these waveguide cavities. Microwave and optical quantum memories and optical to microwave interface circuits could be built using the spins in these rare-earth ion doped crystals in 3 dimensional quantum circuits. These waveguide cavities are very promising for quantum integrated devices, because Er^3 has the longest measured optical coherence time of 6 ms close to the telecommunication wavelength of 1550 nm, which makes it easier to couple these quantum memory waveguides to the existing telecommunications technology. Also, these quantum memories could be integrated with the developing 3 dimensional superconducting qubits technology.

To date, an on demand readout memory on a waveguide has not been demonstrated. Also, from the above storage time, bandwidth and efficiency values, a quantum memory waveguide that is practically useful for quantum repeater applications has not been demonstrated yet. To be able to use these quantum memories in quantum repeaters, the storage times should at least be on the order of seconds to make sure that no errors are introduced into the system. Furthermore, the efficiency of the quantum memory has to be significantly increased, so that quantum information is not lost during transmission. Also, the time-bandwidth product of the memory must be increased so that more information can be stored.

2.8 Summary

From the literature review presented in this chapter, it can be concluded that fabrication of waveguide devices for quantum memories using rare-earth ion doped crystals is possible. The results of these experiments showed that reasonable coherence times can be achieved in waveguides built using rare-earth ions.

In moving towards waveguide fabrication, host crystals with low intrinsic inhomogeneities are ideal. Most of the demonstrations reviewed in this chapter had used $LiNbO_3$ as the host crystal for rare-earth ions. It was discussed that the intrinsic disorder of $LiNbO_3$ crystals caused the inhomogeneous linewidth to be very large compared to Y_2SiO_5 host crystals. Hence, the fabricated waveguide presented in this thesis used Y_2SiO_5 as the host crystal.

The aim of the work presented in this thesis was to fabricate a gradient echo memory on a waveguide platform. In the next chapter, the material properties of the rare-earth ion doped system used to fabricate the waveguides will be discussed. In

addition, the complexities of the design and fabrication of these planar waveguides will be explored.

Chapter 3

Proposed Linear Optics Quantum Processor Architecture

3.1 Introduction

A successful quantum repeater needs single photon sources, quantum memories with long storage times and detectors at each node. All of these individual components need to be highly efficient for the whole quantum repeater to perform better than direct transmission of quantum information between two links. A practical quantum repeater also requires complex operations to be performed at each local node. These operations include entanglement swapping and quantum distillation. Currently, there is no way of performing the required operations including two-qubit gates deterministically, but it is possible to build a quantum processor using non-deterministic gates. It was proposed by Knill, Laflamme and Milburn (KLM), that non-deterministic quantum processors can be built using linear optics [144].

In the KLM scheme, the optical modes of photons, vertical and horizontal polarizations for example, are used as qubits that are to hold the quantum information and the operations performed using these qubits are called quantum gates. In a quantum repeater node, entanglement swapping (local joint measurements on the entangled states) between two quantum memories has to be performed. Such operations are possible by using two-qubit probabilistic quantum gates between the two memories [6, 145].

To fully operate the KLM proposal using non-deterministic gates, a linear optics quantum information processing unit consists of single photon sources, quantum memories, photon detectors, and passive elements such as beam splitters and phase shifters. To construct these complicated circuits and reduce the loss due to coupling in and out of bulk devices, it would be ideal to build an integrated chip containing all the necessary components on the same platform, rather than free space components.

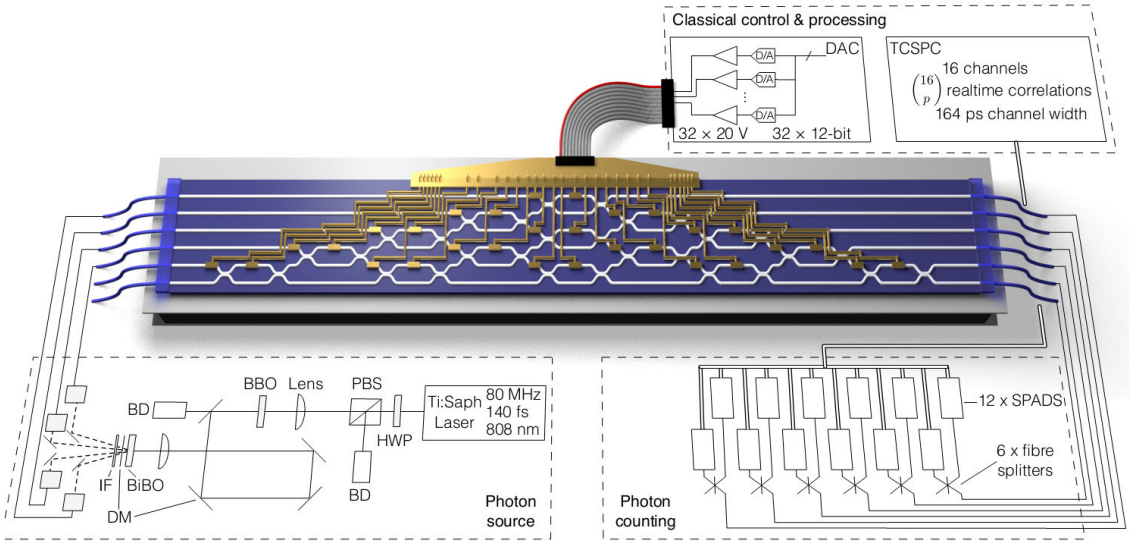

Figure 3.1: An alternative approach to building an optical quantum information processor unit has been built by Carolan *et al.*. In this architecture, photon pairs are generated using spontaneous parametric down conversion. Created photons are then transmitted through an array of polarization maintaining fibers to the linear optical processing unit (LPU). The LPU consists of 30 thermo-optical phase shifters controlled by a digital to analog convertor (DAC) unit off the chip. 15 of these phase shifters form 15 Mach-Zehnder interferometers. Photons to be measured are coupled out of the LPU using another array of fibers and transmitted to photon counting detectors off the chip [146].

In this chapter, I am proposing how KLM processing units can be designed using rare-earths to build a quantum repeater.

A state of the art linear optical quantum information processor unit built by Carolan *et al.* is shown in Figure 3.1 [146]. This passive integrated photonic chip is a silica on silicon waveguide circuit, working as a single mode waveguide at the wavelength of 808 nm. Polarization maintaining fibers are connected to the input and output channels of this waveguide circuit, with coupling losses of about 9% for each fiber. This chip has a maximum of six inputs, and consists of an array of 30 waveguide directional couplers and 30 thermo-optic phase shifters. These thermo-optical phase shifters are controlled by thermo-optical heaters, fabricated on top of the waveguide and controlled by an electrical circuit providing the voltage required for any desired phase shift. 15 of these phase shifters create 15 Mach-Zehnder interferometers on this integrated chip. The fiber to fiber loss in this system is about 42%. This integrated chip is reprogrammable and was programmed to realize heralded quantum logic and entangled quantum gates, among other complex processes [146].

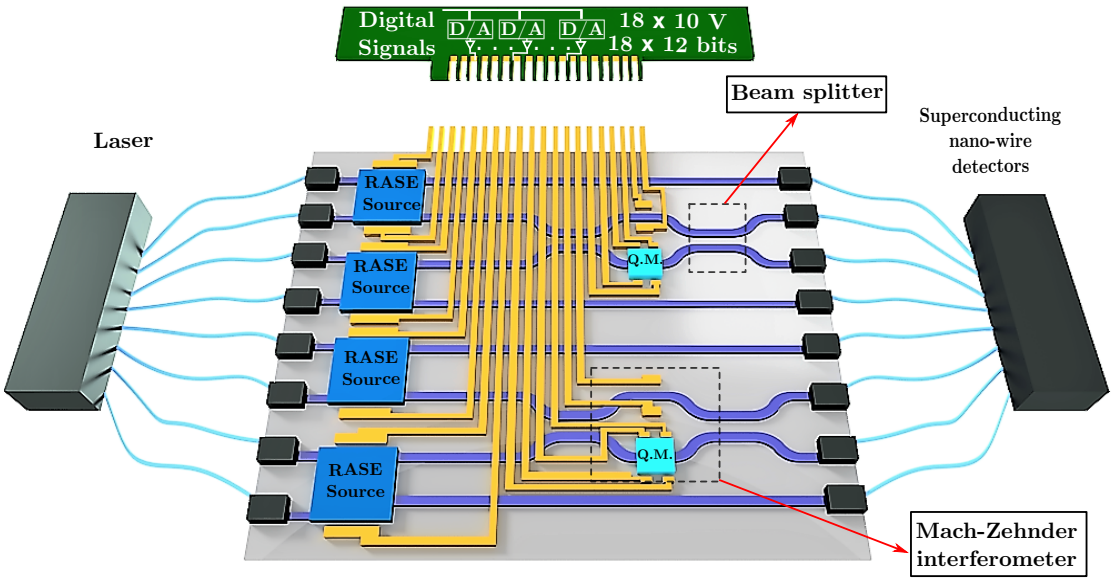

Figure 3.2: Linear optical quantum processor. This integrated chip includes 4 RASE photon sources, 2 quantum memories, 4 beam splitters and 2 Mach-Zehnder interferometers. In this chip, the superconducting nano-wire detectors and the electronic control circuitry are off-chip.

To implement the full KLM scheme, due to the non-deterministic nature of events, quantum memories are essential. This integrated chip doesn't have a quantum memory. It is possible to use delay lines instead of quantum memories on this chip, but that would require fast switches, not available on this integrated circuit. The thermal switching speeds are slow compared to the photon packet size and there is no way of acquiring any feedback to the system in real time. Also, this linear optics processor unit is a hybrid device with on chip and off chip components, with the photon source and the photon counting detectors off the chip, which leads to coupling losses. In this chapter, I outline a proposal for a linear optical quantum processor using a rare-earth ion doped integrated platform. This integrated chip can bring the photon sources and quantum memories together with classical control elements such as modulators and switches, and passive elements such as beam splitters and phase shifters on to one processor chip. This platform uses the long storage times of rare-earth quantum memories. Also, different devices on the chip can be controlled by electrical fields inducing Stark shifts on the ions.

The proposed linear optics quantum processor architecture of this chapter is shown in Figure 3.2. In this system, the single photon sources and quantum memories, as well as passive elements such as beam splitters, are on the same chip. As can be observed, these components are controlled by electronic circuits similar to what was required in the chip of Figure 3.1. These components are briefly introduced in

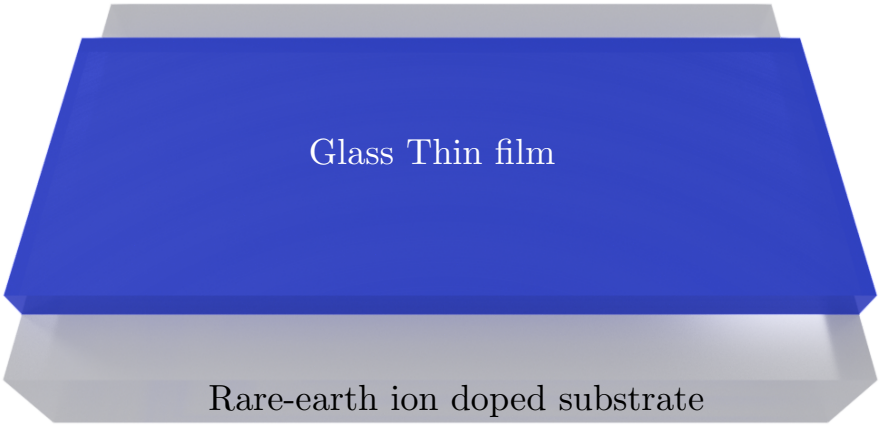

Figure 3.3: A simplified illustration of the waveguide. TeO_2 glass thin film deposited on a Pr^{3+}:Y_2SiO_5 substrate.

later Sections.

3.2 Waveguide design

In the waveguide design proposed here, thin films of high refractive index glass were deposited on rare-earth ion doped substrates. This approach combines the unique optical coherence properties of rare earth ion dopants in high-quality single crystals with the glass waveguide, the fabrication of which has been studied extensively in the optical communications industry [24, 147, 148]. A simple illustration of the waveguide is shown in Figure 3.3.

To build an operational integrated quantum information processor, it will be necessary to be able to design active elements independently from each other. This will require spatially isolating the devices by having passive waveguides linking active regions. In the proposed waveguide structure, isolated elements can be fabricated on the chip by tapering the waveguide region [149] and lifting the light field in and out of the active substrate in three dimensional space as shown in Figure 3.4.

A notable advantage of the passive waveguides is that the technique is largely sample independent. Any high refractive index glass used as the thin film could be combined with any rare-earth ion doped crystal as the substrate, as long as an appropriate index mismatch is achieved.

The waveguides designed in this thesis were thin films of TeO_2 with a refractive index of 2.05 deposited on Pr^{3+}:Y_2SiO_5 substrates with a refractive index of 1.806. The rare-earth ions of Pr^{3+} were probed by the evanescent field of light extending

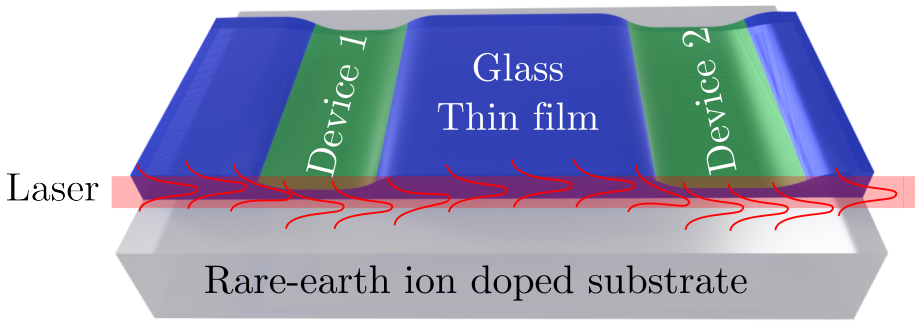

Figure 3.4: A simplified illustration of 2 separate devices fabricated by tapering the waveguide. By reducing the thickness of the thin film, the evanescent tail of the light field is pushed into the substrate, probing the active rare-earth ions.

into the substrate.

3.3 Time scale of operations

For successful quantum communication, entanglement has to be spread throughout the whole network. For this to be possible, the quantum memories in each node, must be able to hold the quantum information long enough for entanglement to be established in their neighboring nodes and in the entire network. The performance of quantum repeaters was analyzed by Razavi *et al.* [150] in 2009. It was found that the repeater rate decays exponentially to the power of $exp(-\sqrt{L/c\tau})$ ($\tau \ll L/c$). In this formula, L is the total distance of the link, τ is the quantum memory storage time and c is the speed of light. Rare-earth crystals have demonstrated long coherence times of up to 6 hours [14], making them a very capable system for this purpose.

The time scale of entanglement swapping operations in each quantum repeater node depends on the time-bandwidth product of the quantum memories used in the links. In rare-earth quantum memories the bandwidth is from MHz to hundreds of MHz. For example, a bandwidth of 1.6 MHz was reported in the quantum memory built by Hedges *et al.* [26]. In that particular memory, the maximum bandwidth that was potentially possible was limited by the hyperfine structure of the crystal to about 10 MHz. The bandwidth of a rare-earth GEM can be increased by either using crystals with Kramers ions with larger hyperfine splittings like Er^{3+} ions [26], or by growing better quality crystals with lower inhomogeneous broadenings, which are narrower than the hyperfine splittings of these systems [25]. In these high quality crystals, the memory bandwidth depends on the optical depth and the amplitude

of the electric gradient causing a Stark shift. Stoichiometric rare-earth crystals that are isotropically pure with low inhomogeneous linewidths are being developed as shown in Reference [25].

3.4 Electronic control

Using Stark shifts, external electrical signals would allow the control of the various components required in an integrated quantum device by fast and local electronic manipulation of rare-earth ion ensembles, bringing the ions in and out of resonance with the laser source rather than modulating the source. Using Stark shifting in rare-earth ion doped devices, coherent transients have been demonstrated [74], spectral and temporal shaping of the ensemble can be achieved [28] and quantum protocols can be accomplished [26].

A very simple example of devices that can be built with this method are electrically controlled optical switches as shown in Figure 3.5. By switching the voltages between the electrodes at different times, photon echo signals can be retrieved at various times. When the voltage of a device is switched from low to high, the frequency of the ions in that device are moved into resonance with the excitation laser frequency. If the voltage of device 1 is switched on, and a sequence of $\pi/2$ and π pulses are applied, a photon echo can be retrieved from device 1. Now if device 2 is turned on at a later time, and the same pulse sequence is applied, device 2 also emits a photon at a later time compared to the first echo signal.

The applied Stark shift has to be much larger than the Rabi frequency of the optical field used to drive the rare-earth ions. For example, in Pr^{3+}:Y_2SiO_5, the Rabi frequency is limited to about 2 MHz due to the hyperfine structure. The Stark coefficient of Site 1 of 0.02%Pr^{3+}:Y_2SiO_5 was measured to be 111.6 KHz/Vcm^{-1} [4], so the required voltage to induce shifts of 2 MHz is about 18 Vcm^{-1}.

Assuming the Rabi frequency to be about 1 MHz, the switching times have to be faster than 1 μs (less than $\frac{1}{\text{Rabi frequency}}$), preferably on the order of tens of nano-seconds. Very low capacitance electrodes can be fabricated to increase the switching speed. Assuming a resistance of 50 Ω, and a frequency of $f = 10^9$ Hz, the capacitance required is 20 pF. This is a reasonably large capacitance and so fast switching should not be difficult. In Chapter 4, the design of an electrode structure to implement the required voltages and electric field calculations for a simple device are presented.

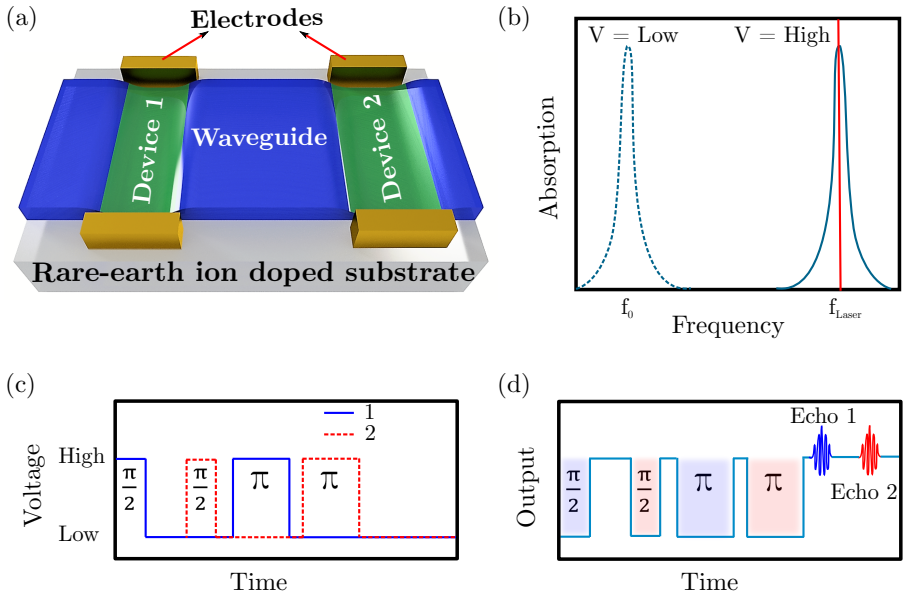

Figure 3.5: A simple example of two electrically controlled optical switches (devices 1 and 2) utilizing the proposed architecture for integrated rare-earth-ion quantum systems. Electrodes are incorporated with a waveguide-based platform to control individual components through the linear Stark shift of the ions. (a) Two photon echo devices are shown. (b) When the voltage is switched from low to high, the ions are shifted from f_0 into resonance with the excitation laser frequency f_{laser} (c) and (d) show an indicative time evolution of the applied voltage and waveguide output for the two photon echo devices. In (d) the absorption of the $\pi/2$ and π pulses decreases the output intensity and the photon echoes modulate the waveguide output because the coherent emission is at f_0.

3.5 Elements of linear optical quantum processor chip

In this Section, various elements required for the proposed linear optical quantum processor chip will be described. These components are parts of the chip shown in Figure 3.2.

3.5.1 Single photon source

Photon pair sources which create entangled photon pairs based on spontaneous parametric down conversion, are a common photon pair generator source in quantum repeater protocols [151, 152, 153]. However, the bandwidth of these sources is usually high, on the order of tens of THz. This bandwidth is much higher than the tens to hundreds of MHz bandwidths of quantum memories based on rare-earth crystals.

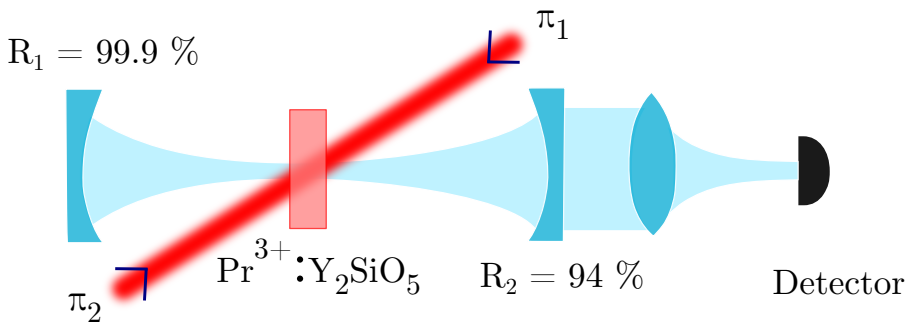

Figure 3.6: In cavity enhanced RASE, the crystal is situated in the middle of the Fabry-Perot cavity and the two preparation and rephasing pulses overlap in this region. Cavity enhanced RASE, improves the rephasing efficiency. This method also increases the signal to noise ratio of the RASE photon source [154].

The photon source of the proposed architecture will use the RASE protocol, which was described in Section 2.7.1.3. RASE in a rare-earth ion crystal has the advantage that the entangled non-classical states are generated and stored in the same protocol, and so the bandwidth is automatically correct [111]. Also, a photon pair generator based on spontaneous parametric down conversion is built using non-linear crystals, and so cannot be easily integrated onto a rare-earth platform. This would lead to increased coupling losses. The photon source based on the RASE protocol proposed here can be integrated on the same platform as the rare-earth quantum memory, reducing coupling losses between devices.

In RASE, by increasing the optical depth one should be able to increase the rephasing efficiency. But because the control fields and signals are all applied in the same mode, the rephasing π pulses end up distorted, potentially lowering the fidelity of the rephased emission. This issue can be avoided by placing the sample, creating the photon source using the RASE protocol, in a low finesse cavity, theoretically increasing the efficiency up to 100% [111]. This is achieved by applying the π pulses to the sample in a different off axis mode.

In cavity enhanced RASE, the ensemble is placed in a Fabry-Perot cavity, with the two rephasing and preparation pulses diagonally applied to the crystal, overlapping in the region where the crystal is situated, as shown in Figure 3.6. By changing the reflectivity of the cavity mirrors, one can determine which side the ASE and RASE photons will be emitted. The demonstration of a Cavity enhanced RASE by Ferguson *et. al* paved the way towards integration of single photon sources and quantum memories all on one rare-earth platform. Cavity enhanced RASE is discussed thoroughly in Reference [139].

Cavity enhanced RASE on chip can be designed as shown in Figure 3.7. The

active region can be tapered so that the two preparation and rephasing pulses will be overlapping in this region. Bragg gratings can be fabricated to work as the two cavity mirrors, and they can be designed in such a way that both ASE and RASE photons are emitted from one side or both sides, depending on the chip design.

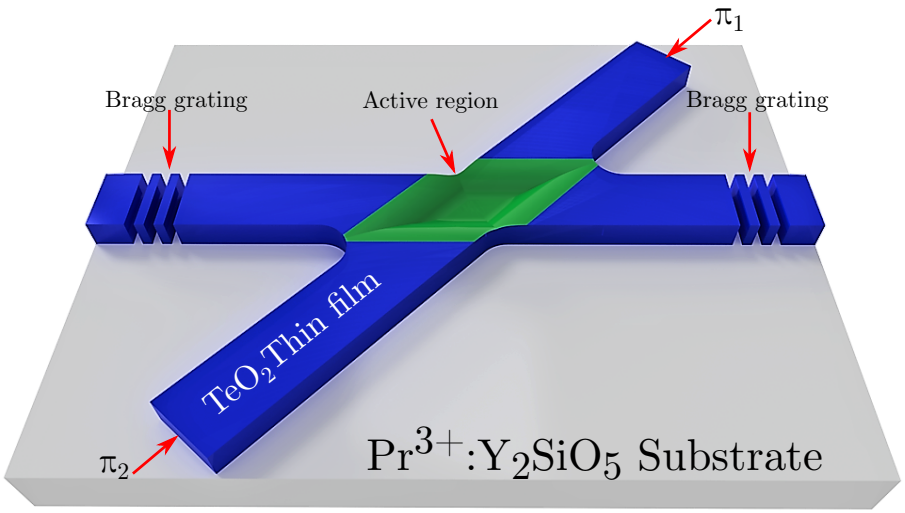

Figure 3.7: A photon source using the RASE protocol. Bragg gratings are used instead of the cavity mirrors. The active region can be designed by tapering the waveguide at the region where the two rephasing and preparation pulses overlap.

3.5.2 Quantum memories

As mentioned before, quantum memories are an essential component of a successful quantum repeater node. One must be able to store the generated entanglement while entanglement is being established in neighboring nodes. The storage time of the quantum memory must be long enough to hold the entanglement to allow entanglement swapping in the entire link to be performed. So it would be ideal for the memory storage time to be longer that the time required for the entanglement if the whole link to be established. In rare-earth ion crystals long coherence times on the order of hours [14] have been demonstrated, which makes them a very promising material for this purpose. Rare-earth ion based photon echo quantum memories have been described in Section 2.7.

A gradient echo rare-earth quantum memory on chip can be designed as shown in Figure 3.8. The electrodes are designed so that the rare-earth ions in the active substrate witness a linear electric field gradient going across the waveguide in

the propagation direction. Simulation results showing the linear electric field are presented in Chapter 4.

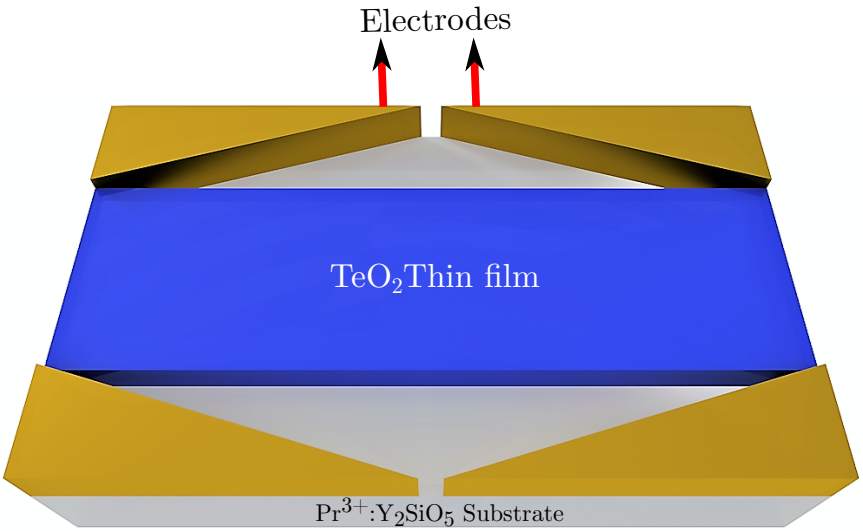

Figure 3.8: A waveguide gradient echo rare-earth quantum memory. Electrodes are designed such that a linear electric field gradient is placed on the waveguide.

3.5.3 Passive elements

Passive elements such as beam splitters and phase shifters are also required on a linear optical quantum chip. These passive devices can be used to control the light field, without the active rare-earth ions interacting with the light, using an external electric field. In the waveguide architecture proposed in this thesis, one can take advantage of the second order non-linearity χ^2 of the TeO_2 glass films, in which by applying a small electric field relatively large phase shifts can be produced [155]. Another method for phase shifting the light can be achieved by Stark shifting off-resonant absorption peaks of the rare-earth substrate, which would phase shift the light without exciting the active ions.

Beam splitters and Mach-Zehnder interferometer waveguides for amplitude modulation can be fabricated on the integrated circuit as shown in Figure 3.2. Using electrical control, light can be switched between different paths or switched on and off in one path. For example, to construct a Mach-Zehnder interferometer, the light in one arm can be phase shifted using small electrical fields by applying a certain voltage to the electrodes. Another method to induce amplitude modulation in the Mach-Zehnder interferometers can be by applying small magnetic fields one arm.

This can be achieved by placing a thin wire close to one arm, and running a small current through the wire.

3.5.4 Single photon detectors

Superconducting nano-wire single photon detectors (SNSPD) are a good candidate to be used for photon detection. The nano-scale size of these detectors make them highly sensitive to absorbing a single photon. SNSPDs can be designed to work at different wavelengths. SNSPDs are highly efficient, with reported efficiencies of more than 97% [156].

Ideally, the detectors should be on chip. Currently, the superconducting nano-wires used for these detectors can't tolerate the level of magnetic fields required to get the long coherence times of the rare-earth quantum memories. This means that unless superconducting nano-wires capable of remaining superconducting in magnetic fields larger than tens of Gauss become available, it will be necessary to have the detectors off chip to separate them from the rare-earth devices.

3.6 Summary

In this chapter, an alternative method of building a linear optics quantum processor chip has been presented. This passive waveguide architecture has the advantage that it is sample independent. Also, by tapering waveguide regions, isolated devices can be built on chip.

This method can bring non-classical single photon sources and quantum memories, required for a quantum repeater, on to the same platform. In this integrated circuit, the bandwidth of the photon generator and the quantum memories are automatically matched because they are both on the same chip.

The long storage times achievable using rare-earth ion doped quantum memories eliminates the need for high switching speeds and reduces the clock speed of the processor to a manageable speed. These long storage times give the quantum repeater node more robustness, ensuring that entanglement can be established in neighboring nodes and the entanglement swapping can be achieved between nodes.

The proposed architecture also incorporates passive elements like beam splitters and Mach-Zehnder interferometers onto the same integrated circuit. Using these

passive elements and electrical control, the light field can be manipulated in different parts of the beam path without interacting with the active ions.

Superconducting nano-wire single photon detectors (SNSPD) can be used to detect the output photons in this integrated chip. To-date, a SNSPD compatible with the magnetic field requirements of rare-earth ion doped quantum memories has not been built. So until this is achieved, the SNSPDs will have to be kept off chip.

In the next chapters, the proposed waveguide structure is investigated. First, the waveguide fabrication is presented and then the experimental analysis of the architecture is reported.

Chapter 4

Material Complexities and Fabrication of Rare-Earth Planar Waveguides

4.1 Introduction

The aim of this chapter is to introduce two rare-earth ion doped thin film approaches, as shown in Figure 4.1, and present some of the fabrication and material issues involved in each approach.

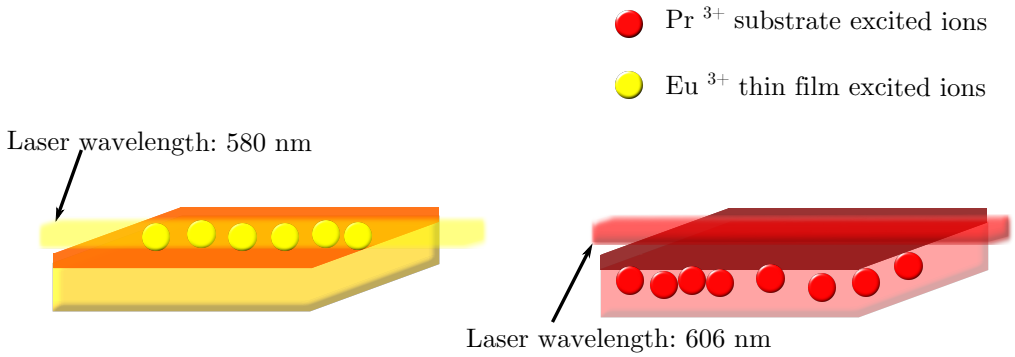

Figure 4.1: Two rare-earth ion doped thin film architectures, (a) For the active rare-earth ion waveguide, a thin film of Eu^{3+}:Y_2O_3 was deposited on a sapphire substrate. The Eu^{3+} active ions were then probed by a laser at its excitation wavelength of 580 nm, (b) For the passive rare-earth ion waveguide, a glass thin film of TeO_2 was deposited on a Pr^{3+}:Y_2SiO_5 substrate. The Pr^{3+} active ions in the substrate were then evanescently probed by a laser at its excitation wavelength of 606 nm.

The first method, which is primarily a PhD project conducted in the Laser Physics Center at the ANU by Paulraj *et al.* [23], was growing rare-earth ion doped

thin films on suitable substrates. These films were fabricated by depositing thin layers of Eu^{3+}:Y_2O_3 ($n_{thinfilm}$ = 1.95) on α-Al_2O_3 ($n_{substrate}$ = 1.76) substrates using the Pulse Laser Deposition (PLD) method. In these thin films, the preservation of the optical coherence properties of the rare-earth depends on the growth mechanism and the lattice mismatch between the thin film and the substrate. After the deposition, these films were characterized by X-ray diffraction and optical spectroscopy.

The second approach, which is the focus of this thesis, was depositing glass thin films of TeO_2 ($n_{thinfilm}$ = 2.05) on rare-earth ion doped single crystalline substrates of Pr^{3+}:Y_2SiO_5 ($n_{substrate}$ = 1.806). This method has many advantages to the previous approach, essentially avoiding issues caused by stressing the crystalline structure. Glass is a soft material compared to rare-earth crystals, so it can relax on the substrate and lattice matching is not essential. Even in the cold liquid helium temperatures needed for the experiments at hand, glass is still mobile. The characterization of these thin films will be presented in Chapter 6.

The deposition of suitable electrodes to produce the electric fields required to probe the substrate ions and Stark shift their frequencies is also presented. The material deposited to fabricate the electrodes on the glass thin films was gold. There were a few issues with the adhesion of these gold electrodes to the thin film surface, which had to be investigated and resolved.

4.2 Thin films with rare-earth doped crystal as active core

The first thin film fabrication method was primarily the PhD project of Paulraj [23] conducted in the Laser Physics Center at the ANU. This project involved attempting to grow rare-earth ion doped thin films on suitable substrates by Paulraj. The fabricated thin film was Eu^{3+}:Y_2O_3 on α-Al_2O_3 substrate. After fabricating the thin films, the crystalline quality of the thin films was examined using X-ray diffraction by Paulraj. I was involved in this project, specifically in the optical analysis of these thin films and will be briefly reporting the progress. First, in Section 4.2.1, Eu^{3+}:Y_2O_3 and its optical properties will be described. Then, in Section 4.2.2, the fabrication process and the optical inhomogeneous linewidth will be presented.

Bulk crystal	T_1 (μs)	T_2 (μs)	Γ_{IH} (GHz)	$\Gamma_{H(echo)}$ (kHz)	$\Gamma_{H(hole)}$ (kHz)
Eu^{3+}:Y_2O_3	900	510	5	0.62	< 1.75

Table 4.1: Spectral and relaxation parameters for the $^7F_0 \rightarrow {}^5D_0$ transition of bulk crystal 2%Eu^{3+}:Y_2O_3 [88].

4.2.1 Eu^{3+}:Y_2O_3

Y_2O_3 crystallizes in the cubic bixbyite structure and the unit cell contains 16 formula units (80 atoms) [157]. This crystal has a high melting point of $1200°C$ and therefore growing this crystal is extremely difficult [157]. The optical and hyperfine coherence properties of the bulk crystal Eu^{3+}:Y_2O_3 have been thoroughly investigated [22, 88, 158]. The optical transition of interest in these crystals was the $^7F_0 \rightarrow {}^5D_0$ of Eu^{3+}:Y_2O_3 at a wavelength of 580.89 nm. The spectral and relaxation properties of Eu^{3+}:Y_2O_3 grown by flame fusion are presented in table 4.1. In this table T_1 is the radiative lifetime.

4.2.2 Eu^{3+}:Y_2O_3 thin films

To preserve the optical and hyperfine coherence properties of the bulk crystal, the grown thin film has to maintain a single crystalline structure. Extensive research has been carried out at the University of Hamburg on crystalline rare-earth ion doped sesquioxide Pulsed Laser Deposition (PLD) grown films on α-Al_2O_3 and quartz substrates [157]. The main purpose of these projects was constructing solid state lasers and other luminescent devices using these thin films [157], and therefore the optical or hyperfine coherence properties of the developed thin films at liquid helium temperatures were not important and had not been investigated.

To fabricate thin films with the rare-earth ion doped crystal as the active material, a suitable substrate had to be selected. Two important criteria have to be met for this purpose:

- The substrate must have a lower refractive index in order to achieve waveguiding.
- The lattice symmetry and lattice constant of the substrate and thin film material must match, otherwise the obtained thin film becomes polycrystalline or amorphous rather than single crystalline.

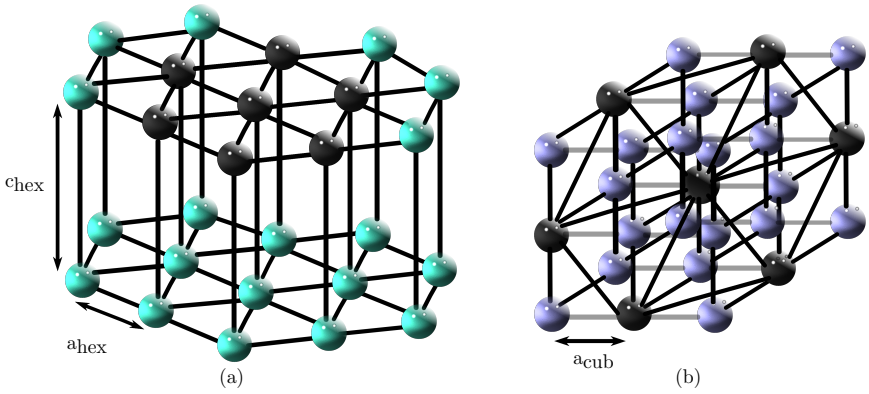

Figure 4.2: (a) Sapphire α-Al_2O_3 hexagonal crystalline structure, (b) Rare-earth cubic crystalline structure [157]. A particular characteristic face of the Eu^{3+}:Y_2O_3 crystal (shown by the black balls) can match the hexagonal structure of α-Al_2O_3.

One suitable substrate for constructing Eu^{3+}:Y_2O_3 thin film waveguides was sapphire, the α state of Al_2O_3. The refractive indices of Y_2O_3 and α-Al_2O_3 are 1.95 and 1.76 respectively, so this selection gives a suitable structure to achieve waveguiding.

The unit cell of α-Al_2O_3 has trigonal symmetry, with two Al_2O_3 units. Therefore, it can also be viewed as having a hexagonal lattice. As can be observed from Figure 4.2, the crystal structure of α-Al_2O_3 and a rare-earth crystal, for example a Eu^{3+}:Y_2O_3 crystal with a cubic bixbyite structure, can be matched (as indicated by the black colored atoms).

The lattice mismatch parameter, shown in Equation 4.1, can be used to characterize the different material combinations and the resulting lattice mismatch between these materials.

$$\text{lattice mismatch parameter} = \frac{\sqrt{2}a_{cubic} - 3a_{hex}}{\sqrt{2}a_{cubic}} \tag{4.1}$$

The lattice mismatch parameter for Y_2O_3 and α-Al_2O_3 was calculated to be 4.74%. which is an acceptable mismatch.

4.2.2.1 Thin film growth method and results

In an attempt to grow rare-earth ion doped thin films, the Pulse Laser Deposition (PLD) method was used by Paulraj. The type of material that can be fabricated with this method is restricted by the absorption of the material in the U.V. wavelengths and the melting point of the crystals [159]. A simplified schematic of the chamber

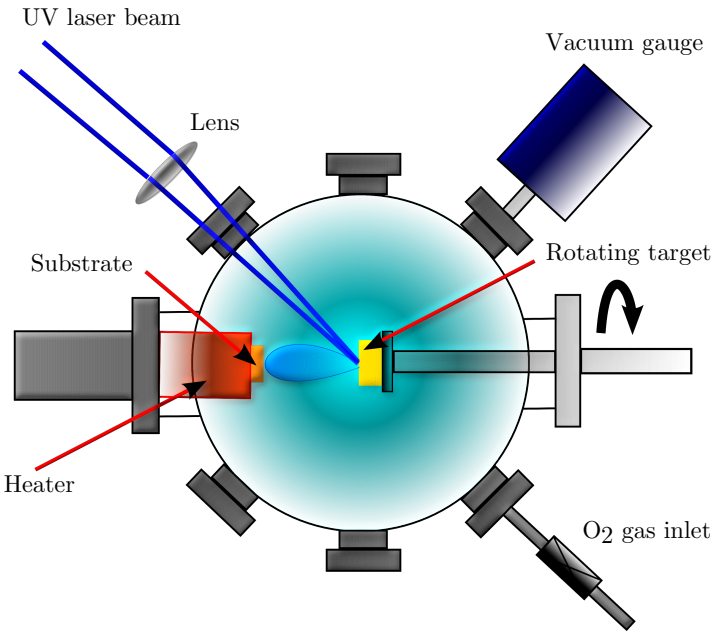

Figure 4.3: Schematic of the Pulse Laser Deposition device. A UV laser source is used to ablate the target creating a plasma plume of atoms that is deposited on the substrate.

in which the thin film was developed can be observed in Figure 4.3. The target was placed in an ultrahigh vacuum chamber with a base pressure of 4.3×10^{-5} Pa $\sim 5.6 \times 10^{-5}$ Pa. The target was on a rotating stage and was then struck by a focused ultraviolet pulsed laser beam, with a wavelength of 248 nm. In this method, after the target is struck by the U.V. laser beam pulses, the atoms and ions ablate from the target forming a plasma plume and deposit on the substrate. The laser shot frequency was varied, 500 pulses were shot with the frequency of 1 Hz, followed by 950 shots with the frequency of 5 Hz. The variation in frequency allows the first few layers of material to be deposited slower, so as to achieve better quality crystals.

The substrate was placed on a holder, which was placed in front of a heater with a variable temperature. The temperature of the heater was varied between 650°C $\sim$ 1000°C. There was a small (few millimeters) distance between the heater and the substrate, therefore the temperature of the substrate was lower than the acquired temperature from the heater sensors. The distance between the target and the substrate was 4 cm. Thin films with thicknesses of 100 nm $\sim$ 1250 nm have been grown using this method by Paulraj [23].

The group at the University of Hamburg characterized the structure of their fabricated thin films, using X-ray diffraction, Rutherford backscattering, atomic

force microscopy and optical spectroscopy at room temperature [157]. It was found that the quality of the fabricated thin films depends on a number of things such as the substrate temperature in the growth process, the lattice mismatch between the thin film and the substrate, the effects of the growing thin film surface during the growth process, etc..

In this group, the optical spectroscopy measurements were conducted at room temperature using a florescence spectrometer in the visible and ultraviolet range. The emission spectrum of 4%Eu^{3+}:Y_2O_3 thin films, with a thickness of 500 nm, grown on α-Al_2O_3 were compared to bulk samples of 1%Eu^{3+}:Y_2O_3. The thin films that were grown at a temperature of 700°C had an emission spectrum that was slightly broader than the bulk samples. Thin films grown in room temperature were completely amorphous and had no sharp emission peaks [157]. These results agreed well with their other characterization methods, indicating that by increasing the growth temperature the quality of the crystal improves.

To observe the optical properties of the thin film grown by Paulraj [23], the inhomogeneous linewidth was measured. This was simply achieved by looking at the emission of the thin film when being excited with a laser tuned to the optical transition of $^7F_0 \rightarrow {}^5D_0$ of Eu^{3+}:Y_2O_3 which occurs at 580.89 nm. The inhomogeneous linewidth of these thin films was measured at room and liquid helium temperatures (2 K) as shown in Figure 4.4.

The inhomogeneous line was about 300 GHz, broadened by about 2 orders of magnitude compared to the bulk crystal with inhomogeneous linewidths of 10 GHz at liquid helium temperatures. The large inhomogeneous broadening suggested that the thin films may be either polycrystalline or amorphous.

Thin films and nano-crystals have similar size. So, a comparison of the thin films and nano-crystals can be a good indication of the quality of the thin films. In 2013, Perrot *et al.* reported an inhomogeneous linewidth of 17 GHz in 60 nm nano-crystals of 0.86%Eu^{3+}:Y_2O_3 at a temperature of 3.5 K. This is a very narrow linewidth observed in a nano-crystalline structure and is close to the bulk sample linewidth, with similar doping concentrations. The results of these experiments indicate that our thin films probably have a structure that is more disordered than these 60 nm nano-crystals.

The possible thin film growth mechanisms are briefly illustrated in Figure 4.5. The formation of clusters and re-evaporation processes from the substrate can cause stress on the thin film and result in large excess inhomogeneous broadening. According to the obtained results, the thin film is either polycrystalline or completely

amorphous.

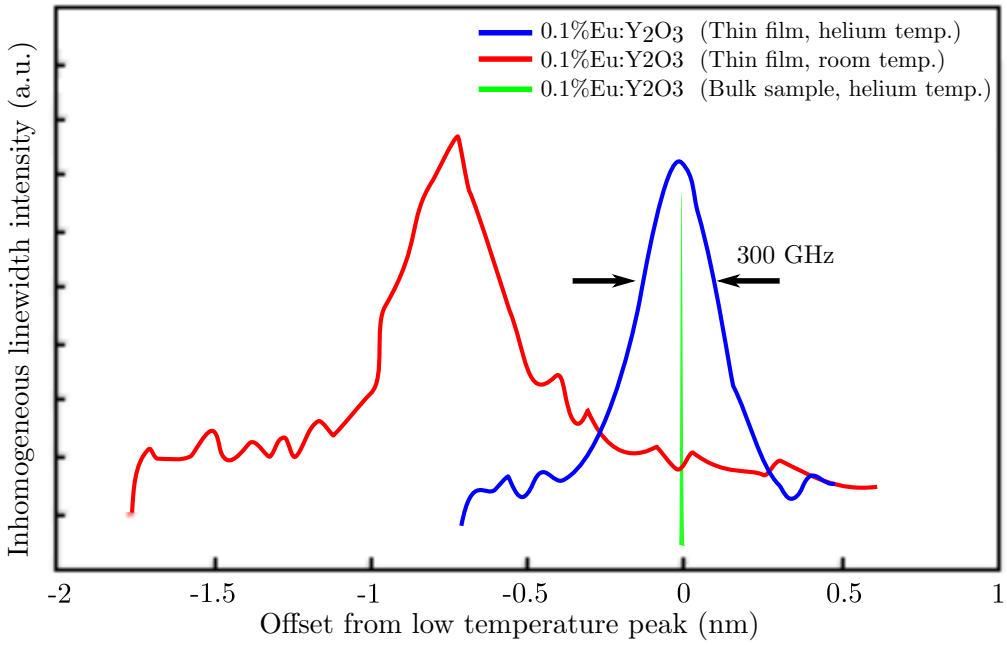

Figure 4.4: $0.1\%Eu^{3+}$:Y_2O_3 inhomogeneous linewidth of fabricated thin film and bulk crystal at room and liquid Helium temperatures(2 K). The inhomogeneous broadening of the produced thin film was at least two orders of magnitude larger than the bulk sample measurement.

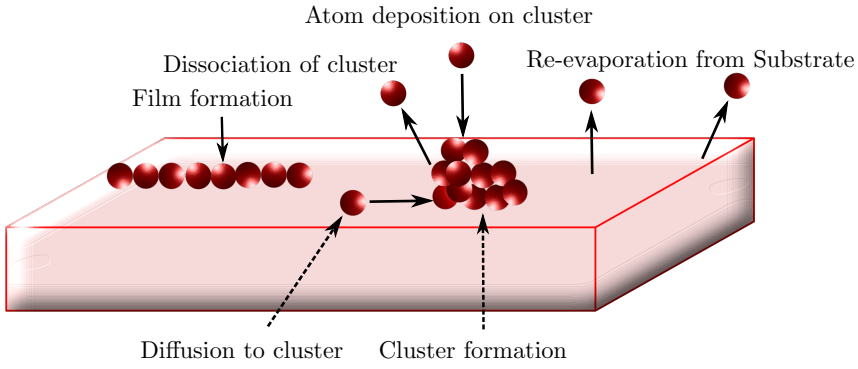

Figure 4.5: Growing thin films of rare-earth ion doped crystals, thin film growth mechanisms. Further explanation can be found in Reference [160].

This is an ongoing project by Paulraj [23], but the results so far have indicated that growing single crystalline thin films is a complicated and difficult task. In order to progress in this project, material issues are being analyzed. Preliminary results of the X-ray diffraction and optical spectroscopy, indicate that these films are not single crystalline. At the moment, Paulraj is investigating different factors that may improve the thin film quality.

One parameter that has been changed during the growth process has been the substrate temperature. As was shown by the results obtained in the group at the University of Hamburg [157], increasing the growth temperature leads to better quality crystal structures, moving from completely amorphous structures to epitaxial thin films. This group hadn't measured the optical emission spectrum of their thin films at liquid helium temperatures, that are required for our experiments. So, from their results it cannot be concluded that by further increasing the growth temperature crystal qualities would improve even further. For our purpose, to build thin films that can be used for integrated quantum devices, we need to obtain single crystalline structures that have similar optical coherence properties to bulk rare-earth crystals. In the thin films grown by Paulraj, changing the growth temperature through a range from 600°C to 1000°C didn't change the quality of the thin films, which may indicate that some other factors have to be taken into consideration.

The atmosphere of the chamber was also investigated. O_2 was inserted into the chamber. One option is to change the pressure of the O_2 and the other option is to add a neutral gas, for example Ar gas. Changing the atmosphere inside the chamber may help with the stoichiometry of the fabricated thin film. This is one of the parameters that Paulraj [23] is considering at the moment.

In an attempt to grow better quality crystals, shielding close to the surface of the target has also been investigated. This is achieved by placing a shield close to the target, preventing all the ablated surface material from depositing on the substrate. The atomic plume can diffuse around the shield and form atomic layers on the substrate. This is another attempt that is being analyzed at the moment by Paulraj.

The growth of single crystalline rare-earth ion doped thin films which preserve the optical and hyperfine coherence properties of these crystals for coherent applications has not been thoroughly researched in the past. This makes this field relatively new and challenging because a lot of parameters have to be investigated to construct such a thin film. Since the objective of this thesis was to implement integrated quantum information devices, another method of waveguide fabrication was proposed and will be discussed from here on.

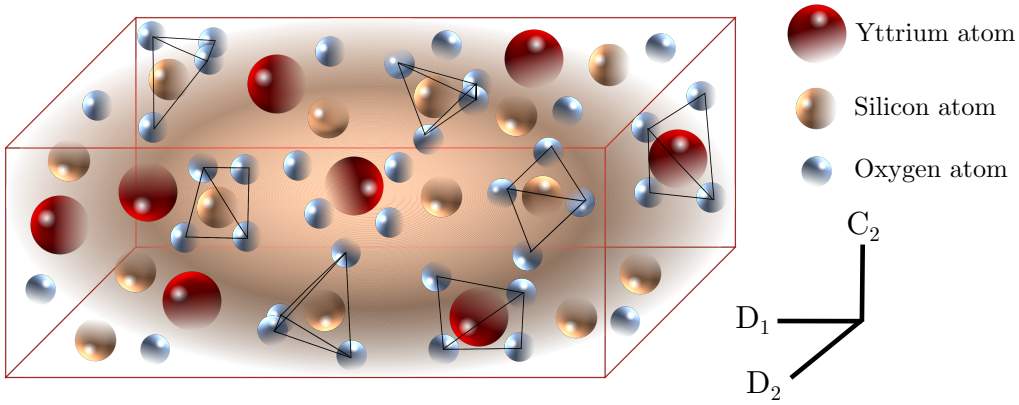

Figure 4.6: The unit cell of the Y_2SiO_5 crystal with the crystalline axes, D_1, D_2 and C_2.

4.3 Thin films with rare-earth doped crystal as active substrate

In this approach high quality bulk rare-earth ion doped crystals were used as the waveguide substrate and then by growing a thin layer of a high refractive index glass on top, a waveguide was fabricated. The bulk crystal used as the substrate was Pr^{3+}:Y_2SiO_5, which is introduced in Section 4.3.1. This is followed by the fabrication method explained in Section 4.3.2.

4.3.1 Pr^{3+}:Y_2SiO_5

The selected rare-earth ion doped crystal in this thesis was Pr^{3+}:Y_2SiO_5. The spectroscopic properties of this crystal have been extensively researched [2, 161], hence it was a good choice for the relatively new design investigated in this project. The yttrium orthosilicate crystal (Y_2SiO_5), shown in Figure 4.6, is a mono-clinic crystal belonging to the C_{2h}^6 space group (No. 15 in the International Table of Crystallography) [162]. This crystalline structure has eight molecules per unit cell, as can be observed in Figure 4.6. The dimensions of the unit cell are a = 14.411, b = 6.726, c = 10.419 and $\beta = 122.22°$ [162].

The yttrium to oxygen bond in the Y_2SiO_5 crystal forms two distinguishable and distorted octahedral yttrium sites known as 'Site 1' and 'Site 2' [162, 163]. In Pr^{3+}:Y_2SiO_5, the triply ionized Pr^{3+} replaces the Y^{3+} ions in the structure. Pr^{3+} ions occupy two non-centrosymmetric crystallographic sites with no rotational symmetry (C_1). Site 1 is the site that is relevant to this work and the transition

	Site 1 of $0.02\%\mathbf{Pr^{3+}}\mathbf{:Y_2SiO_5}$
$\lambda[^3H_4 \rightarrow {}^1D_2]$	605.977 nm
Γ_{inh}	4.4 GHz
T_1	164 ± 5 μs
T_2	152 μs ($\equiv$ 2100 Hz)
Γ_h	1800 Hz
f	3×10^{-7}
α	10 cm^{-1}

Table 4.2: Spectral and relaxation parameters for the $^3H_4 \rightarrow {}^1D_2$ transition site 1 in $0.02\%Pr^{3+}:Y_2SiO_5$ [2].

wavelength of this site in $Pr^{3+}:Y_2SiO_5$ is at 605.977 nm. Maximum absorption in Site 1 of $Pr^{3+}:Y_2SiO_5$ occurs when the polarization of light is aligned with the D2 axis [164, 165]. So, to obtain maximum absorption when moving towards waveguide structures, it would be beneficial if the polarization of the guided light is aligned with this axis.

$Pr^{3+}:Y_2SiO_5$ is a good candidate for the demonstration of an optical data storage device due to its relatively large oscillator strength and long coherence times [48, 166]. Furthermore, $Pr^{3+}:Y_2SiO_5$ has previously been used successfully in the demonstration of many quantum communication applications, such as efficient quantum memories for light [26] and dynamic filtering [28].

The energy level diagram of Pr^{3+} ions in the crystalline structure of Y_2SiO_5 of Site 1 is shown in Figure 4.7. This structure shows the relative impact of the spin-orbit of the free ion, the crystal field and quadrupole Hamiltonian terms [59, 167, 168]. The degeneracy of the *LSJ* states has been lifted by the crystal field, which results in C_1 symmetry in the crystal.

The optical coherence properties and hyperfine structure of the $^3H_4 \rightarrow {}^1D_2$ optical transition of 0.02 $\%Pr^{3+}:Y_2SiO_5$ has been studied extensively by Equall *et al.* [2]. These experiments were conducted at 1.4 K by pumping on liquid helium. The spectral and relaxation properties of the $0.02\%Pr^{3+}:Y_2SiO_5$ crystal used in this

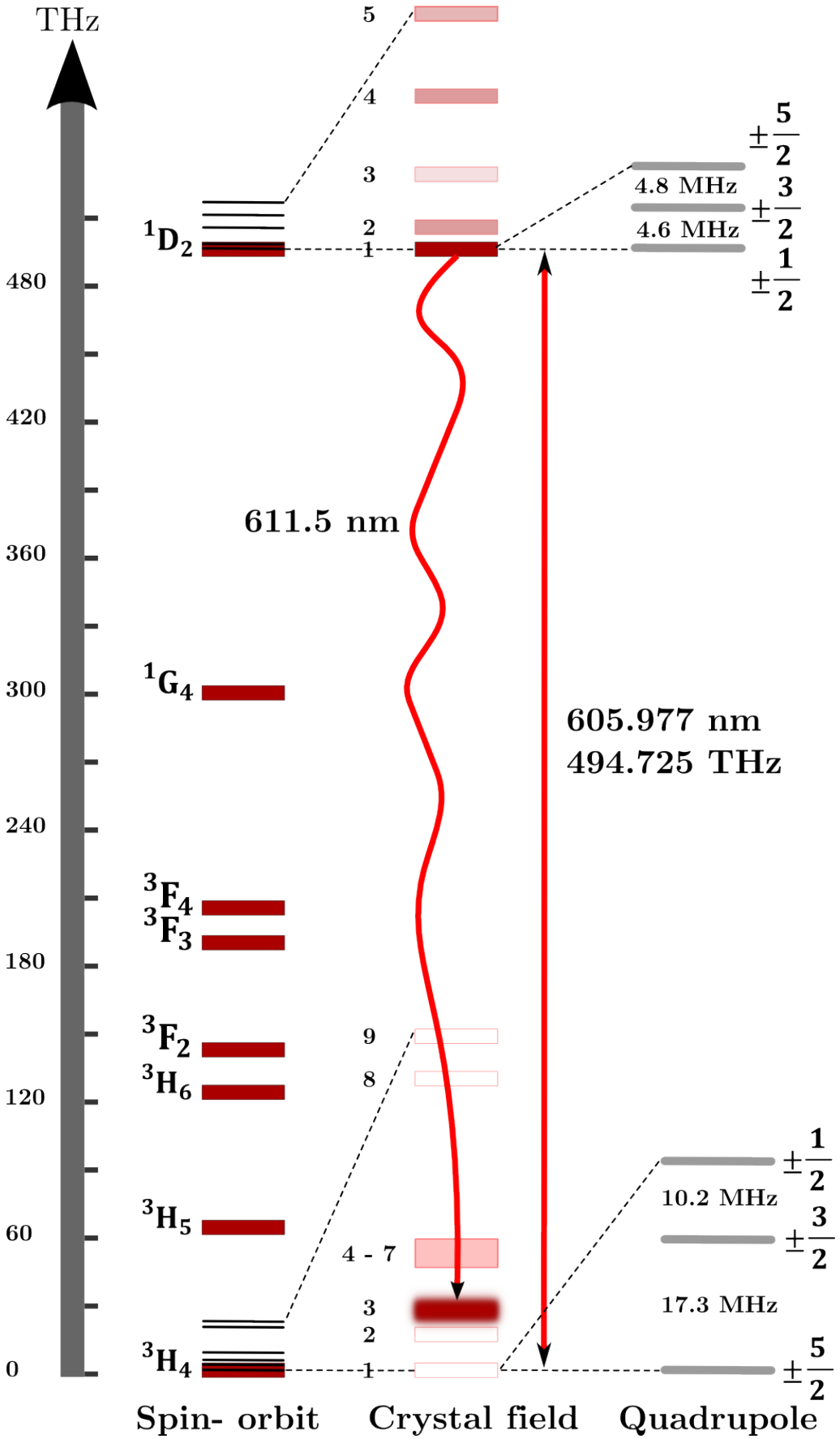

Figure 4.7: Pr^{3+}:Y_2SiO_5 energy structure [59]. This energy level diagram shows the effect of spin-orbit, crystal field and quadrupole Hamiltonians on the energy structure of Pr^{3+}:Y_2SiO_5 [2, 69, 167, 168].

research is shown in table 4.2.

The hyperfine levels in the Pr^{3+}:Y_2SiO_5 crystal have also been extensively researched. In zero magnetic field, the 3 doubly degenerate hyperfine levels have been split on the order of 10 MHz and the spin state lifetimes are approximately 200 s at 1.4 K [69]. This results in a lower bound for the homogeneous linewidth to be close to the millihertz level, but magnetic fluctuations cause excess broadening on the hyperfine level's homogeneous linewidths. Using the ZEFOZ technique, Longdell *et al.* were able to extend the zero field coherence time to 1.4 s from the initial 500 μs [48, 49]. With the application of dynamic decoupling (DDC) pulses and the static magnetic field, the storage times were further extended to 28 s [53].

4.3.2 TeO_2 thin films on Pr^{3+}:Y_2SiO_5 substrates

The rare-earth ion quantum component integration introduced and investigated here relies on the complex photonic circuitry that can be fabricated in low loss TeO_2 ridge waveguides coupled with fast electronic manipulation of ensembles of rare-earth ions in the active substrate. One of the advantages of glass waveguides is that one can obtain very good quality, smooth walls on the ridge. Tellurite glasses have great optical properties which make them suitable for many applications such as optical telecommunications and sensing [24]. These glasses have a big transparency window from about 400 nm to 6 μm in the mid infrared range. They also posses high refractive indices of up to about 2.2 [24], which is desirable for our purpose due to the high refractive index of rare-earth ion doped crystals used as the substrate in the waveguide. Furthermore, these glasses have low material dispersion and so less light and hence less quantum information would be lost during the performed operations.

The slab waveguide was constructed by depositing a 400 ± 10 nm TeO_2 thin film ($n_{eff} = 2.05$) on a Pr^{3+}:Y_2SiO_5 rare earth crystal ($n_{sub} = 1.806$). The thickness of the thin film was selected such that the waveguide only supported the fundamental mode.

Sputtering is one of the most common methods to deposit thin films for the fabrication of integrated devices [169]. Using sputtering, homogeneous thin films with good adhesion properties can be fabricated [169]. In this fabrication method, a voltage between the target holder and the rest of the vacuum chamber creates a plasma in the chamber. After the creation of the plasma, high energy ions are shot at the target material by a sputtering gun. This causes atoms to come off the target

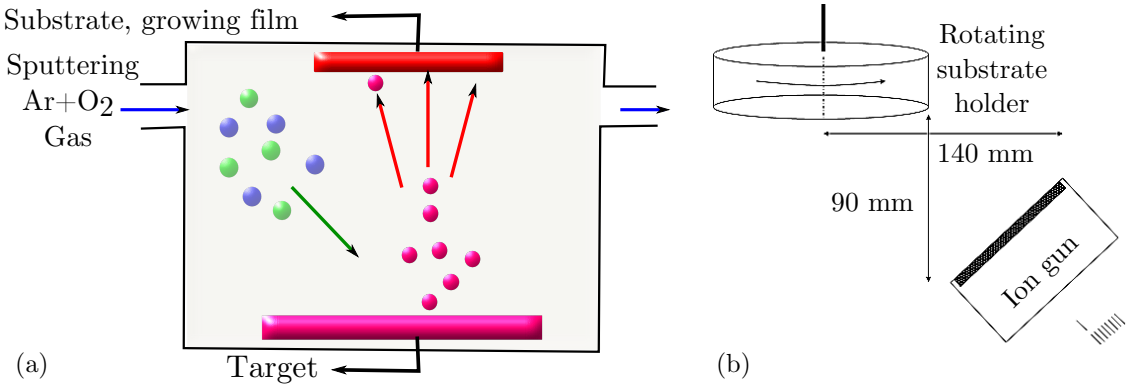

Figure 4.8: Thin film growth using the sputtering method at room temperature. (a) Illustration of reactive sputtering, target atoms come off the surface and deposit on the substrate. (b) The configuration of the RF sputtering gun, and the substrate.

surface and diffuse away from the target. These atoms form a thin film layer by condensing on the substrate.

The fabrication of the thin films in this thesis was achieved using an RF sputtering gun and reactive gases. In RF sputtering, any material, whether conducting or insulating, can be used as the target material. Reactive sputtering was used, which means that a reactive gas is induced into the chamber. In this fabrication method, to ensure that stoichiometric thin films are deposited on the substrate, the reactive gas pressure, the flow rate of gases and the rate of sputtering are important factors. For example, when Oxygen is introduced into the chamber, the sputtering rate reduces a lot. By increasing the RF power or lowering the pressure of the chamber, the reduced rate can be balanced. This thin film fabrication has been thoroughly examined and optimized in Reference [169].

For TeO_2 thin films deposited on Pr^{3+}:Y_2SiO_5 substrates, the reactive gas in the chamber was an Argon and Oxygen mixture. Dr Khu Vu from the Laser Physics Center at the ANU [170] fabricated these thin films and the Pr^{3+}:Y_2SiO_5 substrates were bought from Scientific Materials Corp, Bozeman Montana, USA [171]. The pressure in the chamber was set to 5 mTorr. The Argon flow was set to 6 sccm and the Oxygen was set to 5 sccm. The sputtering gun was an RF gun with a power of 75 W. A simple illustration of the sputtering method is shown in Figure 4.8. These conditions were optimized using the design of experiments (DOE) method using software simulations [169]. High quality and low loss thin films have been previously demonstrated using TeO_2 [24].

TeO_2 is a soft glass and interacts with water, or moisture in the air. Hence, to protect the TeO_2 thin film from environmental hazards, a thin 5 nm layer of SiO_2

was deposited onto the Pr^{3+}:Y_2SiO_5 surface before the TeO_2 deposition. Then a 14 nm layer of SiO_2 was deposited on top of the TeO_2 glass. The optical experiments performed on these thin films will be discussed in Chapter 6. Two coupling methods were used in these experiments which will be further explained in Chapter 5.

4.4 Deposition of electrodes on TeO_2 thin films

One can use Stark shifts, as explained in Section 2.2.1.4, to electronically control rare-earth ions in quantum devices. To achieve the required Stark shifts to manipulate the active Pr^{3+} ions in the substrate of the fabricated TeO_2 thin films, one can envisage depositing the control electrodes onto the thin film surface. For this purpose, gold (Au) electrodes were deposited onto the thin film surface. In this project, a small mask was placed on the thin film and gold was deposited onto the crystal surface as shown in Figure 4.9.

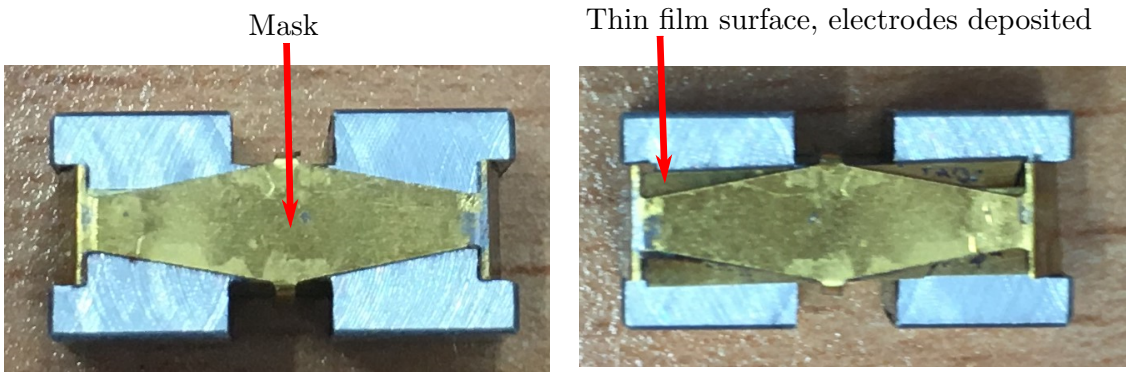

Figure 4.9: The mask was placed on top of the crystal which was sitting on a piece of aluminum block. It was then placed in the E-beam evaporator where gold was deposited onto the crystal edges.

The bonding of Au to other materials is weak [172] and usually a buffer layer of Ti or Cr is used to bond the Au to the underlying material. The Ebeam Evaporator system at the ANFF labs at the ANU [173] was used to deposit the electrodes onto the surface of the TeO_2 thin films. A stainless steel mask was designed to achieve the desired electrode shape. In the first attempt, a 10 nm thick layer of Ti was deposited, after which a 100 nm of Au was deposited. This coating completely came off after cleaning the crystal surface with Acetone.

In the next trial, a 10 nm layer of Cr was deposited before the 100 nm Au layer. This layer also came off after the cleaning process. After this attempt, the thin film surface was first bombarded with Ar gas, which is used to etch a few nm off

the surface and clean the thin film surface. Then a 10 nm layer of Ti, followed by 100 nm of Au was deposited. These electrodes bonded well with the slab waveguide surface.

4.5 Summary

In this chapter, two waveguide design approaches of active and passive waveguides and their material issues were discussed. Growing single crystalline thin films that preserve the optical coherence properties of the $0.1\%Eu^{3+}:Y_2O_3$ crystal proved to be difficult. The broadened 300 GHz inhomogeneous linewidth of the grown thin films that were 2 orders of magnitude larger than bulk samples, was an indication that the grown thin films were either polycrystalline or amorphous. Different factors affecting the growth of these thin films, such as growth temperatures and the chamber environment are being investigated by Paulraj.

The passive waveguide, which is the focus of this thesis, was fabricated using $Pr^{3+}:Y_2SiO_5$ as the substrate and a thin glass layer of TeO_2 as the thin film, with the reactive sputtering method. The sputtering conditions were optimized using the DOE method and software simulations to obtain high quality thin films. Experiments performed using these thin films are explained in Chapter 6.

To electronically control the devices built using this method, electrode deposition was also investigated. gold thin electrodes were deposited using the Ebeam evaporator. The bonding of gold to other surfaces is weak, so a buffer layer of Ti had to be deposited onto the thin film surface before the gold deposition.

In the next chapter, waveguide theory and the principles of such a structure required for a waveguide will be explored. Also, two coupling methods of prism coupling and grating coupling will be explained.

Chapter 5

Waveguide and Electrode Design

5.1 Introduction

In this chapter an analytic model of the slab waveguides used in this project is developed. The model is primarily used to calculate the coupling of the optical mode to the rare-earth doped substrate. The important factors relevant to this thesis are the amount of power penetrating into the active substrate, that probes the Pr^{3+} ions and the efficiency of the coupling method.

Two coupling methods used in this thesis, prism coupling and grating coupling, are introduced. Prism coupling is a relatively easy method to use, as long as a prism with a refractive index that is higher than the thin film is available. Using this method, the coupling point cannot be precisely defined and the prisms take too much space on the surface of the waveguide. So, grating coupling, which would be more versatile when integrating many devices on a single chip, was used in further experiments. The important parameters of a binary grating, the pitch, number of gratings and the efficiency will be presented.

To be able to electronically control the Pr^{3+} active rare-earth ions in the substrate of the waveguide, electrodes had to be deposited onto the thin film surface. The design of electrodes that would produce a linear electric field gradient across the thin film will be introduced. The simulations were performed using the Comsol Multiphysics [174] software, which uses a finite element method to simulate such problems.

5.2 Waveguide theory

A geometrical figure of a typical waveguide structure with light confined in the core is illustrated in Figure 5.1. In any simple waveguide structure, three media are analyzed: the core (film), substrate and superstrate. In a dielectric optical waveguide, confinement of light is achieved when total internal reflection occurs at the interface between the higher refractive index core (film) and lower refractive index substrate.

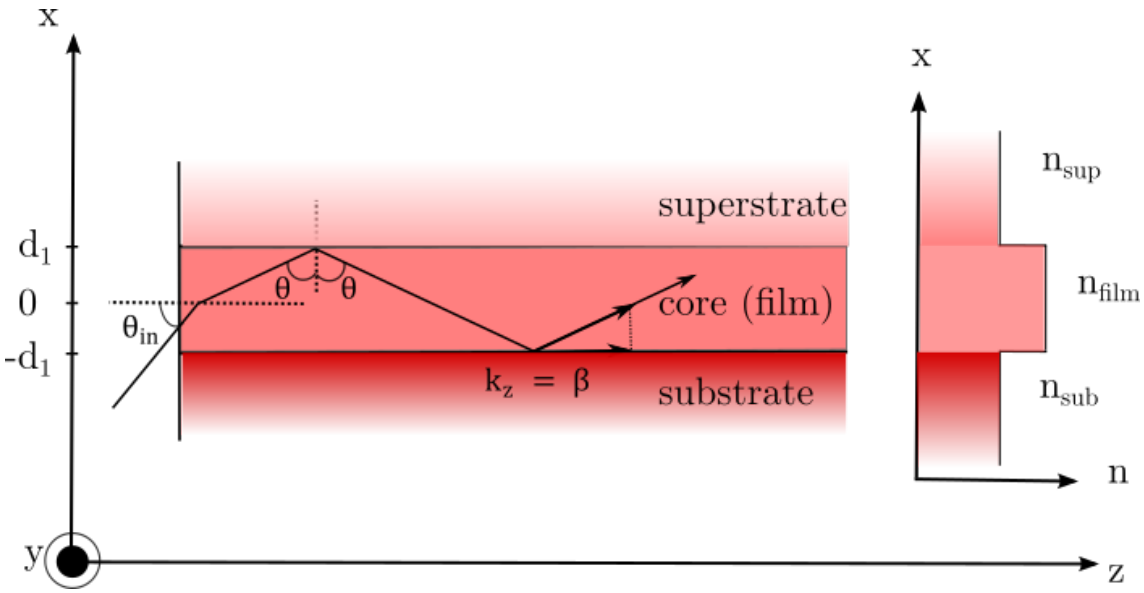

Figure 5.1: Waveguide structure with the three layers of superstrate, core and substrate. For guiding to occur, the refractive index of the core has to be higher than the surrounding layers.

The propagation of light inside the film of a waveguide structure can be expressed by the wave-vector k_z, in a media with an effective refractive index of n_{eff}. In this description, the propagation constant is calculated by Equation 5.1. In this equation (Equation 5.1), $k_0 = |\mathbf{k_0}|$ is the wave-vector of the incident wave on the thin film and z is the direction of propagation [175].

$$\beta = k_z = k_0 n_{eff} \tag{5.1}$$

, where β is the propagation constant.

In this project, since waveguides supporting a single transverse mode are relevant, Maxwell's wave equations to calculate the electric fields of this mode have to be solved. In this approach a discrete number of modes are supported and the

dimension of the thin film is comparable to the wavelength of the utilized light ($2d_1 \approx \lambda$). Maxwell's equations can be written as Equation 5.2, where **E** and **B** represent the electric and magnetic fields, respectively.

$$\begin{aligned} \nabla.\mathbf{B} &= 0 \\ \nabla \times \mathbf{E} + \frac{\partial \mathbf{B}}{\partial t} &= 0 \\ \nabla.\mathbf{D} &= \rho \\ \nabla \times \mathbf{H} - \frac{\partial \mathbf{D}}{\partial t} &= \mathbf{j} \end{aligned} \tag{5.2}$$

In Equation 5.2, **D** represents the electric displacement vector, which can be expressed by $\mathbf{D} = \epsilon\mathbf{E}$ in an isotropic dielectric medium, **H** is the magnetic flux density, ρ is the charge density, which is zero for isotropic media ($\nabla.\mathbf{E} = \rho = 0$), and **j** represents the current density.

Considering the boundary conditions for a planar optical waveguide as shown in Figure 5.1, by solving Equation 5.3, the electric field of a finite plane wave propagating in the z direction can be obtained.

$$\mathbf{E}(\mathbf{r}, t) = \mathbf{E}(x, y) \exp^{i(\omega t - \beta z)} \tag{5.3}$$

In a planar waveguide structure, the y direction can be considered as infinite. This assumption simplifies Equation 5.3 to Equation 5.4.

$$\mathbf{E}(\mathbf{r}, t) = \mathbf{E}_y(x) \exp^{i(\omega t - \beta z)} \tag{5.4}$$

To obtain maximum absorption, the waveguide of this thesis was designed such that it only supported the Transverse Electric (TE) mode which is parallel to the D_2 axis of the rare-earth substrate. Solutions for TE modes can be written as shown in Equation 5.5.

$$E_y(x, y, z, t) = E_y(x) \exp^{i(\omega t - k_z z)} \tag{5.5}$$

Using Equation 5.4 and considering that $E_y(x)$ is continuous across the boundary, the electric field in the planar waveguide can be calculated. To achieve waveguiding in a structure, light waves need to be oscillating in the guiding layer (thin film) and decay exponentially in the substrate and superstrate regions. Hence the solution to the above equation that satisfies these conditions is as shown in Equa-

tion 5.6.

$$E_y(x) = \begin{cases} E_{sup}\exp^{(-\alpha_{sup}x)}\exp^{-ik_z z} \ ; \ x > d_1 \\ \cos(k_x x + \psi)\exp^{-ik_z z} \ ; \ -d_1 \leq x \leq d_1 \\ E_{sub}\exp^{(\alpha_{sub}x)}\exp^{-ik_z z} \ ; \ x < -d_1 \end{cases} \tag{5.6}$$

E_{sub} and E_{sup} are the electric field amplitudes in the substrate and superstrate respectively and are shown in Equation 5.7.

$$\begin{aligned} E_{sup} &= \cos(kd_1 + \psi)\exp^{\alpha_{sup}d_1} \\ E_{sub} &= \cos(-kd_1 + \psi)\exp^{-\alpha_{sub}d_1} \end{aligned} \tag{5.7}$$

ψ is the phase shift that the light wave experiences in the film. α_{sub} and α_{sup} and k_x are the wave numbers in the 3 regions. These wave numbers are calculated using Equations 5.8.

$$\begin{aligned} k_0 &= \tfrac{2\pi}{\lambda} \\ \alpha_{sup} &= k_0\sqrt{n_{eff}^2 - n_{sup}^2} \\ k_x &= k_0\sqrt{n_{film}^2 - n_{eff}^2} \\ \alpha_{sub} &= k_0\sqrt{n_{eff}^2 - n_{sub}^2} \end{aligned} \tag{5.8}$$

From the continuity condition $\frac{\partial E_y}{\partial x} = 0$ on the $x = \pm d$ interface and Equation 5.8, the mode guidance Equation 5.9 can be obtained, where m is the mode number.

$$2k_x d_1 - \arctan\left(\frac{\alpha_{sup}}{k_x}\right) - \arctan\left(\frac{\alpha_{sub}}{k_x}\right) = m\pi \tag{5.9}$$

By solving this equation for the mode m, the effective refractive index n_{eff} and so the propagation constant can be calculated. From Equation 5.9, it can be concluded that for the thin film to support the fundamental TE_{00} mode, a minimum thickness of the thin film layer is required, and for the designed waveguide of TeO_2 on Pr^{3+}:Y_2SiO_5 substrates, this minimum thickness was calculated to be about 300 nm . It was also calculated that to support the second TE mode, the film thickness had to be more than 550 nm. To ensure that coupling into the fabricated thin films was possible, and that the film only supported the first mode, the thin film deposited was slightly

thicker than the minimum calculated value and was 400 ± 10 nm thick.

The Transverse Electric (TE) component of the electric field was calculated for a slab of 400 ± 10 nm TeO_2 thin film ($n_{eff} = 2.05$) on a $0.005\%Pr^{3+}:Y_2SiO_5$ rare earth crystal ($n_{sub} = 1.806$) as shown in Figure 5.2.

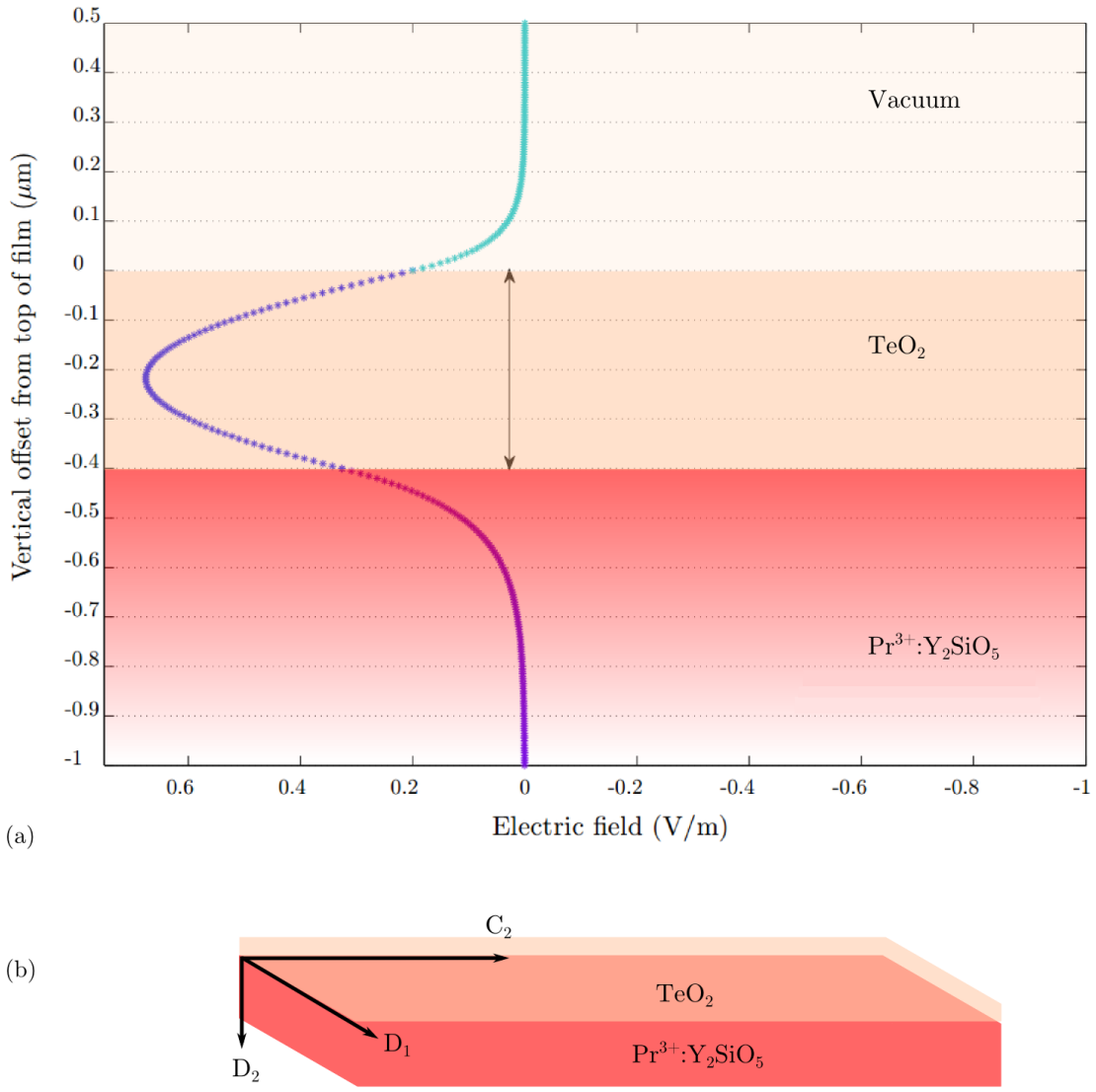

Figure 5.2: (a) The electric field amplitude Ex of the fundamental TE mode supported by the 400 ± 10 nm TeO_2 film waveguide on a $0.005\%Pr^{3+}:Y_2SiO_5$ crystal substrate. (b) Crystalline axes relative to the film deposition.

To simplify Equation 5.6, as the terms in the z direction are the same in all three regions, these terms can be ignored. So the electric field in the three regions

of the waveguide can be written as Equation 5.10.

$$E(x_{sup}) = E_{sup}\exp^{(-\alpha_{sup}x)};\ x > d_1$$
$$E(x_{film}) = \cos(k_x x + \psi);\ -d_1 \leq x \leq d_1 \tag{5.10}$$
$$E(x_{sub}) = E_{sub}\exp^{(\alpha_{sub}x)}\ ;\ x < -d_1$$

Using Equation 5.11 the intensity of light coupled into the three regions in the waveguide structure can be calculated.

$$I_{sup} = \frac{c\times n_{sup}\times\epsilon_0}{\lambda} \times E(x_{sup})^2$$
$$I_{film} = \frac{c\times n_{film}\times\epsilon_0}{\lambda} \times E(x_{film})^2 \tag{5.11}$$
$$I_{sub} = \frac{c\times n_{sub}\times\epsilon_0}{\lambda} \times E(x_{sub})^2$$

By integrating the intensity of light in the structure with respect to x as shown in Equation 5.12, the power coupled to the three parts of the waveguide can be calculated as shown in Figure 5.3.

$$P_{sup} = \int_x I_{sup}dx \Rightarrow S_{sup} = \int_x P_{sup}dx$$
$$P_{film} = \int_x I_{film}dx \Rightarrow S_{film} = \int_x P_{film}dx \tag{5.12}$$
$$P_{sub} = \int_x I_{sub}dx \Rightarrow S_{sub} = \int_x P_{sub}dx$$

To calculate how much light has penetrated into the substrate relative to the light coupled to the film, the area shaded in red in Figure 5.3 was calculated. This is actually the power per unit area, which is the amplitude of the Poynting vector. The percentage of the relative amount of light coupled to the ions in the substrate to the coupled light in the film can be calculated by Equation 5.13. For the 400 nm TeO_2 film on a 0.005%Pr^{3+}:Y_2SiO_5 substrate, 7.2% of the light in the thin film was penetrating into the substrate. In future structures that could still support the TE_{00} mode, by reducing the thickness of the thin film, one can increase the power coupled to the substrate ions .

$$\%S_{\frac{film}{substrate}} = \frac{S_{sub}}{S_{film}} \times 100 \tag{5.13}$$

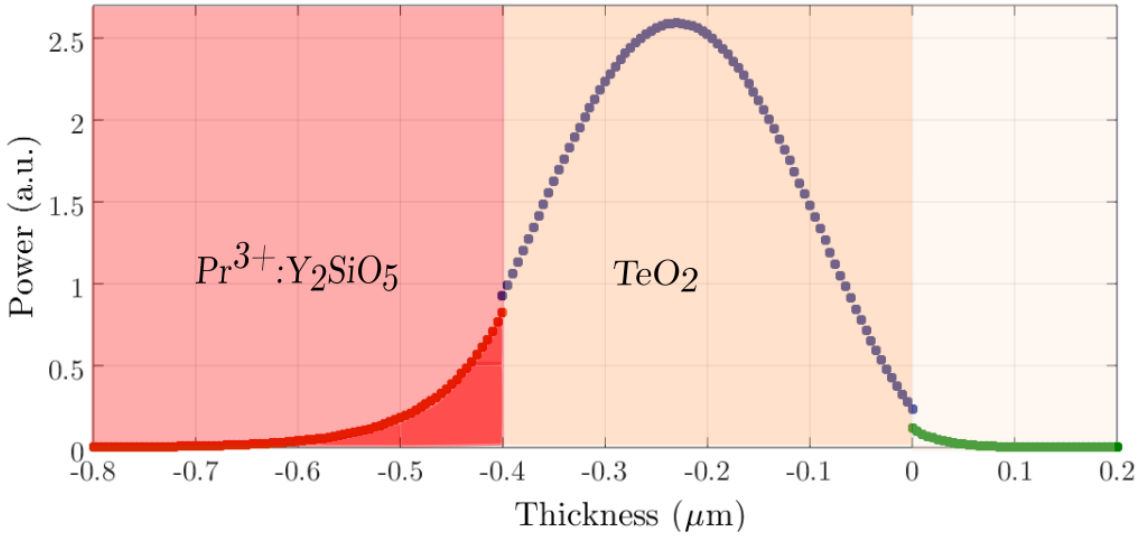

Figure 5.3: TE fundamental mode power in a 400 nm TeO_2 film on a 0.005%Pr^{3+}:Y_2SiO_5 substrate which was produced using a Matlab code. The powers in each section of the waveguide (superstrate, film, substrate) are shown with different colored dots. Red, purple and green dots show the amount of power in the substrate, film and superstrate, respectively. To calculate the amount of light probing the Pr^{3+} ions in the substrate relative to the light coupled to the film, the area shaded in red was calculated.

5.3 Coupling methods

In this Section, two methods for coupling light-waves propagating in free space into the thin films, prism coupling and grating coupling, are investigated. In all the calculations and simulations, the thin films were considered to be slab waveguides. This is a good approximation, since the thickness of the films are similar to the wavelength of the coupled light and therefore the light wave is confined in the thickness and not confined in the transverse direction, which could be assumed infinite to simplify calculations. The diffraction of light along the propagation direction is not an issue in these structures since propagation distance is much larger (on the order of centimeters) compared to the Rayleigh distance (on the order of millimeters), such that the overall divergence is quite low. For example, in the setup where the wavelength of light is 606 nm and the refractive index of the thin film is about 2, and if the spot size is about 20 μm, the Rayleigh distance can be calculated to be 4.15 mm. In this situation, if the waveguide is 10 mm, the beam width at this distance can be calculated to be about 52 μm, which is a bit over double (2.6×) the spot size at the waist of the beam.

Prism coupling was initially selected because of its simplicity and that no fabri-

cation was required for this method. In this method, a higher refractive index prism, compared to the thin film's refractive index, was pressed against the thin film. One of the problems faced using this method was that the coupling spot cannot be well defined. Also, prism coupling is not a method that can be used for more complex integrated quantum systems, because it is not practical to have a lot of large prisms on top of the many devices required on chip.

To enable the construction of devices with multiple input and output couplers, grating coupling was investigated. Gratings were written onto the thin films using Focused Ion Beams (FIB). Grating coupling gave a well defined and controlled coupling spot as opposed to prism coupling, where the coupling spot was not exactly known. The fabrication of these gratings was harder than initially expected. Drifting of the e-beam in the FIB system, which resulted from electrostatic charging on the surface of the thin film, was one of the main issues in writing the gratings.

For coupling to gratings, one still requires macroscopic optical devices to couple light into gratings at particular angles. This will not be practical when moving to complex integrated quantum processors, especially when the quantum device is inside a cryostat. Although grating coupling may not be the best way to couple light into quantum processor chips, it was selected as an interim method of coupling in this project. The investigations into writing gratings will be useful in later research into writing Bragg gratings, for example, as cavities on quantum processor chips. The more suitable method of coupling to quantum processor chips in the long term is fiber butt coupling, but implementing this method was beyond the scope of the project.

5.3.1 Prism coupling

An easily obtainable method of coupling laser beams onto waveguide structures is by using a higher refractive index prism on the thin film. Prism coupling was the first coupling method used to couple light into the thin films of TeO_2 on the Pr^{3+}:Y_2SiO_5 substrates to show that the active substrate method works in principle. The theory of prism-thin film coupler has been extensively researched by Tien *et al.* [176]. In this Section, the theory developed by Tien *et al.* [176] will be presented to calculate the coupling efficiency of light into the TeO_2 thin films.

To excite a mode in the thin film, the prism's refractive index has to be higher than the refractive index of the thin film. For this purpose, a Rutile prism with a refractive index of $n_{vertical} = 2.89$ was held on top of the TeO_2 thin film with

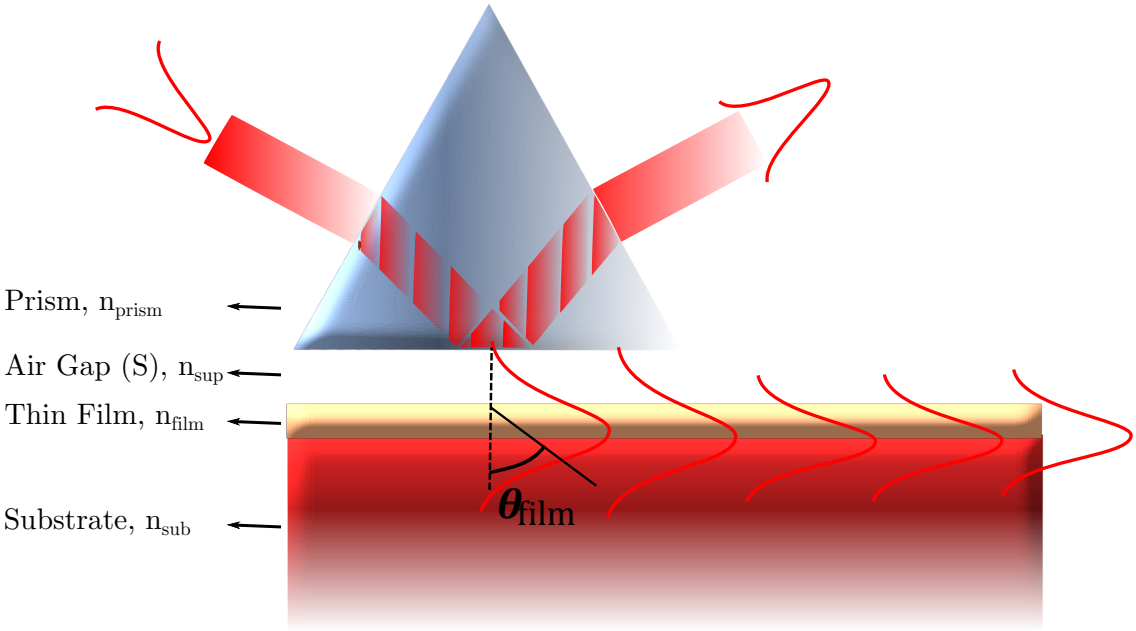

Figure 5.4: Schematic of prism-film coupler. The incident laser beam is totally internally reflected at the base of the prism. The waves in the prism and thin film are coupled through the evanescent wave traveling through the air gap to the thin film. Any of the film modes can be excited by proper orientation of the angle of the incident beam.

a refractive index of $n_{eff} = 2.02$. As simply illustrated in Figure 5.4, the base of the prism is placed on top of the thin film surface. An input laser beam is totally reflected at the base of the prism. The total internal reflection on the prism base causes an exponentially decaying evanescent wave to tunnel below the base of the prism and into the film. If the horizontal component of the wave vector entering the thin film is equal to any of the thin film modes, that mode is excited. Therefore, by choosing the correct angle of incidence for the input laser beam, the required fundamental TE mode can be excited.

To calculate the efficiency of the coupled mode to the TeO_2 thin film, the propagation constant (β) and effective film thickness (h_{eff}) were calculated as shown

in Equation 5.14.

$$\begin{aligned} \beta &= k n_{film} \sin\theta_{film} \\ \delta_{film-sub} &= \frac{\lambda}{(2\pi\sqrt{({n_{film}}^2 \sin {\theta_{film}}^2 - {n_{sub}}^2)})} \\ \delta_{film-sup} &= \frac{\lambda}{(2\pi\sqrt{({n_{film}}^2 \sin {\theta_{film}}^2 - {n_{sup}}^2)})} \\ h_{eff} &= h + \delta_{film-sub} + \delta_{film-sup} \end{aligned} \tag{5.14}$$

Where:

- β is the Propagation constant.
- n_{sub} = Refractive index of substrate ($n_{Pr^{3+}:Y_2SiO_5} = 1.806$).
- n_{film} = Refractive index of thin film ($n_{TeO_2} = 2.02$).
- n_{sup} = Refractive index of air ($n_{sup} = 1$).
- n_{prism} = Refractive index of Rutile prism ($n_{prism} = 2.89$, in the vertical polarization).
- θ_{film} = Angle of the fundamental mode in the thin film (θ_{film}= 68°).
- h = thickness of film (μm) = 0.4 ± 0.01 (μm).
- $\delta_{film-sub}$ and $\delta_{film-sup}$ are the changes to the effective film thickness due to the substrate and superstrate, respectively.
- h_{eff} is the effective thin film thickness.

The efficiency of the coupled fundamental TE mode, considering a varying wide and finite air space ($exp(P_{sup}S) \gg 1$) in the range of 0 to 350 nm between the prism

and thin film surface, was calculated as shown in Equation 5.15.

$$
\begin{aligned}
p_{sup} &= \sqrt{\beta^2 - {kn_{sup}}^2} \\
\phi_{film-sup} &= \arctan \frac{\sqrt{{n_{film}}^2 \sin {\theta_{film}}^2 - {n_{sup}}^2}}{n_{film} \cos \theta_{film}} \\
\phi_{prism-sup} &= \arctan \frac{\sqrt{{n_{prism}}^2 \sin {\theta_{film}}^2 - {n_{sup}}^2}}{n_{prism} \cos \theta_{film}} \\
T &= \sqrt{(4 \times exp^{(-2 \times p_{sup} \times S)} \times sin(2\phi_{film-sup}) \times sin(2\phi_{prism-sup}))} \\
\eta &= \frac{(8 \times h_{eff} \times tan(\theta_{film}))}{(l \times (T^2)))} \times (1 - exp^{-(T^2 \times l)/(4 \times h_{eff} \times tan(\theta_{film}))})^2
\end{aligned}
\tag{5.15}
$$

Where:

- p_{sup} is defined from the wave equation calculated in detail in Reference [176].
- $\phi_{film-sup}$ and $\phi_{prism-sup}$ are defined for convenience in later equations.
- T is the approximation for the absolute value of transmittance between the prism-air gap and air gap-thin film interfaces, for a wide and finite air gap (S) where $exp^{(p_{sup} \times S)} \gg 1$.
- l (μm) is the coupling spot size.
- η is the coupling efficiency of the prism into the thin film.

The relationship between the air space distance (S) and coupling efficiency was calculated as shown in Figure 5.5 using a numerical analysis method. As can be observed in Figure 5.5, if the air space between the prism and TeO_2 is around 0.1 μm, the maximum efficiency of about 80% can be obtained.

Prism coupling is a relatively easy approach and can be used to quickly experiment on a fabricated thin film, but as mentioned before, is not practical to use as a coupling method for coupling to an integrated quantum processor chip. In the next Section, grating coupling will be explained.

5.3.2 Grating coupling

Grating coupling can be used to couple light into different devices on a quantum integrated chip. This coupling method was selected to couple light into the fundamental TE mode of TeO_2 thin films of this thesis. A simple binary grating structure

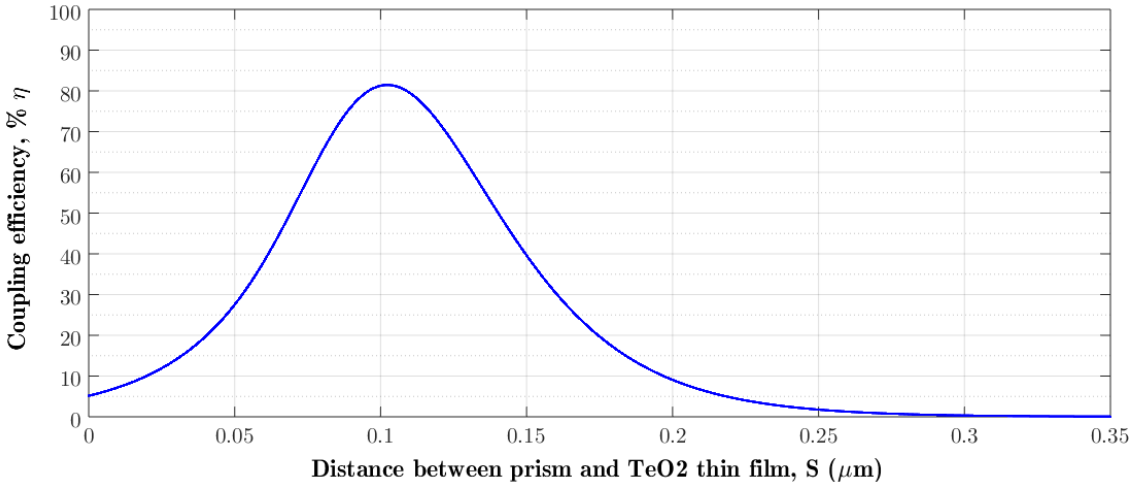

Figure 5.5: Prism coupling efficiency as a function of the distance between the prism face and thin film surface. As can be observed the air gap greatly affects the coupling efficiency. If the distance between the TeO_2 thin film and Rutile prism is close to 100 nm, a maximum coupling efficiency of about 80% can be obtained.

was written onto the thin film surfaces using the Focused Ion Beam (FIB), which will be further explained in Section 6.4. The theory and design of binary gratings was thoroughly researched by Harper [177]. Using Reference [177], the grating angle of incidence and the pitch of the gratings were calculated with respect to the cryostat setup. The other important factor was the grating coupling efficiency that was calculated with respect to grating depths using References [177] and [178].

In binary gratings, the periodic structure consists of thin rectangular ridges. The basic structure of a grating coupler consists of four regions; cover (air), thin film (waveguide), substrate and gratings. A simple schematic is shown in Figure 5.6. Equation 5.16, shows the diffraction equation as was presented in Reference [177].

$$n_{eff} = n_i sin(\theta_i) - q\frac{\lambda}{\Lambda} \tag{5.16}$$

Where:

- $q = 0, \pm1, \pm2, ...$ is the diffracted order number. Due to the cryostat setup of this thesis, the diffracted order $q = -1$ is selected.
- n_{eff} is the effective refractive index of the thin film, which in this part of the project was $n_{eff} = 1.98$. This slight reduction from the refractive index of the TeO_2 ($n_{TeO_2} = 2.02$) is due to the thin layer of SiO_2 which is deposited on top of the thin film as explained in Section 4.3.2.
- θ_i is the angle of incidence on the gratings from the air space above the thin

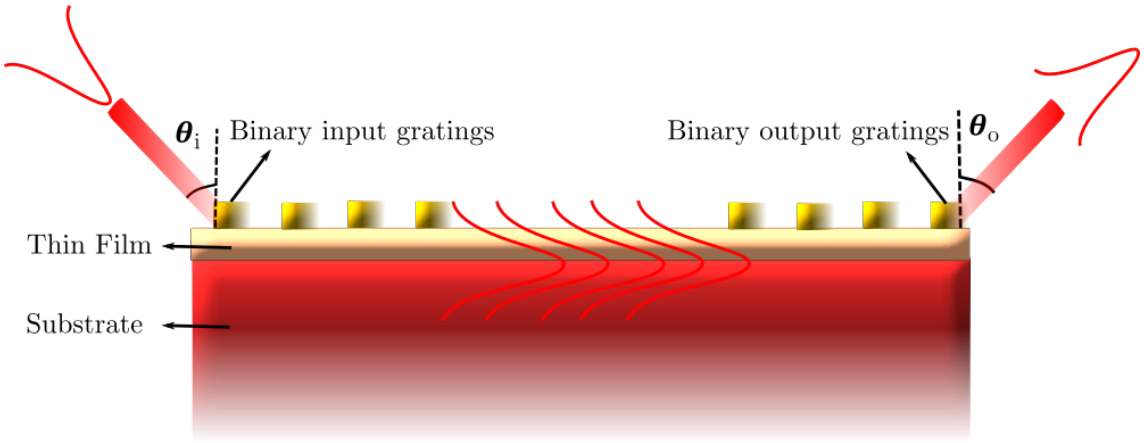

Figure 5.6: Schematic of grating coupling. Input and output gratings can be designed to couple light into and out of the thin film. The incident beam with a particular angle is coupled to the input grating. This light wave is then diffracted into one of the thin film modes. The light then propagates in the thin film mode, and is diffracted out of the waveguide using the output coupler.

film.

- n_i is the refractive index of the incident medium, that was the air space above the thin film.

- λ is the wavelength of the incident light. The wavelength used in this project was 605.977 nm, the excitation wavelength of Pr^3 to probe these ions in the substrate.

- Λ is the grating period or pitch.

From the above equation, a range of pitches can be found for different incident angles. In the writing process, the frame size of the whole grating structure was about 20 μm. This dictated the spot diameter of the beam that can be used to couple to these gratings. The wavelength of the incident light and the refractive index of the thin film and substrate are used to calculate the pitch of the gratings, which was calculated to be 340 nm. With this pitch and the spot diameter of about 20 μm, 55 to 60 lines were written using the FIB setup. Using the calculated pitch of 340 nm and the diffracted order number of q = -1, the incident angle of 11.4° was calculated. The diffracted order number was selected such that a convenient angle was obtained for coupling light into the gratings with the existing cryostat setup. In the cryostat setup used in this thesis, light was coupled to the thin film using a window at the bottom of the cryostat as shown in the next chapter.

5.3.2.1 Eigenmode expansion method

The eigenmode expansion method can be used to calculate grating efficiencies. A complete review of the eigenmode expansion method for solving the wave equations of periodic structures and obtaining electric field components numerically is given in Reference [178]. In this method, the waveguide structure is divided into sections with the same refractive index along the propagation direction. The guided or radiation modes of each section are calculated. The total electric or magnetic field can thus be written as a linear combination of these eigenmodes. By putting all the sections together, a stack is obtained. The scattering matrix of the stack can be calculated by a mode matching technique at the interfaces of the sections. The reflection and transmission of the total stack is attained by the scattering matrix. In this numerical method, by exciting the waveguide with the fundamental mode, the electric and magnetic fields, as well as the radiated power can be calculated at any given position in the stack.

To find the boundary conditions one must consider that the eigenmode method has a size limit in the vertical direction. In this approximation, artificial reflections occur at the boundaries of the sections. This problem is avoided by using an artificial layer called the perfectly matching layer (PML) at the boundary of the different materials. This artificial layer absorbs the reflections and thus doesn't let false reflections into the simulation.

The parameters involved in the simulation need to be selected carefully. Three important parameters are the thickness of the PML, the number of eigenmodes (N) and the distance between the actual structure and the boundaries of the simulation domain (d). A relatively large N is needed in order to obtain close to accurate results for the radiation outputs for the waveguides with grating couplers. However, if N is too large, the simulation becomes very slow. This is also true for the thickness of the PML and the distance d.

The modeling tool used to simulate the grating coupler waveguide structures is a tool called Cavity Modeling Framework (CAMFR) [179]. The simulation result for the TeO_2 on Pr^{3+}:Y_2SiO_5 thin film showed the light field coupled into the waveguide as observed in Figure 5.7.

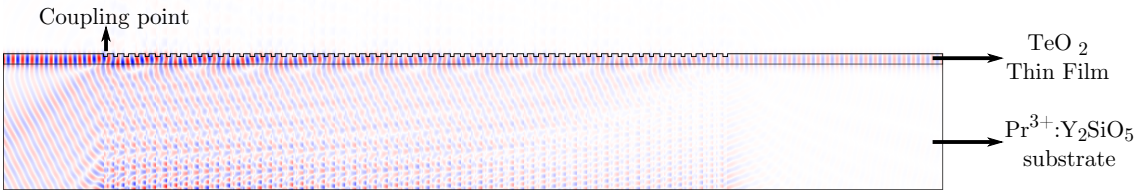

Figure 5.7: Electric field profile of the gratings on the TeO_2 on Pr^{3+}:Y_2SiO_5 waveguide. The red and blue show the positive and negative peaks of the electric field, respectively. The electric field is mostly confined to the TeO_2 thin film, with some leakage going into the Pr^{3+}:Y_2SiO_5 substrate.

5.3.2.2 Gaussian beams

In reality, the light coupled to the thin films are not plane waves but rather Gaussian beams. So the calculations of grating coupling efficiencies have to be amended to take Gaussian beams into account. The beam waist (ω_0) is the original beam size. The amplitude of a Gaussian beam remains Gaussian after propagation through free space. The Gaussian beam is described by the Equation 5.17 [178].

$$\begin{cases} |E(\rho,z)| = \frac{\omega_0}{\omega(z)} \exp\left\{(-\frac{\rho^2}{\omega^2(z)})\right\} \\ \\ \omega(z) = \omega_0\sqrt{1+\frac{2z^2}{k\omega_0^2}} \end{cases} \tag{5.17}$$

The CAMFR modeling tool was used to calculate the grating coupling efficiency into the TeO_2 thin films on Pr^{3+}:Y_2SiO_5 substrates [179]. To calculate the coupling efficiency in the eigenmode expansion method, first the overlap integral between the input electromagnetic field and the grating is calculated. Equation 5.18 is only accurate in uniform media and in weakly guiding structures.

$$\gamma = \frac{\left|\iint E \times H^*_{\text{input}}\right|^2}{Re[\iint E \times H^* \iint E \times H^*_{input}]} \tag{5.18}$$

Nevertheless, it is a good approximation for the case where there is air between the input light and the grating structures. This is due to the fact that the back reflections from the grating to the input source are not taken into consideration in Equation 5.18.

The coupling efficiency from the input source to the waveguide and hence from the waveguide to the detector, was calculated by multiplying the overlap integral by the in-coupled (or out-coupled) power efficiency. After normalizing the input source mode and the waveguide mode, Equation 5.19 was obtained, where S is the facet of

the input light source.

$$\eta = \left| \iint_S E \times H^*_{input} S \right|^2 \tag{5.19}$$

Using the numerical analysis of the CAMFR modeling tool, the coupling efficiencies for different gratings depths on a slab TeO_2 on Pr^{3+}:Y_2SiO_5 thin film was calculated as shown in Figure 5.8. For this simulation, the spot size was selected to be 20 ± 1 μm. With a pitch of 340 nm and grating depth of 170 nm, the maximum efficiency of 63.33% was calculated.

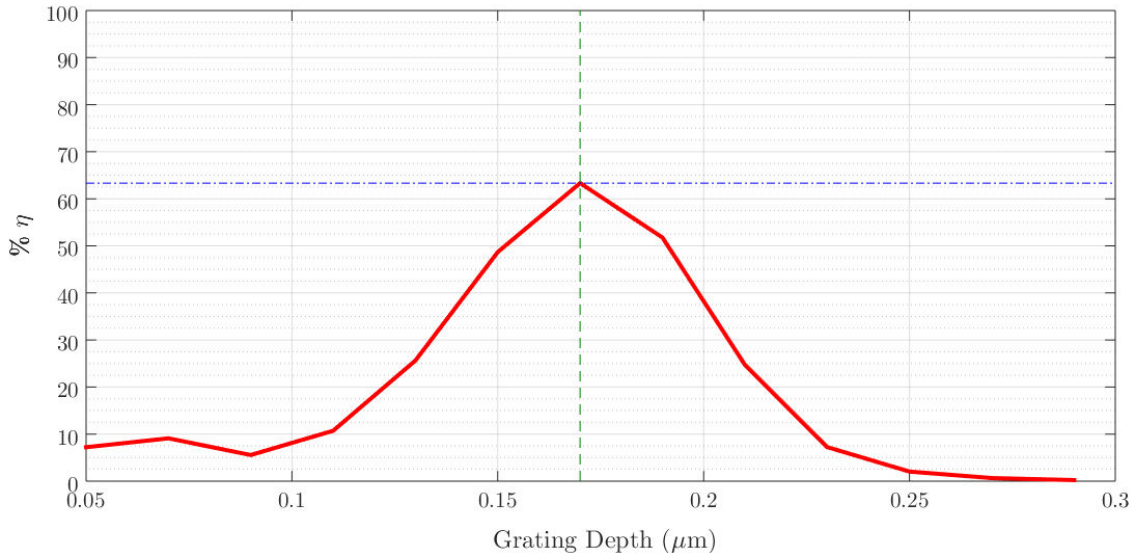

Figure 5.8: Relationship between the coupling grating efficiency and grating depths. 340 nm pitch gratings were written on TeO_2 thin films on Pr^{3+}:Y_2SiO_5 substrates. 170 nm deep gratings resulted in a maximum input coupling efficiency of about 63%. In this simulation, the spot size was selected to be 20 ± 1 μm.

5.4 Design of electrodes on thin films

The Gradient Echo Memory protocol uses Stark shifts, as explained in Section 2.2.1.4, to electronically control the ions in the rare-earth ion doped crystal. In the gradient echo quantum memory built by Hedges *et al.* [1, 26] a bulk crystal and four cm-scale electrodes were used as shown in Figure 5.9. In this GEM, there was a distance between the crystal and the electrodes, so the voltage on the electrodes had to be on the order of tens of volts in order to produce an electric field gradient on the ions to maintain the desired frequency shift. The limit on how big the electric field gradient can be limits the bandwidth of the memory [1].

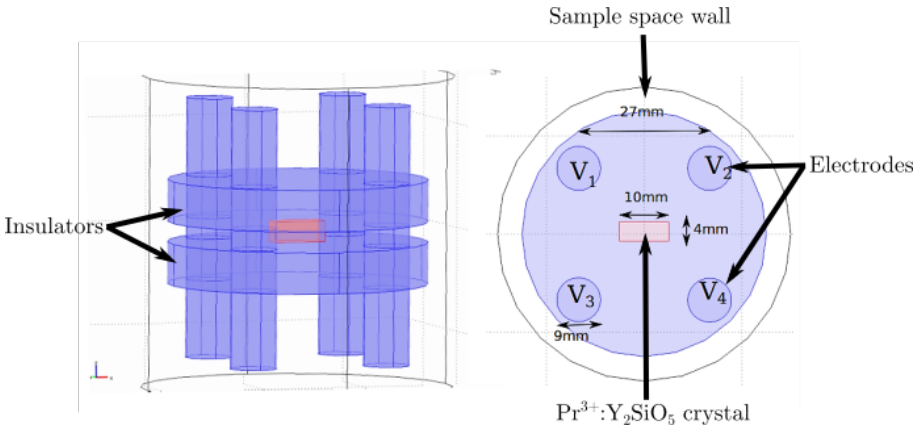

Figure 5.9: Side (left) and top (right) view of a simple quadrupole setup from Reference [1]. Distances between electrodes and dimensions of the setup are shown.

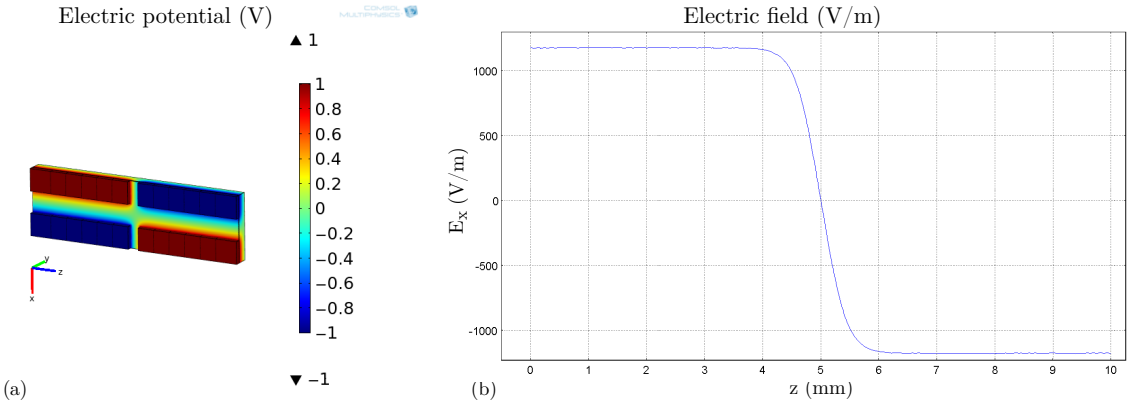

Figure 5.10: Simulation of electrodes designed to obtain a linear electric field (E_x) along the propagation direction (z) [174]. 4 rectangular shaped electrodes with diagonal voltage polarities were simulated. (a) Voltages of 1 and -1 are diagonally applied to the electrodes. (b) The electric field probing the Pr^{3+} ions in the substrate in the middle of the x axis is shown.

By moving towards an integrated structure, large electric field gradients can be placed onto the ions, increasing the bandwidth of the quantum memory. This is achieved by depositing the electrodes on top of the thin film. In order to achieve a linear electric field gradient on the crystal in the propagation direction, some electrode designs were simulated. The electrode shapes and sizes were designed by trial and error, taking into account that a linear electrical field parallel to the D_2 axis of the crystal along the propagation direction was required. The first design was depositing rectangular electrodes onto the top of the thin film as shown in Figure 5.10. As can be seen, the electric field produced by this design was not linear along the propagation direction.

After the first design, the rectangular shape of the electrodes were changed to a triangular (trapezoidal) shape and Figure 5.11 was simulated. It was observed that

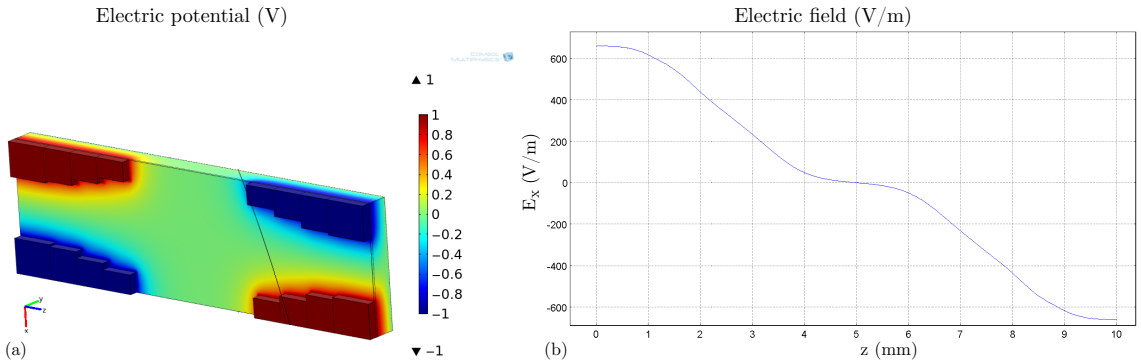

Figure 5.11: Simulation of electrodes designed to obtain a linear electric field (E_x) along the propagation direction (z) [174]. Triangular (or more precisely trapezoidal) electrodes with diagonal voltage polarities were simulated. (a) Voltages of 1 and -1 were diagonally applied to the electrodes. (b) The electric field probing the Pr^{3+} ions in the substrate in the middle of the x axis is shown. It is more linear than rectangular electrodes along the propagation direction.

the electric field produced by this design was closer to a linear field along the propagation direction. In the next series of designs, to obtain a more linear electric field, the shape and size of the trapezoid electrodes were changed. The implementation of this design was performed using a mask as described in Section 4.4. Figure 5.12 shows the TeO_2 on Pr^{3+}:Y_2SiO_5 thin film with gold electrodes. As can be observed, the deposited electrodes were not exactly as designed.

As can be observed from part (a) of Figure 5.12, the maximum applied electric field was 88 V/cm with a voltage of 10 V. The Stark coefficient of Pr^{3+}:Y_2SiO_5 in site 1 is 51.6 ± 0.05 kHz/(V cm $^{-1}$) [4] along the D_2 axis of the crystal. Therefore, it can be calculated that the ions' maximum frequency shift with this voltage is 4.53 ± 0.01 MHz. In the experiment by Hedges *et al.* [26], 20 V was applied to the electrodes, causing a maximum shift of 1.6 MHz. From the simulation results of electrodes deposited on the thin film, by applying voltages of 20 V, a maximum frequency shift of 9.28 ± 0.01 MHz can be achieved. This is an order of magnitude larger than the experiment performed by Hedges *et al.* [26]. In a quantum memory, ideally, one needs to be able to Stark shift ions between different hyperfine levels. The hyperfine splittings of a Pr^{3+}:Y_2SiO_5 crystal are on the order of 10 MHz, hence there is no point in going to larger voltages and bigger Stark shifts for this particular crystal. By changing the voltage polarization on the electrodes, the linear field gradient was reversed as shown in part (b) of Figure 5.12 and the stored light pulse can be recalled. Figure 5.13 shows the fabricated thin film of TeO_2 on the Pr^{3+}:Y_2SiO_5 substrate with the deposited electrodes.

Higher voltages, causing bigger Stark shifts, will be required for rare-earth

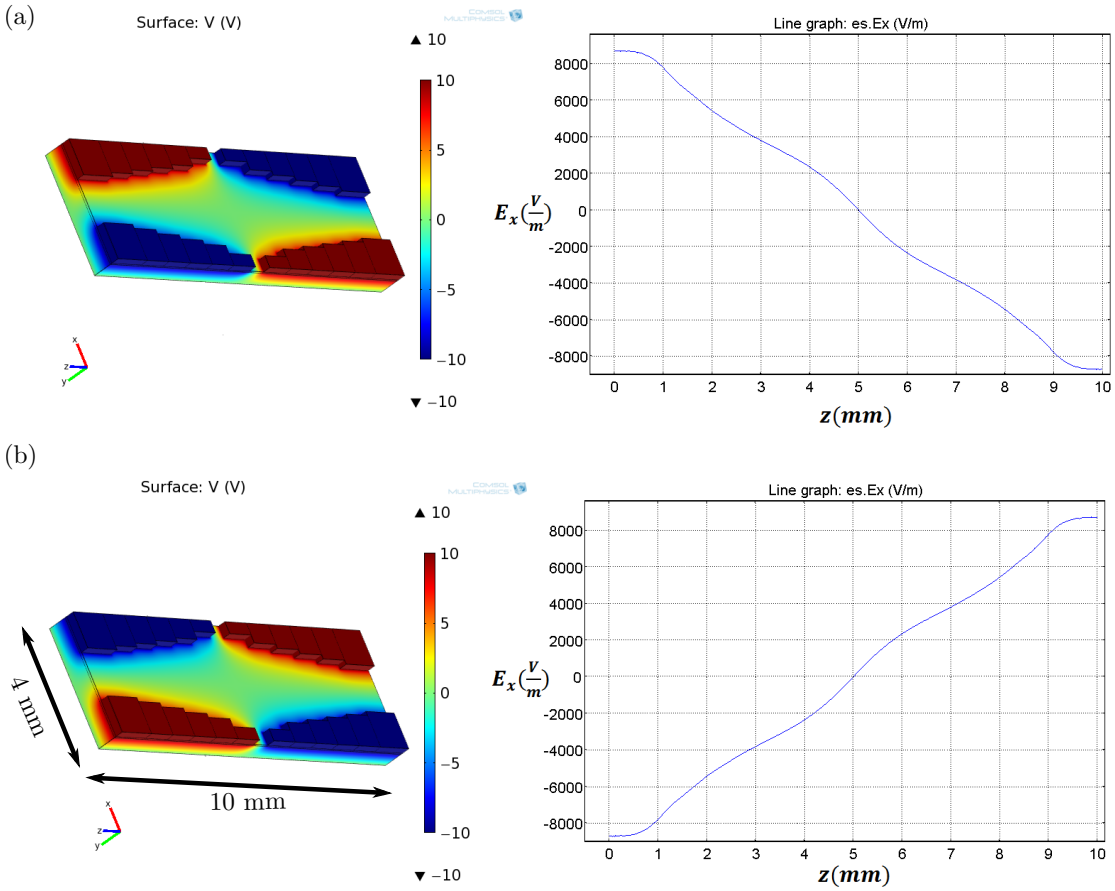

Figure 5.12: Simulation of electrodes designed to obtain a linear electric field (E_x) along the propagation direction (z) [174]. Triangular electrodes with diagonal voltage polarities were simulated. (a) This configuration could be used in the storage phase of the gradient echo memory, 10 and -10 Volts were applied diagonally to the electrodes. (b) By reversing the voltage polarities the electric field is flipped which could be used to recall the stored information.

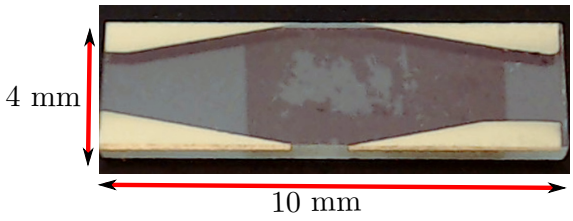

Figure 5.13: TeO_2 on Pr^{3+}:Y_2SiO_5 thin film with deposited gold electrodes.

crystals doped with Eu^{3+} or Er^{3+}, for example. This can be achieved by increasing the voltage and bringing the electrodes closer to the waveguide region. When moving towards integrated quantum processors, two dimensional waveguides will be used rather than the plane waveguides demonstrated here. Using these structure, the electrodes can be placed much closer to the waveguide region and the voltages can be increased, causing bigger Stark shifts.

5.5 Summary

Optical waveguide theory and the principles required for the design of such structures were explored in this chapter. Maxwell's equations for optical waveguides were used to calculate the transverse electric (TE) modes in these waveguides. The solution to these equations lead to the calculation of the electric fields and the optical power in the three regions of the waveguide structure. The TE fundamental mode power in a 400 nm thin film of TeO_2 was then calculated leading to the calculation of the ratio of power penetrating into the Pr^{3+}:Y_2SiO_5 substrate as opposed to the power in the thin film.

Two methods for coupling light-waves propagating in free space into the thin films, prism coupling and grating coupling, were also discussed. Prism coupling is a good proof-of-principle method to couple light into thin films relatively easily. However, it is not a practical method when moving towards integrated quantum optical devices, as the prism coupler takes a lot space on the thin film and also, the coupling point can not be exactly known. Using grating coupling , more compact structures can be built with many coupling points. For the grating coupling method, it was calculated that for the excitation wavelength of 605.977 nm for Pr^{3+}:Y_2SiO_5, and with a spot size of 20 μm, a grating pitch of 340 nm can be calculated. The diffraction mode that was easiest to couple into the thin film was selected. With this diffraction mode and the pitch of 340 nm, the incident angle of 11.4 ° was calculated. Another important parameter in a grating affecting the coupling efficiency is the depth of the gratings. From Figure 5.8, if the grating depth is about 170 nm, an efficiency of about 60% is calculated.

Electrodes can be designed on the surface of the thin film to produce the desired linear Stark shifts along the direction of propagation (C_2 axis of the crystal) on the Pr^{3+} active ions. From the simulation results, the shape of the electrodes deposited on the thin film was trapezoidal. It was also calculated that by applying voltages of 20 V, a maximum frequency shift of 9.28 ± 0.01 MHz can be achieved, which is an order of magnitude more than the bulk crystal experiment performed by Hedges *et al.* [26]. This shift is on the order of the hyperfine splittings for this particular crystal and therefore, larger voltages are not necessary.

In the next chapter, the experiments performed using these waveguide structures and their complexities will be presented.

Chapter 6

Waveguide Characterization and Experiments

6.1 Introduction

Initial experimental demonstrations of key aspects of the proposed architecture for integrated photonic quantum hardware are presented in this chapter. The principle of performing coherent transients using evanescent coupling and probing active ions in the substrate was tested. In this configuration, only a small part of the transverse mode is interacting with the coherent emitters in the substrate. This situation is significantly different to the studied situation in bulk crystals, where the full transverse mode is interacting with the active ions. The success of this architecture also depends on the optical properties of the ions near the interface of the glass thin film and the substrate not being significantly modified. In particular, we are interested in the optical inhomogeneous and homogeneous broadening and the ground state hyperfine lifetimes of the ions in the substrate. The experiments presented in this chapter investigate these two issues using a simple slab waveguide. Furthermore, I also experimentally demonstrate the use of electrodes plated on the surface of the thin film to control the state of the ions using Stark shifting.

To perform the required coherent transient experiments, first prism coupling was used. Placing a prism on a slab waveguide is a simple coupling technique to couple light into the waveguide, but it is not a good solution for future more complicated devices using for example, ridge waveguides. This is due to the imprecision of the coupling point and the added complication of having many prisms when fabricating many devices on the same chip. The second technique used here was grating coupling, where many gratings can be fabricated onto the waveguide, which would allow the implementation of many coupling points on chip. The observed coupling efficiencies are compared with the values predicted in Chapter 5.

The experiments performed with the fabricated thin films with the two coupling techniques of prism and grating coupling are presented in Sections 6.2 and 6.4, respectively. After which, the Stark shifting experiment controlling the active ions in the substrate is presented and analyzed in Section 6.5.

6.2 Prism coupling

6.2.1 Experimental setup

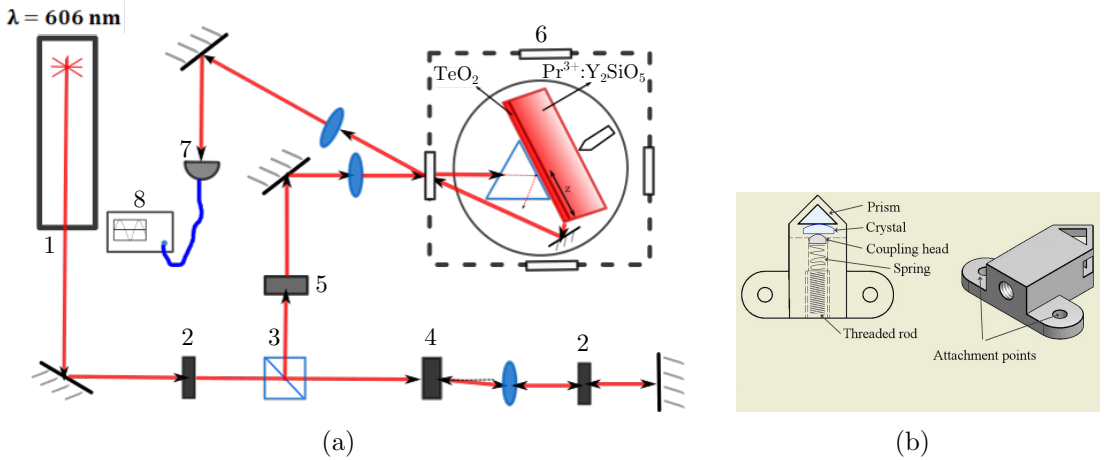

(a) (b)

Figure 6.1: Prism coupling setup, (a) Experimental Setup, Consisting of 1- Laser, 2- Half wave plate (HWP), 3- Polarizing Beam Splitter (PBS), 4- Acousto-optic modulator (AOM), 5- Polarization Rotator, 6- Liquid helium bath cryostat, 7- Detector, 8- Digital oscilloscope. (b) Prism- thin film holder designed for evanescent coupling. Attachment points were connection points to the sample rod [100]. Pictures are not to scale.

To investigate the absorption and spectroscopic properties of the substrate ions, the experimental setup shown in Figure 6.1(a) was used. The TeO_2 thin film on a $0.005\%Pr^{3+}$:Y_2SiO_5 substrate was fabricated using the method explained in Section 4.3.2. A commercial Coherent $699-29$ dye laser was tuned to the ${}^3H_4 \leftrightarrow {}^1D_2$ transition of Site 1 of Pr^{3+} ions at 605.977 nm (494.73 THz). The input laser power on the prism face was 9 ± 0.1 mW. In the first part of the experiment a frequency stabilized laser was not available and so the laser bandwidth was on the order of MHz.

To measure the optical coherence properties of the active Pr^{3+} substrate ions, the excitation beam was gated with a double pass acousto-optic modulator (AOM) to create the pulse sequences for two pulse echo experiments that were described in

Section 2.4.2.2. The modulated light was then coupled to the planar slab waveguide using a Rutile prism ($n_{vertical} = 2.89$) held in contact with the sample using a prism-thin film holder designed for evanescent coupling by Bartholomew [100], as shown in Figure 6.1(b). To obtain a coupling point, the prism was polished on soft cloth, placing a slight curvature (about R = 45 m) on one of the prism surfaces. To couple to the TE_{00} mode in the waveguide, the angle of incidence of the beam on the vacuum-prism interface was calculated to be $18 \pm 0.1°$, which was measured using a goniometer placed on the sample rod outside the cryostat. The coupling was sensitive to adjustment of the angle to about 0.1°. The helium gas flow inside the cryostat moved the sample rod very slightly (on the order of 0.1°), which caused loss of coupling and the loss of the output signal. In order to eliminate this problem, liquid helium was let into the sample space, to dampen the vibrations caused by helium gas on the sample rod. So, the prism-waveguide assembly was immersed in liquid helium, which was pumped below the lambda point, and cooled to 2 K. Also, the rod was mechanically stabilized by attaching a heavy metal piece to the goniometer on the top of the rod, making the structure heavier to minimize any unwanted movement during the experiment.

To allow for the contraction of the components in the cryostat, the pressure head on the back of the substrate in the prism-film holder was spring loaded to have the required flexibility. Using a 10 cm lens outside the cryostat, the waist of the beam was focused at the prism-waveguide interface. By measuring the beam size outside the cryostat and taking into account the distance between the lens and the coupling point, the beam size on the prism-waveguide interface was calculated to be approximately 80 μm. The emitted light out of the end face of the film was directed to the cryostat window and out of the cryostat by a mirror. This light was then detected using a DC to 125 MHz New Focus Si photo-diode detector and the signals were recorded using a digital oscilloscope.

6.2.2 Inhomogeneous profile of $0.005\%Pr^{3+}:Y_2SiO_5$ substrate

The inhomogeneously broadened absorption spectrum was measured by scanning the Coherent $699-29$ dye laser 20 GHz. Figure 6.2 shows the absorption spectrum. The spectrum observed on the digital oscilloscope was sitting on a linear background, which was subtracted to obtain Figure 6.2. The inhomogeneously broadened line of the evanescently coupled ions possessed a linewidth of 2.0 ± 0.1 GHz, which was consistent with the linewidth of bulk samples with the same Pr^{3+} doping concentration, which are about 2 GHz [154].

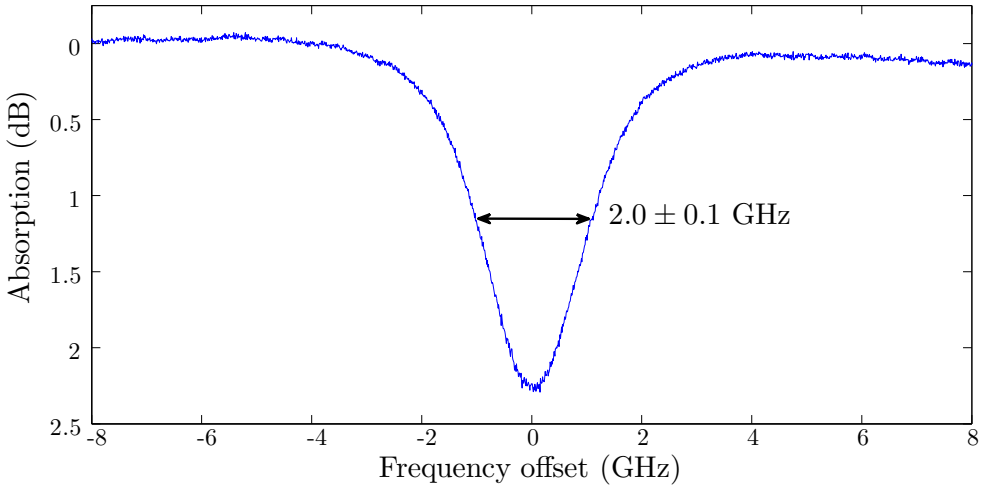

Figure 6.2: The inhomogeneous broadening (absorption spectrum) of a 0.005%Pr^{3+}:Y_2SiO_5 substrate was observed using prism coupling, with FWHM of 2 ± 0.1 GHz. Laser input power on the prism face was 9 ± 0.1 mW. The center frequency was at 494.73 THz.

The model of the propagating TE_{00} mode also allows the absorption of the guided light to be predicted based on the known absorption coefficient of 8 dB/mm [1] for 0.005% Pr^{3+}:Y_2SiO_5, as calculated in Section 5.2. For a film thickness of 400 ± 10 nm, the ratio of the power in the substrate to the total power in the guided mode was calculated to be 7.2%. With an absorption rate of 8 dB/mm [1], an interaction length of 4 ± 1 mm, and 7.2% of light coupled into the 0.005%Pr^{3+}:Y_2SiO_5 substrate, it can be calculated that 2.32 ± 0.8 dB of the input light will be absorbed by the Pr^{3+} ions.

It was observed that about 2.25 dB of the input light was absorbed by the ions. This number was within the error bars of the calculated value of 2.32 ± 0.8 dB.

Figure 6.3, shows the TeO_2/Pr^{3+}:Y_2SiO_5 waveguide. If the praseodymium ions right up to the glass/crystal interface retain the properties of the bulk ions, the absorption coefficient of the TeO_2/Pr^{3+}:Y_2SiO_5 waveguide was predicted to be 0.58 dB/mm which is the bulk absorption of 8 dB/mm scaled by the percentage of power (7.2%) propagating in the substrate. However, the absorption of the waveguide mode will decrease if there exists a depth (x) above which the ions' properties are significantly different to the bulk.

The uncertainty of the interaction length of 4 ± 1 mm is sufficiently large that it is possible that a region at the crystal surface could be present in which ions did not contribute to the observed signal. From our model, the upper bound on the depth

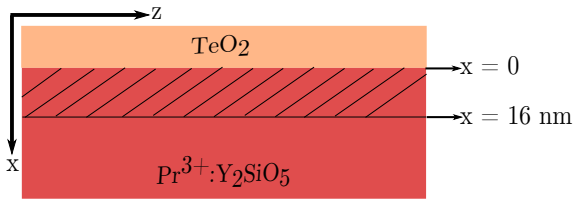

Figure 6.3: $TeO_2/Pr^{3+}:Y_2SiO_5$ waveguide

of such a region was 16 nm. This means that if the first 16 nm of the substrate were disregarded, the measured absorption would still be the within the uncertainty of the calculated absorption. It should also be noted that the uncertainty of the interaction length was sufficiently large that the observed absorption was also consistent with $x = 0$ (at the interface of the glass/substrate). The uncertainty in the interaction length also means that the results would be consistent with the situation where ions within about 10 nm are shifted well outside the 2 GHz wide inhomogeneous linewidth. Though this seems unlikely, as it would have meant that significant excess inhomogeneous broadening had to be observed from the remaining ions below the first 10 nm. This large error bar was due to the prism setup. The point of contact of the prism and thin film could not be accurately measured, which led to this large error bar($\pm$1 mm).

The inhomogeneous linewidth and the amount of absorption, which were consistent with bulk sample measurements, in this part of the experiment show that no excess broadening was observed and that the absorption observed was consistent with the model.

6.2.3 Homogeneous profile of $0.005\%Pr^{3+}:Y_2SiO_5$ substrate

To probe the homogeneous linewidth of the ions in the waveguide mode and measure the coherence time of the substrate ions, two-pulse photon echo experiments were performed. Due to restrictions of laser power in the initial experiments, the excitation pulses were longer than the laser coherence time (3 μs for the $\pi/2$-pulse and 6 μs for the π pulse). A higher-resolution laser was not available at the time. These measurements were later repeated using a frequency stabilized laser on a higher concentration sample. By changing the π pulse length, the Rabi frequency and the intensity of light coupled into the waveguide was measured.

An example of a photon echo is shown in Figure 6.4. The lengths of the $\pi/2$ and π pulses were 3 μs and 6 μs, respectively. The biggest echo intensity was obtained by a t_π of 9 μs. Figure 6.5 shows the averaged maximum intensity of the photon

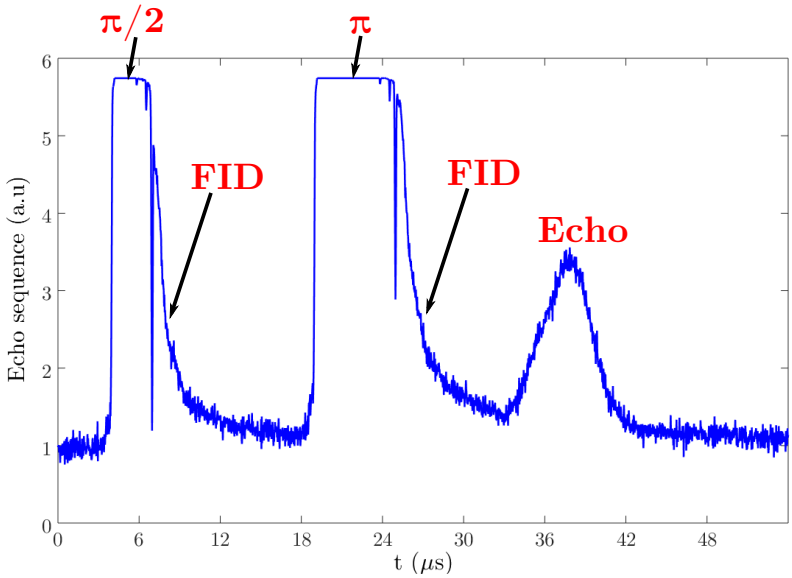

Figure 6.4: Example photon echo sequence using prism coupling, $\pi/2$ and π pulses, their FID and the echo of the input signal.

echo as a function of the delay τ. The optical coherence time T_2 was 70 ± 5 μs, which corresponded to a homogeneous linewidth of 4.5 ± 0.3 kHz. Using the t_π of 9 μs, which gave the biggest echo intensity, the Rabi frequency was calculated to be 349 kHz. Figure 6.6 shows the echo intensities for different π pulse lengths.

The measured homogeneous linewidth was significantly broader than results obtained in zero-field bulk sample measurements in crystals of an equal Pr^{3+} concentration under similar conditions, which were reported to be about 2 kHz [154]. This was most likely due to laser instability, because when similar experiments, on a higher dopant concentration crystal, were repeated later (using grating coupling) with a frequency stabilized laser in Section 6.4.5, the measured T_2 was close to the bulk sample measurements.

It is possible to estimate the intensity of light in the waveguide by determining the π pulse length which maximizes the echo amplitude. This then allows the coupling efficiency into the waveguide to be estimated. The transition dipole moment of $\mu = 1.59 \times 10^{-32}$ Cm, corresponding to an oscillator strength of $f = 3 \times 10^{-7}$ was reported by Reference [2] for this crystal. Considering the above Rabi frequency and the transition dipole moment, the electric field in the substrate was calculated. Using this electric field, the power coupled to the ions in the substrate was calculated to be about 32.5 μW. From the power coupled to the substrate and the ratio of power coupled to the substrate to the film calculated in Section 5.2 (7.2%), the power coupled to the film was calculated to be 491 μW, which was about 4.7% of the total laser power of 9 mW on the prism face.

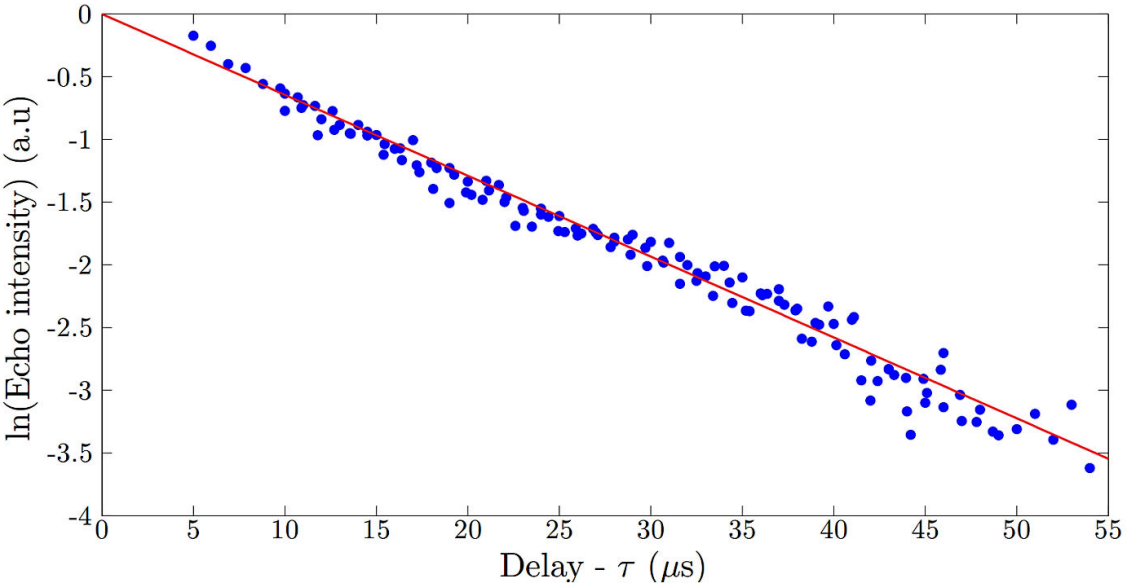

Figure 6.5: Photon echo intensity with increased delay time, the optical coherence time was measured to be 70 ± 5 μs. Laser input power on the prism face was 9 ± 0.1 mW.

6.2.4 Spin state lifetime of $0.005\%Pr^{3+}:Y_2SiO_5$ substrate

To probe the ground state hyperfine lifetime of the substrate ions, a stimulated echo measurement was performed. A series of 1000 $\pi/2$ pulse pairs created a spectral grating, which was then probed with a further $\pi/2$ pulse after a delay T. In this part of the experiment, the Coherent $699-29$ dye laser stabilized to sub-kHz linewidth by locking to a temperature stabilized, ultra-low expansion optical cavity [180] was used. The intensity of the three pulse echo is dependent upon the preservation of the spectral grating over time. The lifetime of the spin states provides an upper bound on the echo decay rate with the delay T.

Figure 6.7 shows the echo intensity as a function of the delay T, which ranged from 0.1 to 1000 s. Holliday *et al.* [69] showed that by using a strong radio-frequency pulse that is resonant with each of the three hyperfine ground states of $Pr^{3+}:Y_2SiO_5$, three population decay rates can be obtained. In their results, the transition resonant with a frequency of 27.5 MHz showed the fastest decay with short lived states. The transitions resonant with 17.3 MHz and 10.2 MHz showed similar and longer population decays. The decay behavior observed here indicated the presence of such short lived states, with a decay rate of 9.8 ± 0.3 s in the first 10 s, and states with significantly longer lifetimes as an echo was still observed at 1000 s. Enough data was not taken to observe the longer decay rates in the current work.

McAuslan [181] has measured the spectral hole lifetime of a $0.005\%Pr^{3+}:Y_2SiO_5$

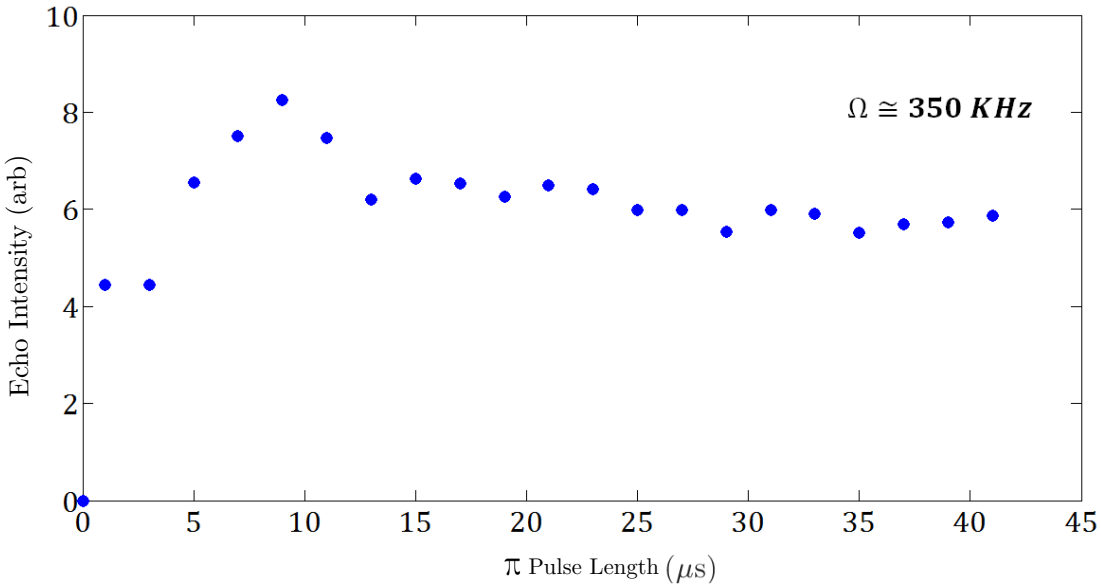

Figure 6.6: The π pulse length was increased and echo intensity was measured. The Rabi frequency was measured from the t_π of 9 μs which gave the biggest echo intensity to be 349 kHz. Laser input power on the prism face was 9 ± 0.1 mW.

WGM resonator, using a similar pulse sequence to what has been used in the current work. He applied 100 pairs of preparation pulses (with a length of 100 ns) followed by a pulse after a wait time 10× larger than the excited state lifetime to ensure that the optical excited state was empty. He has measured two population decays, one with a spin state lifetime of 10 ± 0.7 s and a decay with a longer spin state lifetime of 33.9 ± 9 s. The shorter decay rate spin state lifetime of 10 ± 0.7 s is close to the measured ground state lifetime of 9.8 $\pm$ 0.3 s of this thesis.

The stimulated echo measurements indicated that the close proximity to the interface with the guiding glass medium had not significantly impacted the hyperfine relaxation rate compared to the bulk crystal. The $\pi/2$ pulse pairs were 0.5 μs each and the wait time between the $\pi/2$ pulse pairs was 10 μs. So, the observation of a well-defined echo at T= 1000 s was a strong indication that spectral diffusion was effectively absent in this waveguide architecture over about 100 kHz.

From the above results, it could be observed that the deposition of the glass thin film on the rare-earth ion doped substrate hadn't caused additional strain on the interface of the crystal and the optical coherence properties of the rare-earth ion doped substrate were largely maintained. The promising results of these proof-of-principle experiments led to thinking about other more practical coupling methods such as grating coupling, which will be presented in Section 6.4.

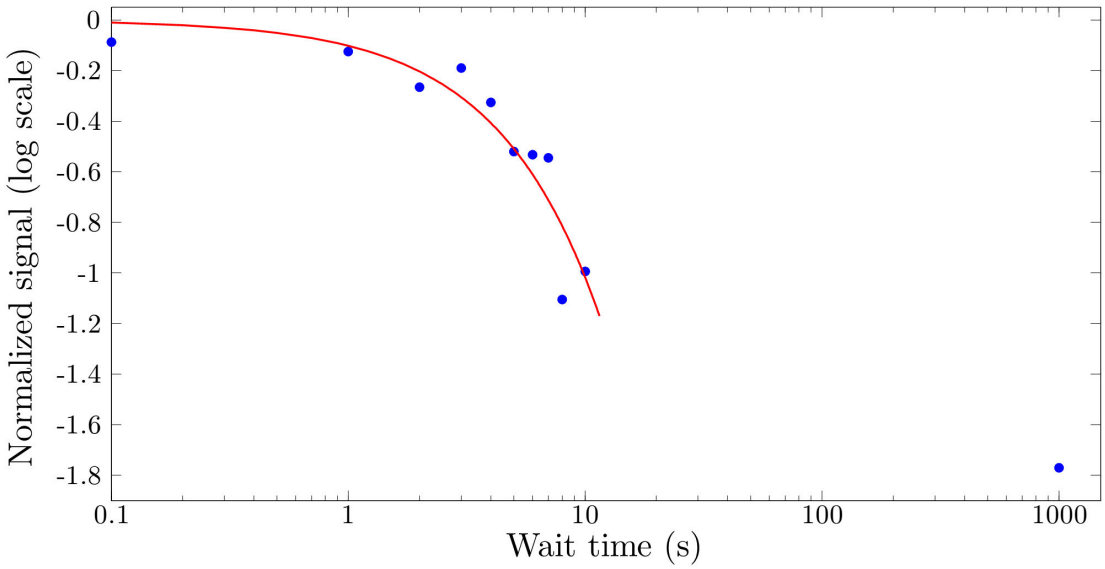

Figure 6.7: Spin echo intensity with increased wait time from 0.1 to 1000 s, a decay time of 9.8 ± 0.3 s was observed in the first 10 s. Laser input power on the prism face was 9 ± 0.05 mW. Data was not taken between 10 s and 1000 s.

6.3 Experimental setup for grating coupling

6.3.1 Cold finger cryostat

The desired coherence properties in rare-earth ion doped crystals require liquid helium temperatures of 4 K and below. To obtain these temperatures, based on the experiment performed, different cryostats are selected. The first set of experiments explained above, were performed using a bath cryostat. The glass thin film used in these experiments was TeO_2 which can be damaged very easily. For example, cycling liquid helium into the sample space in the bath cryostat could possibly damage the surface of the thin film.

To keep these thin films in a clean and contamination free environment, a cold finger cryostat was designed by modifying an existing bath cryostat. This is a much better environment for the thin film, as liquid helium is not let into the sample space and it is only cooled by thermal contact with the cold finger. The two major issues that had to be resolved for utilization of this cryostat were that good quality thermal coupling between the cold finger and the crystal had to be obtained, and radiation heating due to the fact that the crystal was close to the cryostat window had to be minimized.

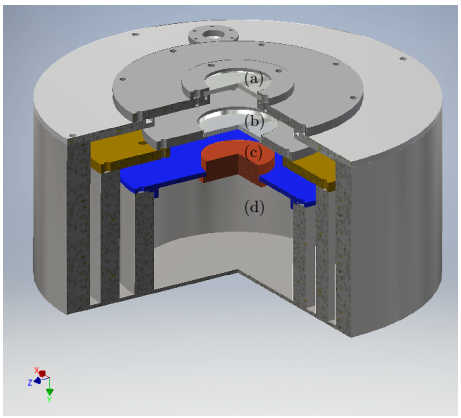

Figure 6.8: Cold finger cryostat, (a) Outer window holding the vacuum in the cryostat , (b) Heat shield window, (c) Copper block where the sample was attached, (d) Liquid helium space. Schematic by Mr John Bottega.

A cross section from the bottom of the cryostat is shown in Figure 6.8. This cryostat consisted of an outer vacuum container, a liquid nitrogen container and an inner liquid helium bucket. A copper cylinder was half immersed in liquid helium and half of it was in the sample space.

6.3.2 Thin film holder

The waveguide was held onto a copper block as shown in Figure 6.9. This copper block was attached to the copper cylinder, which was half in the liquid helium space and half in the sample space. As copper is a good thermal conductor and there was no significant heat load, the temperature of the copper block will be the same as liquid helium that it is in thermal contact with.

To reduce the temperature of the sample, thermal coupling from all the components inside the sample space had to be minimized. As the copper block was thermally connected to liquid helium, all the components had to be thermally connected to this block. To ensure thermal contact between the sample and the copper block, about 100 nm of Au was deposited on the back of the crystal with the same process as mentioned in Section 4.4.

To observe Stark shifting on the ions, electrical contact to the crystal was required. Thin copper wire was connected to the breadboard holding the crystal in place. The electrodes on the thin film surface were in contact with this breadboard as shown in Figure 6.10. The wires attached to the electrodes were another heat load. To reduce this heat load, the wires were spiraled and spun around the copper block to increase contact points and reduce the temperature of the wires as shown

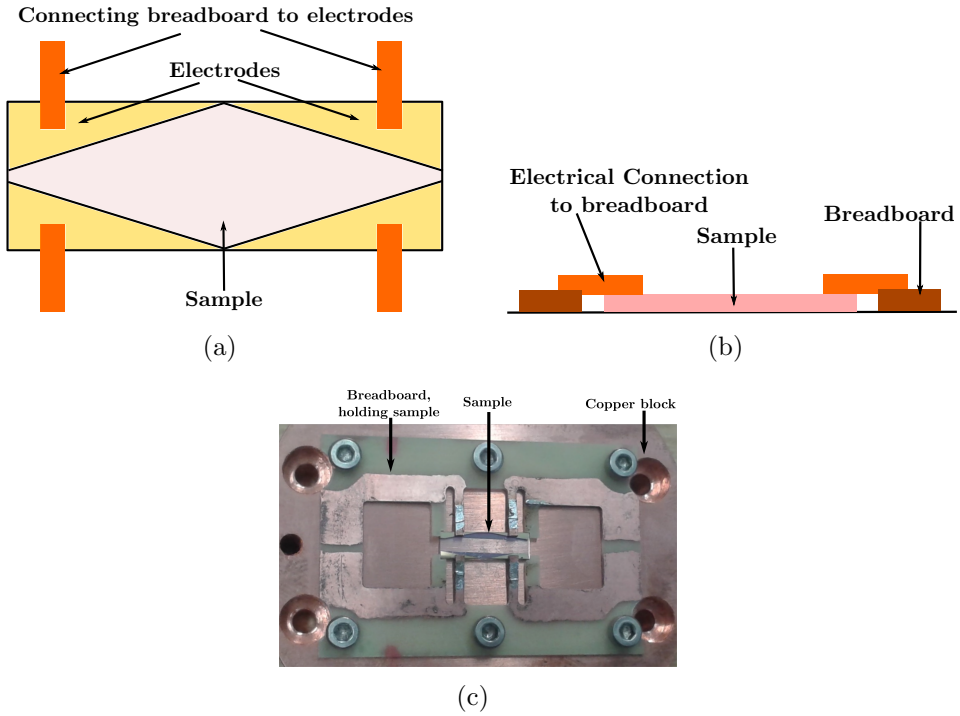

Figure 6.9: Copper block crystal holder. Thin film was placed onto the copper block and held in place by a breadboard on top. The copper block was then attached to a copper cylinder which was half in the liquid helium space, and so the temperature of the cylinder was close to 4 K. (a) Schematic of the front view of the crystal and connections to the breadboard. (b) Sideview of crystal being held in place by the breadboard. As shown in the picture, the breadboard was not thermally connected to the copper block (c) Picture of the thin film holder sitting on the copper block.

in Figure 6.11. The wires were then connected to an electrical feed-through with a head outside the cryostat.

The copper layer on the breadboard was electrically and thermally coupled to the crystal. It was not coupled directly to the cold finger. Further, it was directly exposed to the radiation from the window. The back side of this board was not thermally connected to the copper block and so it could cause the sample temperature to increase. A heat shielding plate, as shown in Figure 6.12, was used to thermally connect the back of the fiber glass breadboard to the copper block while maintaining electrical isolation between the electrodes on the breadboard. The experiment conducted with this cryostat setup will be explained in Section 6.4.

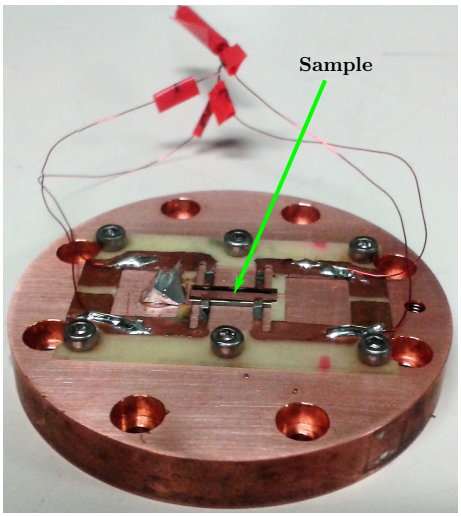

Figure 6.10: Breadboard was electrically attached to the electrodes deposited on the thin film and connected to voltage outside the cryostat by copper wire.

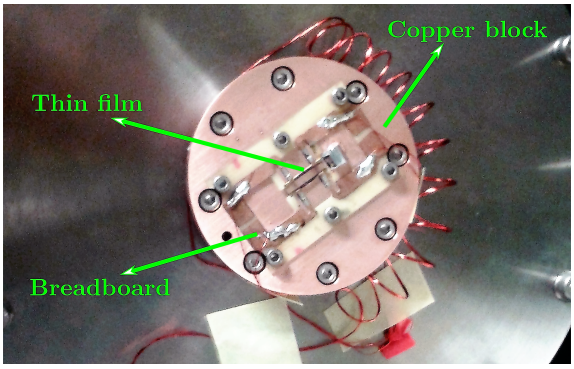

Figure 6.11: Copper wire was wound around the copper block to increase thermal coupling between the wire and the block.

6.4 Grating coupling

6.4.1 Writing binary gratings on TeO_2 thin film surface

The Helios NanoLab^{TM}600i, advanced DualBeam^{TM} for ultra-high resolution imaging, analysis and fabrication at the nano-scale [182], was utilized to write periodic binary gratings onto the TeO_2 thin film surface. This instrument consisted of two tubes, one supplied the Ion beam and the other the Electron beam, as simply illustrated in Figure 6.13.

The first step was aligning these two beams. The two beams are at an angle of 52°. In order to mill into the sample with the Ion beam, the sample had to be parallel with the Ion beam tube. To achieve this, the stage height was set to the

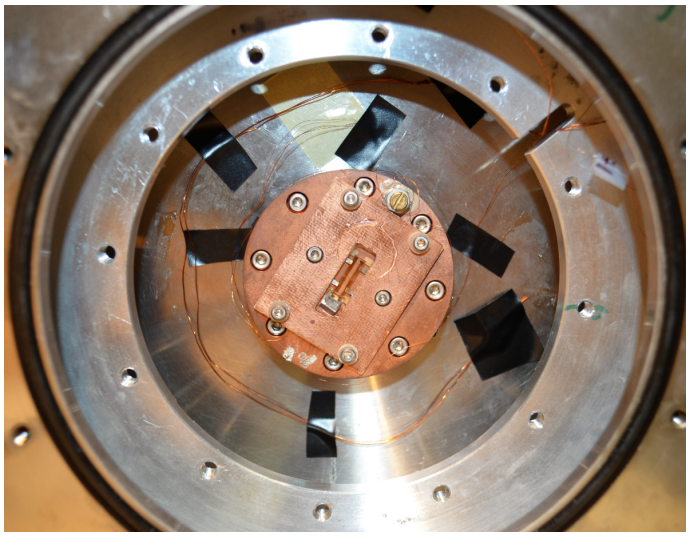

(a)

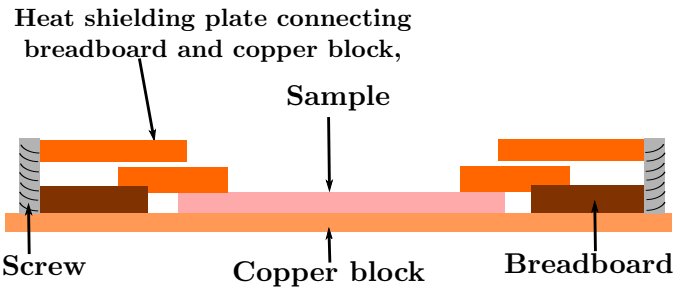

(b)

Figure 6.12: Thin film setup inside cryostat. Breadboard is thermally attached to the copper block using a heat shielding board. A cover slip glass is placed on the gratings to protect the gratings. (a) Picture of the setup inside the cryostat. (b) Side view schematic of heat shield plate attaching the breadboard to the copper block by the screw that was used to attach the breadboard onto the copper block.

"eucentric height", meaning the sample image didn't move when the sample was tilted. This height was 4 mm in this particular setup. The stage was first moved to this height and then the angle was set such that the Ion beam and the sample were parallel. Essentially the sample was aligned such that it was centered relative to both beams. Then the focused ion beam was used to mill lines onto the surface of the sample.

To observe an image with the electron beam, the surface of the sample must be a conductive material. Otherwise, when the surface of the material is bombarded with electrons, electrostatic charging occurs on the surface and the electron beam cannot focus and cannot be aligned with the Ion beam. SiO_2, which was deposited on top of the TeO_2 thin film to protect it, is a non-conductive material, which resulted in electrostatic charging during the grating writing process. The drift of

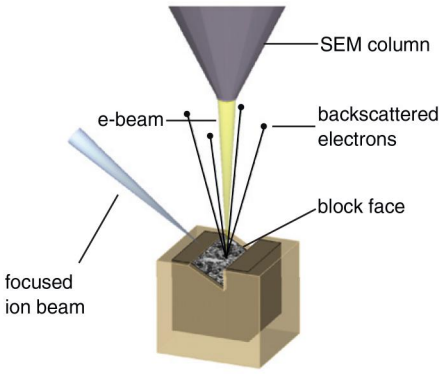

Figure 6.13: A simple demonstration of a focused ion beam setup. The ion and electron columns and their relative angle are shown [183]. In this picture, the electron beam is perpendicular to the surface of the block and the ion beam is at an angle. In my setup, the ion beam was parallel to the surface of the thin film.

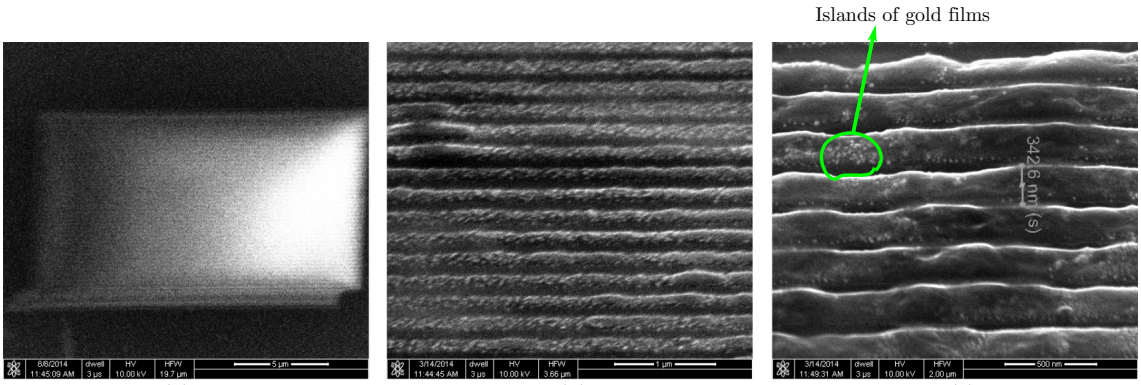

(a) (b) (c)

Figure 6.14: SEM image of misaligned gratings on TeO_2 on Pr^{3+}:Y_2SiO_5 thin films. (a) A lot of electrostatic charging was observed and the ion beam had moved during the writing process, (b) Patches of gold can be seen and hence straight lines were not written, (c) A closer look showed that the pitch of the gratings were not the same.

the electron beam can be observed in Figure 6.14. This drift made it impossible to align the electron beam with the ion beam, and so periodic gratings with the same period could not be written.

To eliminate the charging effect, a thin layer of a conductive material had to be deposited on top of the thin film. The first conductive material that was selected was a thin 5 nm gold film. As can be spotted in part (b) of Figure 6.14, the gold film formed islands on the surface of the SiO_2 film rather than a continuous layer. The thin film surface remained largely non-conductive, and as can be seen in part (a) of Figure 6.14, the milled grating lines were still misaligned. Another problem with depositing gold on the surface was that it could not be removed easily, hence the surface of the thin film was masked so that gold would not be deposited on the

entire surface.

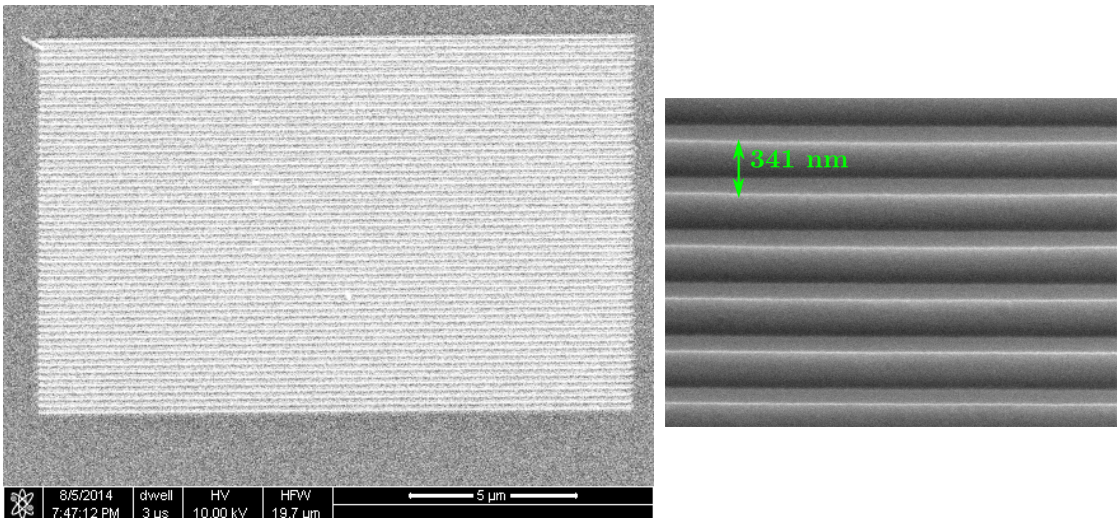

(a) (b)

Figure 6.15: SEM image of gratings on TeO_2 on Pr^{3+}:Y_2SiO_5 thin films, (a) Straight lines with the correct pitch were written, no drift was observed. (b) Closer look at the gratings, the pitch looked the same throughout the grating structure.

Due to these problems, another material was used to obtain a conductive surface. A coating layer of about 10 ± 5 nm of carbon was deposited on the surface of the SiO_2 thin film. Carbon was a much better choice as the thin layer was deposited on the entire surface and after the gratings were written, the carbon layer was easily etched off in an oxygen plasma. Figure 6.15 shows a scanning electron microscope (SEM) image of a written grating.

6.4.2 Performance of gratings

In order to test the gratings and their functionality, a prototype set of gratings were written on TeO_2 on α-Al_2O_3 ($n_{eff} = 1.76$). The refractive index of α-Al_2O_3 is close to Pr^{3+}:Y_2SiO_5, and so the simulation results were similar. To obtain the most efficient grating possible, 8 different grating depths starting from 110 nm with steps of 10 nm up to 180 nm, were written onto the thin film surface.

Figure 6.16 shows one of the TeO_2 on α-Al_2O_3 thin films. The light coupled to the thin film and the scattering beam propagating along the thin film can be observed in this picture. The efficiency could not be calculated using the light collected from the thin film edge, because the edges of these films were not optically polished, and so the output light was scattered. The transmitted light through

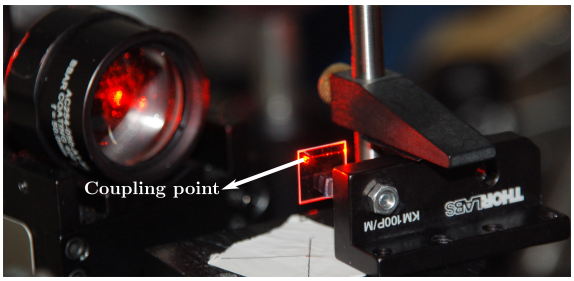

Figure 6.16: Prototype grating coupling, TeO_2 on α-Al_2O_3. Input light was coupled to the binary gratings on the thin film and propagated along the thin film. The coupling point and the scattering beam propagating along the thin film can be observed.

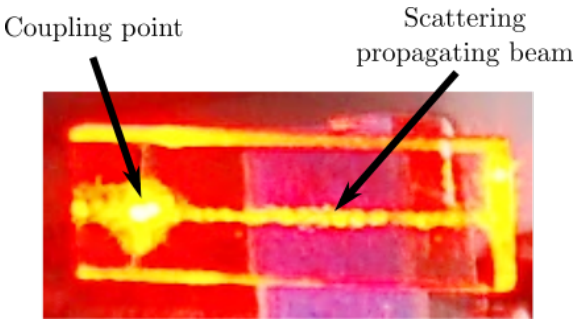

Figure 6.17: Grating coupling, TeO_2 on Pr^{3+}:Y_2SiO_5. Input light was coupled to the binary gratings on the thin film and propagated along the thin film. The coupling point to the 170 nm deep grating and the scattering beam propagating along the thin film are shown.

the thin film was measured and from this number, as mentioned in Section 5.3.2.1, the coupling efficiency could be calculated. The trend of the grating efficiency was similar to efficiency calculations performed in Chapter 5, with the grating with the depth of about 180 nm being the most efficient grating. But the expected efficiency was about 70%, where as the calculated efficiency was much less at about 1%. The possible reasons for such low efficiency are explained in Section 7.1.

After obtaining reasonable results on the prototype thin films on Sapphire substrates, gratings were written on the TeO_2 on Pr^{3+}:Y_2SiO_5 thin film. Figure 6.17 shows light coupled to this thin film and the scattering beam propagating along the thin film. The efficiency of coupled light to these thin films followed the increasing trend of the curve in Figure 5.8, but were reduced by an order of magnitude for each grating as shown in Figure 6.18. Also, as can be observed from Figure 6.18, the model predicted a sharper increase in the efficiency as the grating depth was increased, which was not observed in the efficiency measurements. The 170 nm grating was calculated to be the most efficient in the TeO_2 on Pr^{3+}:Y_2SiO_5 thin films, with an efficiency of 63%. But the measured efficiency of this depth was only $2 \pm 0.1\%$.

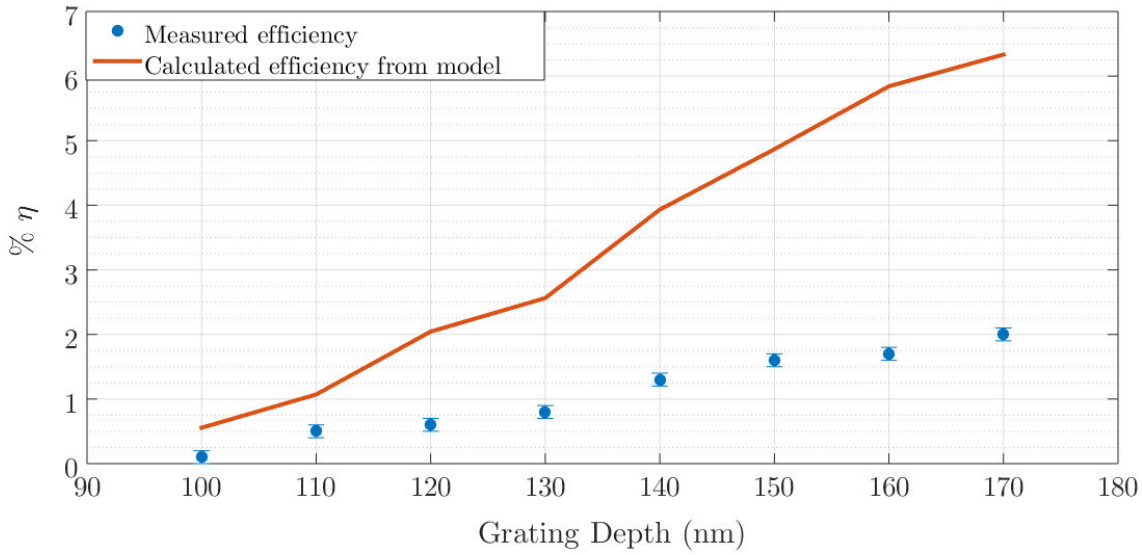

Figure 6.18: Measured efficiency of the 8 gratings with depths of 100 nm to 170 nm, with 10 nm steps, written on the TeO_2 on $0.05\%Pr^{3+}$:Y_2SiO_5 thin film. The linearly increasing trend of Figure 5.8 can be seen as shown by the red line, but the measured efficiencies were an order of magnitude smaller than expected. The calculated efficiency was scaled down 10× for visibility. Input laser power on the gratings was 2.4 ± 0.1 mW. This measurement was done at room temperature, outside the cryostat.

The efficiency did not change significantly between room temperature measurements and cold measurements. Some possible reasons for these low coupling efficiencies are presented in Section 7.1 of Chapter 7.

6.4.3 Experimental setup

After the gratings were written and the carbon layer was etched off, the experimental setup illustrated in Figure 6.19 was constructed. The dye laser used in these experiments was a Coherent 699-29, that was frequency stabilized by locking to an external Ultra-Low Expansion (ULE) cavity via the Pound-Drever-Hall technique [180]. Using this laser locking mechanism, sub-kilohertz linewidths on a millisecond timescale are produced. In addition, the spectral line drifts over longer timescales at a rate of 100 kHz per hour.

The laser was tuned to the ${}^3H_4 \leftrightarrow {}^1D_2$ transition of Site 1 of Pr^{3+} ions at 605.977 nm (494.73 THz). The substrate in this part of the experiment was a $0.05\%Pr^{3+}$:Y_2SiO_5 crystal, with the dimensions of $3 \times 10 \times 0.5$ mm. As before, the excitation beam was gated with a double pass acousto-optic modulator (AOM) to create the pulse sequences for two pulse echo experiments.

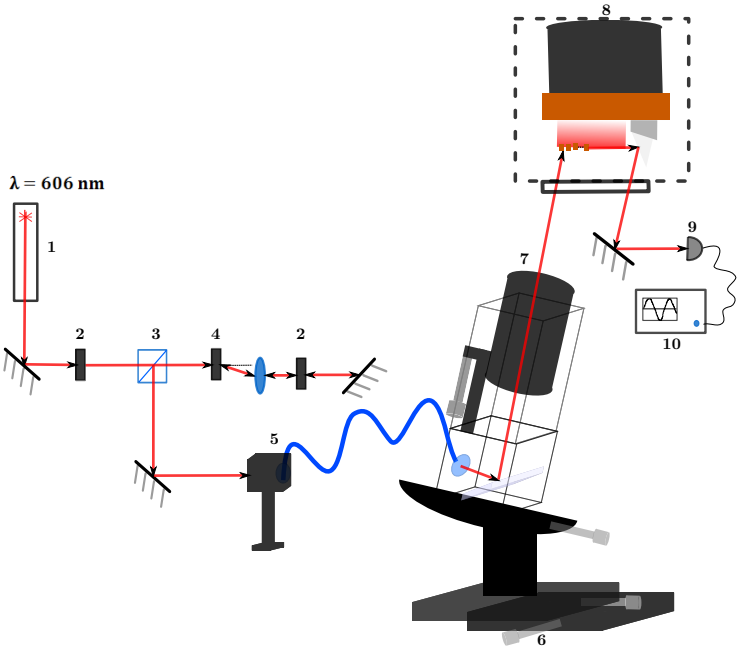

Figure 6.19: Grating coupling experimental setup, Consisting of 1- Laser, 2- HWP, 3- Polarizing Beam Splitter (PBS), 4- AOM, 5- Fiber coupler, 6- Goniometer setup, 7- 5 cm lens, 8- Cryostat, 9- Detector, 10- Digital oscilloscope.

The modulated light was then coupled to the planar slab waveguide using the periodic binary gratings written on the film. In order to couple to the TE_{00} mode, vertically polarized input light was required. The angle of incidence of the input beam on the gratings was calculated to be $11\pm0.5°$, that was tuned with a goniometer setup outside the cryostat. The emitted light out of the end of the crystal was guided outside the cryostat using a right angle prism shaped mirror. This output light was collected from an edge of the crystal which had not been optically polished, therefore there was a lot of scattering and the coupling efficiency could not be easily calculated. The emitted light out of the end face of the film was directed to the cryostat window and out of the cryostat by a mirror. This light was then detected using a Thorn EMI PhotoMultiplier Tube (PMT) and the signals were recorded using a digital oscilloscope. Also, these experiments were performed with a small magnetic field in the z direction, which was used to null the earth's magnetic field in this direction. The magnetic field was made by wrapping a piece of wire around the bottom of the cryostat where the sample was sitting.

6.4.4 Inhomogeneous profile of $0.05\%Pr^{3+}:Y_2SiO_5$ substrate

Acquiring the absorption spectrum was achieved in two stages. First, the laser's center frequency was set to 494.73252 THz (605.968772 nm) and scanned 20 GHz.

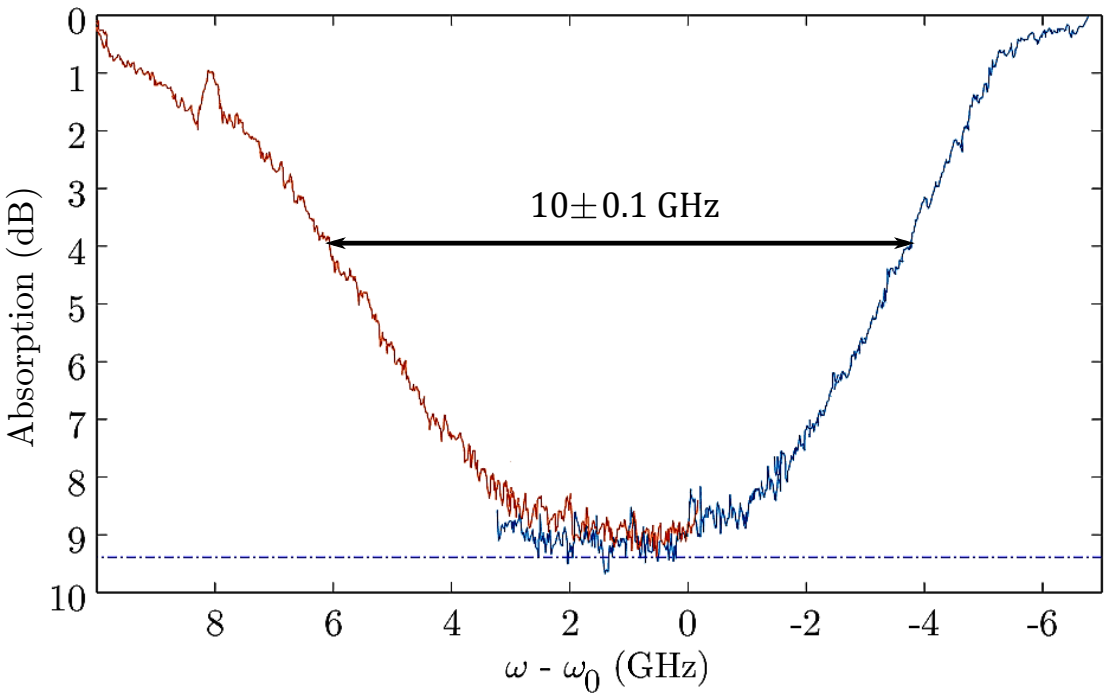

Figure 6.20: The inhomogeneous broadening (absorption spectrum) of a $0.05\%Pr^{3+}:Y_2SiO_5$ substrate was observed using grating coupling, with FWHM of 10 ± 0.1 GHz. Laser input power on the grating was 2 ± 0.05 mW. Note that the small anomalies on the figure are not real, and are due to the filter used to draw this plot in Matlab.

The resultant spectrum was recorded. After which, the laser's center frequency was changed to 494.71371 THz (605.99181 nm) and again scanned 20 GHz and the obtained spectrum was recorded. The absorption spectrum was the result of putting these two traces together. In this experiment, the interaction lengths from the coupling point to the end face of the crystal was about $7.0 \pm 2.5 \times 10^{-3}$ mm. This interaction length has a smaller error bar than the previous interaction length in the prism coupling experiment, because the location of the gratings were measured quite accurately with the scanning electron microscope setup.

The measured absorption spectrum is shown in Figure 6.20. The inhomogeneous broadening of the evanescent coupled ions had a linewidth of 10 ± 0.1 GHz, which was consistent with the linewidth of bulk samples with the same Pr^{3+} doping concentration (about 10 GHz) [1].

Considering the interaction length of about $7.0 \pm 2.5 \times 10^{-3}$ mm and the absorption of 140 dB/cm [1] for a $0.05\%Pr^{3+}:Y_2SiO_5$ crystal, it can be calculated that the absorption over this length of a bulk crystal is 98 dB. From the spectrum shown in Figure 6.20, it can be observed that about 9.38 dB of the input light was absorbed by the near surface ions. From this it can be calculated that the upper bound on

the depth that the ions are contributing to the signal was about 3 nm, which means that if the first 3 nm of the substrate were disregarded, the observed absorption would still be within the uncertainty of the calculated absorption.

6.4.5 Homogeneous profile of $0.05\%Pr^{3+}:Y_2SiO_5$ substrate

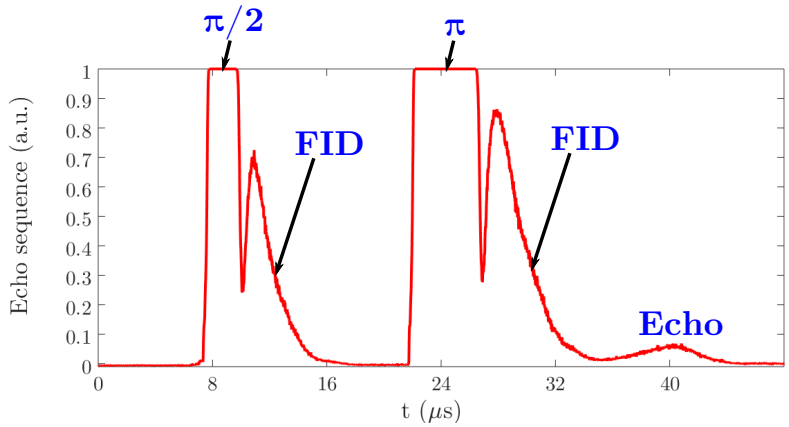

Figure 6.21: Example photon echo sequence using grating coupling, $\pi/2$ and π pulses, their FID and the echo of the input signal.

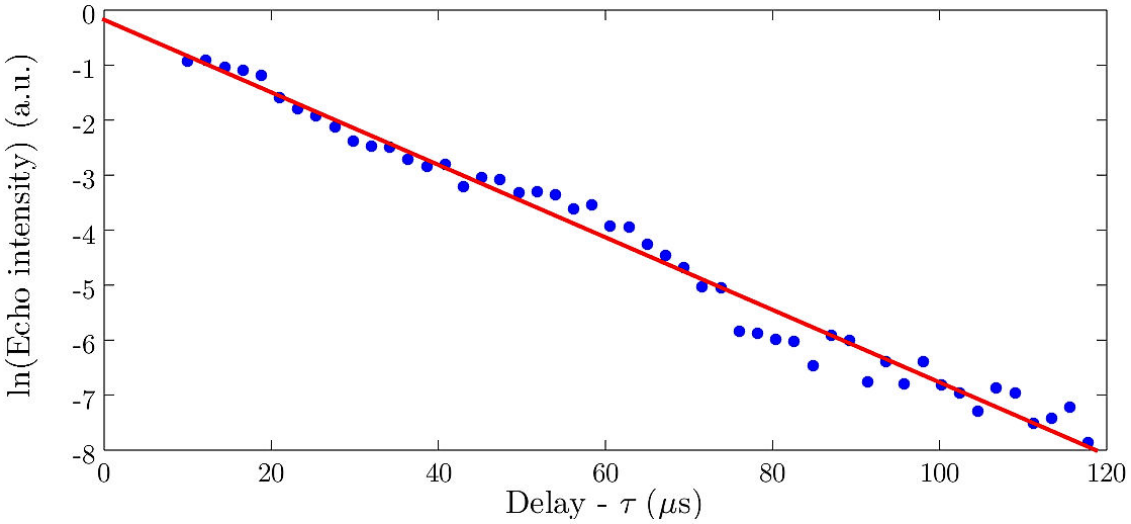

Figure 6.22: Photon echo intensity with increased delay time. The pulse lengths were $\pi/2 = 2$ μs and $\pi = 5$ μs. The optical coherence time was measured to be 121 ± 1 μs. Laser input power on the grating was 2.1 ± 0.05 mW.

To measure the homogeneous linewidth, photon echo experiments were performed. The pulse lengths were 2 μs for the $\pi/2$ pulse and 5 μs for the π pulse. This was because on the day of two-pulse echo measurements, these pulse lengths were giving the biggest echo intensity. The Rabi frequency was measured the next day by changing the π pulse length.

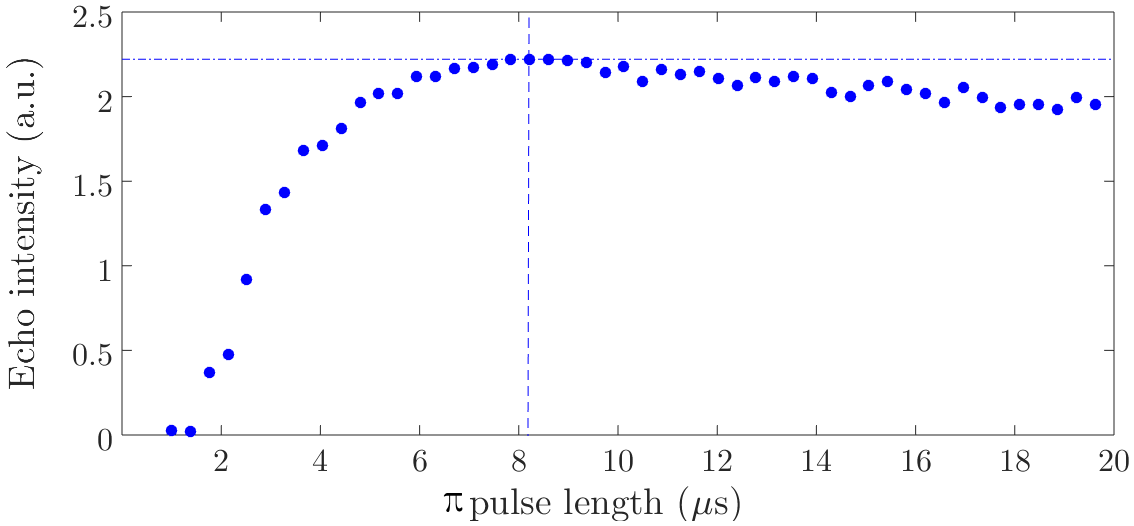

Figure 6.23: The π pulse width was increased and echo intensity was measured using grating coupling. The Rabi frequency was measured, using t_π of 8 μs which gave the maximum echo intensity, to be 392 kHz. Laser input power on the grating was 1.8 ± 0.05 mW.

One echo sequence can be observed in Figure 6.21. Figure 6.22 shows the averaged maximum intensity of the photon echo as a function of the delay τ between the $\pi/2$ and π pulses. The optical coherence time T_2 was 121 ± 1 μs, corresponding to a homogeneous linewidth of 2.6 ± 0.3 kHz. The biggest echo intensity at t_π of 8 μs, gave an estimate of the Rabi frequency to be 392 kHz. Figure 6.23 shows the echo intensities for different π pulse lengths. The reported T_2 in Reference [2], considering the broadening effect of ISD, as explained in Section 2.3.1, was 111 ± 4 μs. In Reference [2], 1 μs pulses were used which were smaller than our pulses, and so their Rabi frequency was higher than what has been measured here. Hence, less ions were being excited in our experiments, and so the measured coherence time was slightly longer.

The transition dipole moment was the same as the bulk crystal amount of $\mu = 1.59 \times 10^{-32}$ Cm, corresponding to an oscillator strength of f= 3×10^{-7} [2]. With the above measured Rabi frequency and the transition dipole moment, the electric field in the substrate was calculated. From these calculations, the power coupled to the ions in the substrate was about 2.5 μW. With a film thickness of 380 ± 10 nm, the power ratio in the substrate to the film can be calculated to be $9.6 \pm 0.1\%$. Therefore, from the power coupled to the substrate and this ratio, the power coupled to the film was about 23.6 μW, which is $1.3 \pm 0.1\%$ of the total laser power of 1.8 ± 0.05 mW on the grating. As mentioned before, the gratings have to be further investigated to obtain better efficiencies.

6.4.6 Spin state lifetime of $0.05\%Pr^{3+}:Y_2SiO_5$ substrate

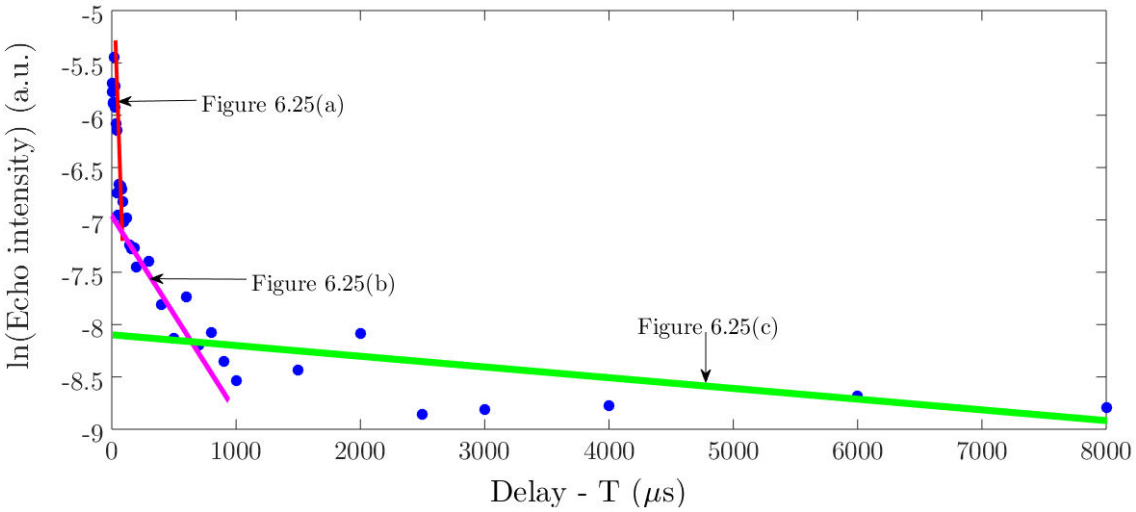

Figure 6.24: 3 pulse echo sequence with increased wait time. The pulse lengths were $\pi/2 = 5$ μs and $\pi = 5$ μs with a delay of 20 μs between the two pulses and T was increased from 5 μs to 8 ms. Three slopes can be observed in the exponential decay curve. Laser input power on the grating was 2.45 ± 0.05 mW.

To manipulate the ground state nuclear spin level lifetime, a stimulated echo measurement was performed. A 3-pulse photon echo series was used to create a spectral grating, which was then probed with a further $\pi/2$ pulse after a wait time of T. The pulse lengths were $\pi/2 = 5$ μs and $\pi = 5$ μs with a delay of 20 μs between the two pulses and T was increased from 5 μs to 8 ms.

Figure 6.24 shows the echo intensity as a function of the wait time of T. Three slopes were observed on the exponential decay curve. Figure 6.25 shows the three decays separately. There was a very fast decay observed in the first 45 μs as observed in Figure 6.25(a), with a decay rate of 59 ± 5 μs, followed by a decay with a rate of of 303 ± 5 μs as shown in Figure 6.25(b). After a wait time of 400 μs, a decay rate of about 9 ± 1 ms was observed as shown in Figure 6.25(c). As these decay rates were on a much shorter time scale compared to what has previously been reported [69], I could not assign each decay to a ground state transition frequency.

In Reference [69], the ground state hyperfine lifetimes were about 200 s for temperatures of 4.2 K and 2 K. Holliday *et. al* showed that the ground state hyperfine lifetime was very temperature dependent, and for site 1, holes could not be seen at temperatures of above 8 K. So the most likely reason for the significant reduction in the hyperfine state lifetime was the elevated temperature of the waveguides.

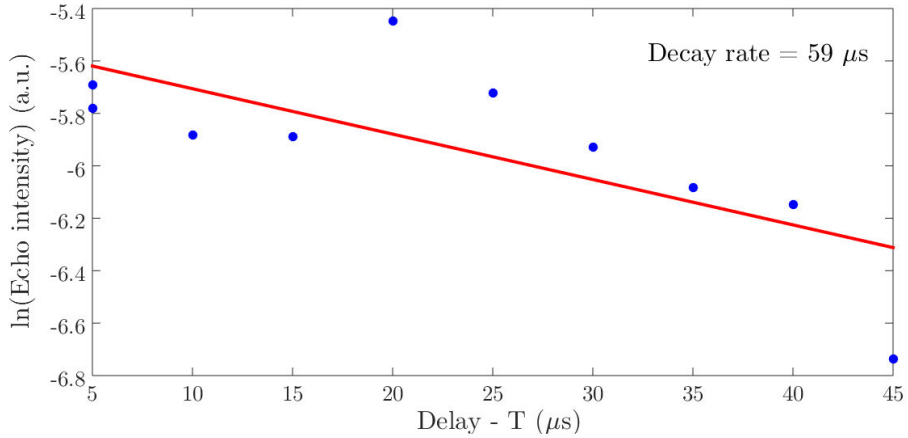

(a)

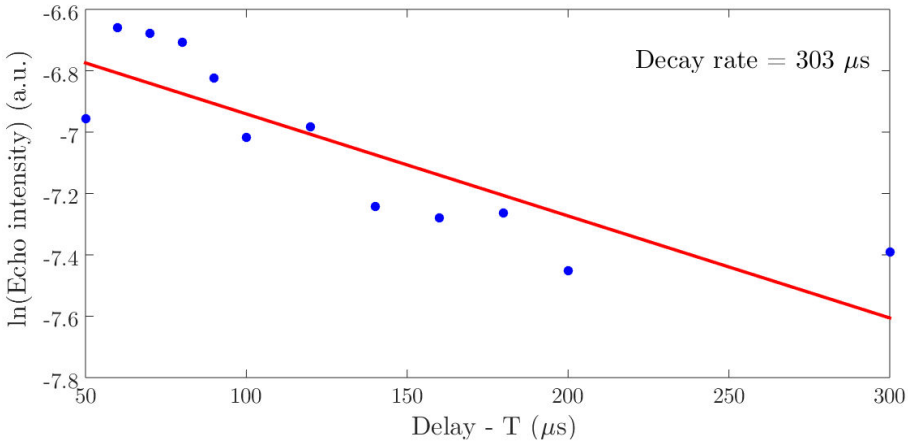

(b)

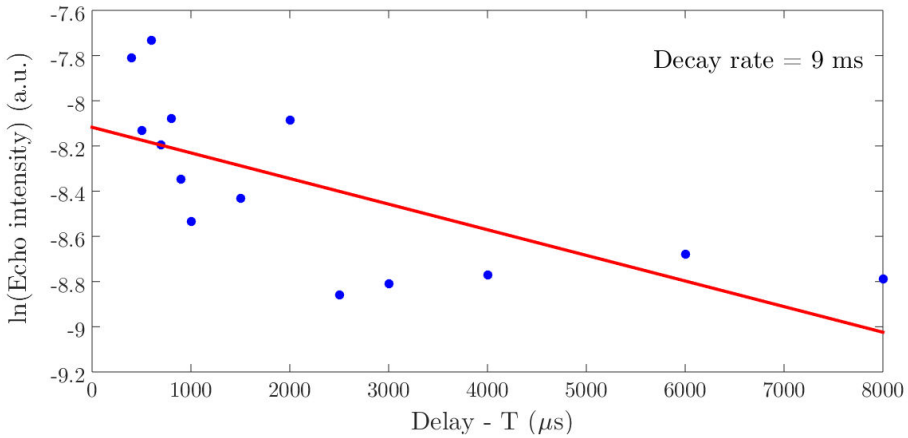

(c)

Figure 6.25: Showing the three slopes of Figure 6.24 separately. Three decay rates of 59 ± 5 μs, 303 ± 5 μs and 9 ± 1 ms were observed. Scattering in the data could be due to external vibrations causing the coupling efficiency to change during the experiment.

6.5 Stark shift effect and electronic control

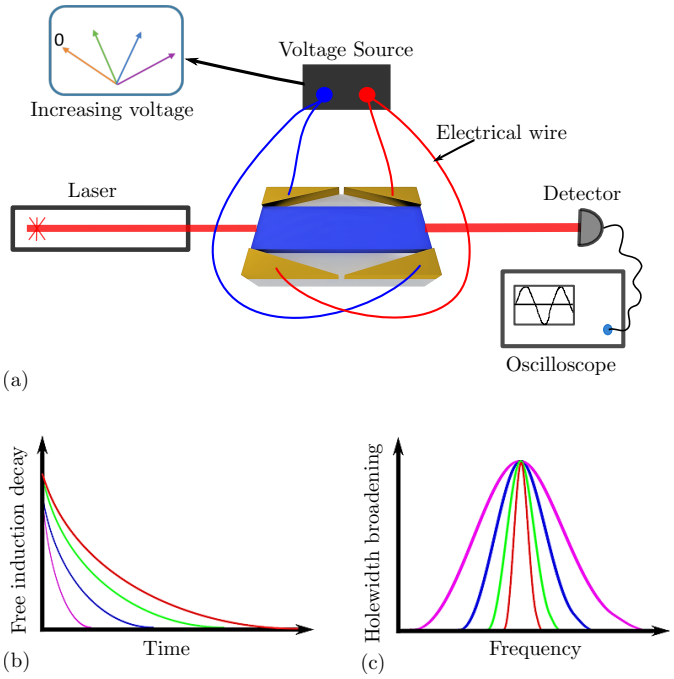

Figure 6.26: Stark shifting experimental setup, (a) Simplified illustration of placing voltage on electrodes on the thin film, (b) and (c) As the measured speed of the free induction decay increases, the holewidth broadening becomes larger.

As mentioned in Section 5.4, triangular electrodes were designed to produce linear electrical fields parallel to the D_2 crystalline axis of Pr^{3+}:Y_2SiO_5. For this purpose, as discussed in Section 4.4, 100 nm thick gold electrodes were deposited onto the TeO_2 thin film to Stark shift the active Pr^{3+} ions in the Pr^{3+}:Y_2SiO_5 substrates. Initial experiments were carried out to determine whether the active ions of Pr^{3+} in the substrate of the proposed waveguides could be electrically controlled. A simplified schematic of this experimental setup is shown in Figure 6.26. The dye laser used in this part of the experiment was the Coherent 699-29, which was frequency stabilized by locking to an external Ultra-Low Expansion (ULE) cavity [180] . The input laser power on the sample was 2.1 ± 0.05 mW. The center frequency of the laser was set to 494.72051 THz (605.98348 nm). A two pulse delayed FID experiment with a long $\pi/2$ pulse (1000 μs) compared to the π (5 μs) pulse with a delay of 200 μs was conducted as shown in Figure 6.27. This resulted in burning of a spectral hole.

As can be observed in the schematic, the voltage connected to the electrodes on the thin film was turned on at the start of the 200 μs and stayed on when the π pulse was applied. The free induction decay curve of this last pulse was detected

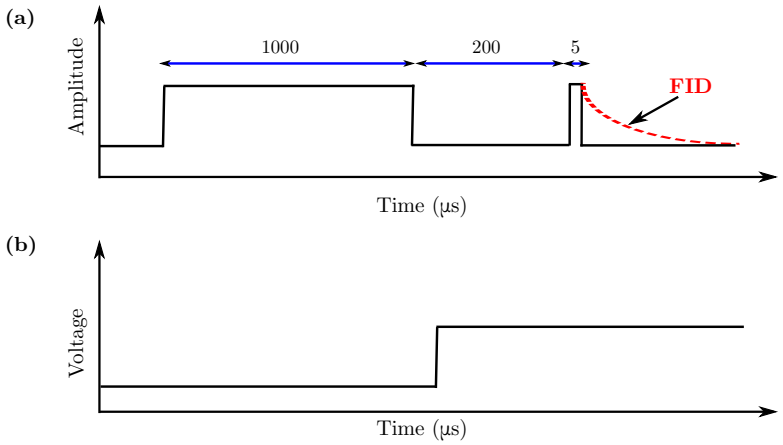

Figure 6.27: Delayed FID pulse sequence, (a) Delayed FID, large initial pulse (1000 μs) is applied, followed by a smaller π pulse (5 μs) after a long delay (200 μs). (b) Voltage is applied to the electrodes at the start of the 200 μs and stays on when the π pulse is applied. The amplitudes in the first figure are illustrated to show the pulse sequence and their values are arbitrary and not to scale.

by a PMT and the signals were observed on the digital oscilloscope. The spectral holewidth broadening and the free induction decay curve have a Fourier transform relationship. As is illustrated in Figure 6.26, the longer free induction decays are an indication of narrower holes. Figure 6.28 shows how to calculate the width of spectral holes, with respect to the initial hole at 0 mV and the π (5 μs) pulse, at different voltages. As can be observed, the initial spectral hole is convolved with a square pulse in frequency space. The result is then multiplied (mixed) with the Fourier transform of the π pulse. By changing the width of the square pulse the final resultant spectra are the spectral holes at different voltages. The square pulse width is changed to match the spectral width of each hole observed at the different voltages in the experiment.

Table 6.1 shows the obtained width of the square pulses and the respective width of the hole observed in the experiment. From the calculations of Section 5.4, it can be calculated that the increase in holewidth broadening caused by a voltage change of 100 mV would be about 0.45 ± 0.1 MHz, which is within the uncertainty of the increase of 0.55 ± 0.2 MHz as observed in Table 6.1. Three of the resultant spectral holes obtained from the experiment and calculated using Figure 6.28 are shown in Figure 6.29.

The width of the obtained square pulses and their respective voltages are shown in Figure 6.30. A linear relationship between the width of the square pulse and voltage was expected. As can be observed, the relationship was linear up to 400 mV, but was damped after this voltage. This is because the π pulse used was a 5 μs pulse,

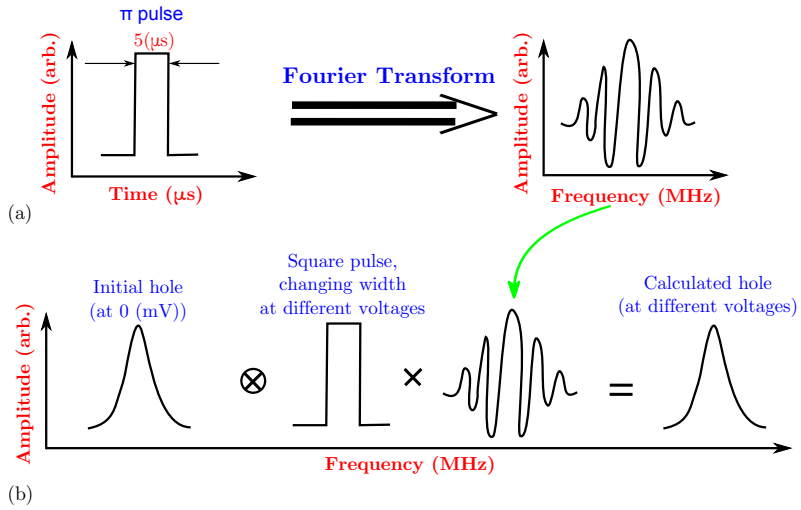

Figure 6.28: (a) The Fourier transform of the utilized π pulse is calculated. (b) The initial hole at 0 mV is convolved with a square pulse. The result is then mixed with the sync spectrum obtained from the square π pulse. The width of the square pulse that is convolved with the initial hole, is changed such that the calculated spectrum for each voltage matches the spectrum obtained from the experiment.

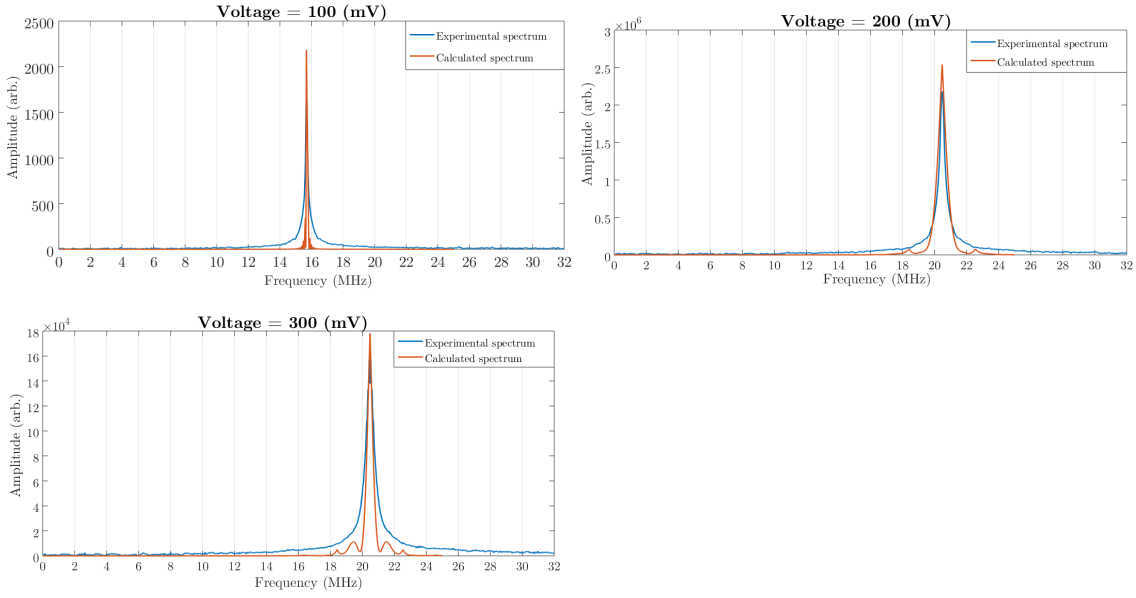

Figure 6.29: The spectral holes obtained from the experiments and the calculated spectral hole of each voltage can be observed. As the voltage was increased, the holewidth broadened.

resulting in a 200 kHz pulse in frequency space. As can be seen from Table 6.1, at voltages of 400 mV to 600 mV, the spectral hole is wider than 200 kHz and so cannot be resolved properly. In the next series of experiments, smaller π pulses should be used to obtain better results.

Voltage (mV)	Experimental Signal FWHM (Hz)	Square Pulse FWHM (Hz)
0	56500	56550
100	94100	94050
200	168000	167750
300	242000	241650
400	325000	324550
500	361000	361050
600	382000	381700

Table 6.1: The full width half maximum (FWHM) of the experimental spectrum and the relevant square pulses were calculated at different voltages. The increase in holewidth broadening caused by a voltage change of 100 mV was about 0.55 ± 0.2 MHz

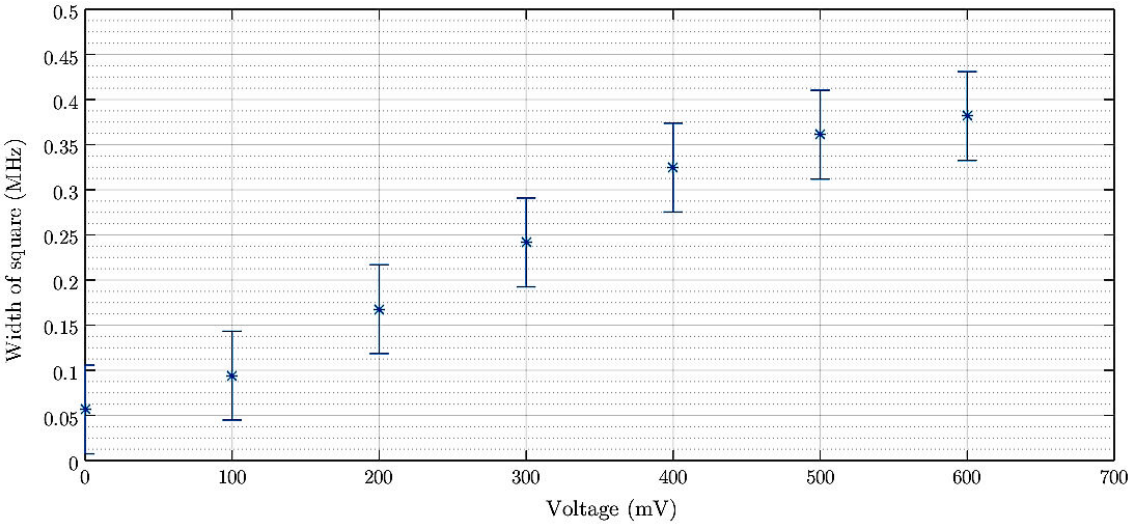

Figure 6.30: The width of the square pulses in frequency space and the respective voltage should have a linear relationship which can be observed up to 400 mV. After this voltage, as can be seen, the curve is not increasing linearly. The non-linearity was caused by the π pulse length.

6.6 Summary

Rare-Earth ion doped optical waveguides of TeO_2 glass on Pr^{3+}:Y_2SiO_5 have been experimentally demonstrated. Optical photon echo experiments using the evanescent field in the Pr^{3+}:Y_2SiO_5 substrate have shown that the optical coherence properties of the near surface ions of Pr^{3+} haven't changed significantly compared to the bulk samples with similar doping concentrations. The inhomogeneous linewidths, optical coherence times and spin lifetimes have been measured using both prism coupling and grating coupling of light into the TeO_2 thin film.

Two discrepancies in the results were the optical coherence time measured in the prism coupling experiment on the thin film with the $0.005\%Pr^{3+}:Y_2SiO_5$ substrate and the spin lifetime measured in the grating coupling experiment of the thin film with the $0.05\%Pr^{3+}:Y_2SiO_5$ substrate. The slight decrease of the optical coherence time was attributed to laser instability. The significant decrease in the spin lifetime in the grating coupling experiment was probably due to the elevated temperature in the cold finger cryostat compared to the bath cryostat. The spin state lifetime can be increased by lowering the sample temperature during the experiment.

The effect of applying an electric field to the electrodes on the waveguide was observed. The increase measured in the holewidth broadening in these experiments was similar to the calculated values of Section 5.4, showing that a voltage change of 100 mV would cause an increase in the broadening of about 0.55 ± 0.2 MHz as observed in Table 6.1. By increasing the applied voltage, a holewidth broadening varying linearly with the voltage should have been obtained. The observed non-linearity at voltages of 400 mV to 600 mV, was due to the fact that the π pulse used was a 5 μs pulse, resulting in a 200 kHz pulse in frequency space. As can be seen from Table 6.1, at voltages of 400 mV to 600 mV, the spectral hole is wider than 200 kHz and so can not be observed properly. In the next series of experiments, smaller π pulses will used to obtain better results.

These experimental results show that this passive waveguide architecture is a practical method and can be used to build linear optical quantum processing devices required in a quantum repeater circuit.

Chapter 7

Discussion

The results of the experiments performed using the waveguide designed in this thesis show that the optical coherence properties of the Pr^{3+}:Y_2SiO_5 substrate, including inhomogeneous and homogeneous linewidths and hyperfine state lifetimes, were similar to the bulk sample measurements. These measurements are collected and presented in Table 7.1. This result was not completely expected because the Pr^{3+} ions at the interface are in close proximity to the TeO_2 glass. Glass is quite

	No magnetic field T= 2 K		**Small magnetic field** T≈ 4 K	
	$0.005\%Pr^{3+}$:Y_2SiO_5	TeO_2 on $0.005\%Pr^{3+}$:Y_2SiO_5	$0.05\%Pr^{3+}$:Y_2SiO_5	TeO_2 on $0.05\%Pr^{3+}$:Y_2SiO_5
Γ_{IH} (GHz)	2 [154]	2 ± 0.1	10 [1]	10 ± 0.1
T_2 (μs)	160 [154]	70 ± 5	111 ± 4 μs [2]	121 ± 5
$T_{1(spin)}$ (s)	10 ± 0.7 [181]	9.8 ± 0.3	10 ± 0.7 [181]	$(9 \pm 1) \times 10^{-3}$

Table 7.1: A summary of the results obtained in the experiments. The magnetic fields and approximate temperatures for each set is shown. As can be observed, the inhomogeneous linewidth (Γ_{IH}) was the same as bulk measurements. The optical coherence times (T_2) obtained in the zero magnetic field data showed a reduction in the T_2. The reason for this is mentioned in Section 6.2.3. In the small magnetic field experiments, optical coherence times were similar to bulk numbers. The spin state lifetimes ($T_{1(spin)}$) were similar to bulk measurements in the zero magnetic field data, but due to elevated temperatures there was a reduction in the the spin state lifetimes in the small magnetic field experiments.

a different system from crystal due to the large level of disorder. As a reference, rare-earth absorption lines in glasses have linewidths of 100 to 500 cm^{-1}, which is about four orders of magnitude broader than inhomogeneous lines of rare-earth

crystals of about 1 to 10 GHz [103, 184]. For example, Eu^{3+} in silicate glass has an inhomogeneous broadening of 100 cm^{-1}, whereas the inhomogeneous linewidth of Eu^{3+} in $YAlO_3$ was measured to be about 0.17 cm^{-1} [103].

The homogeneous linewidth could also be expected to be different near the glass interface. The density of phonon states in a glass is very different to that in a crystal. The density of phonon modes in a crystalline material decreases rapidly at lower frequencies, but this is not the case in glass. As a result, the dynamics of rare-earth sites in glasses are radically different to sites in crystals. For example, Eu^{3+} in silicate glass has a homogeneous linewidth of about 25 MHz, whereas in Eu^{3+} in $YAlO_3$ the homogeneous linewidth was about 5.5 kHz [103, 184]. So it was not clear what would happen to the homogeneous linewidth at the interface of the glass thin film and crystal substrate. Further, ground state lifetimes of Eu^{3+} in silicate glass have been measured to be about 160 s [185] which is very small compared to the ground state lifetime of 23 days in Eu^{3+}:Y_2SiO_5 [68]. From the experiments in Chapter 6, it can be concluded that the phonon density of the glass thin film has not affected the coherence properties of the Pr^{3+} ion.

The key findings presented in the preceding chapters, showing that the active region in a waveguide does not have to be the core, were published in 2014 [105]. Since publishing this work, other researchers have used this technique. For example, there has been investigations using evanescent coupling in silicon photonic waveguides and micro-resonators fabricated on Er^{3+}:Y_2SiO_5 substrates [186].

In the work by Miyazono *et al.* [186], amorphous silicon ring resonators were evanescently coupled to Er^{3+} ions in the bulk substrate of Er^{3+}:Y_2SiO_5 at 4.5 K. Er^{3+} ions were used due to their long optical lifetime and transition wavelengths of 1550 nm in the telecommunication band. The Er^{3+} ions were probed evanescently and their optical properties, such as the inhomogeneous linewidths and excited state lifetimes, were characterized and compared with bulk sample measurements, showing little change from bulk numbers.

Critical to any quantum information device will be the fabrication of extremely low loss waveguides. TeO_2 and Y_2SiO_5 are intrinsically low loss materials. Currently, the main source of loss is likely to be due to scattering from the roughness on the interfaces of the waveguide. Scattering of light can be observed in Figure 6.17. Figure 7.1 shows an electron microscope image of the thin film surface of the waveguide used in the experiments in Chapter 6, on a μm scale. As can be seen in this picture, currently there are a lot of imperfections on the surface of the thin film that can be associated with scratches of the substrate and those are likely to be the

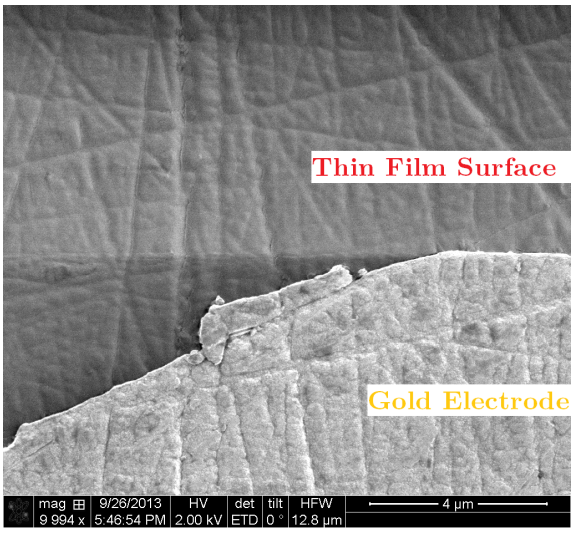

Figure 7.1: Scanning electron microscope image of TeO_2 thin film and gold electrodes. As is observed, the surface of the substrate had many scratches. The surface quality of the substrate can affect the thin film quality, hence a better and cleaner surface is required.

main source of losses in the waveguide. One of the factors that need to be further investigated in future work is whether the methods of polishing could be modified so as to achieve higher quality surfaces.

The experiments in this thesis were performed in slab waveguides because they are easier to manufacture and couple into, but it will be desirable in the future to move to ridge waveguides. In moving from slab waveguides to ridge waveguides, the scattering from the side walls could become significant. Very low loss ridge waveguides using TeO_2 thin films on silica under-cladding on silicon have been constructed by Madden *et al.* [24] and optical losses of about 0.05% were measured in most of the near-infrared spectrum. Given high quality substrates, it is expected that similar results could be achieved in TeO_2 on Y_2SiO_5 structures, so there are reasonable prospects of fabricating low loss ridge waveguides.

In ridge waveguides the side walls could also cause additional stress on the active rare-earth substrate ions. This additional stress could cause the optical coherence properties, like the inhomogeneous linewidth and the coherence times, to change. Investigation into the effect of the ridge on the substrate ions can be done using the high-spatial-resolution hole-burning method introduced by Bartholomew [59]. He built a nanometer-resolution confocal microscope with a magnification of about 100×. Using this high-resolution confocal microscope, the optical coherence properties of the rare-earth sample, can be examined in different spatial regions of the crystal. Both the near-surface ions and the ions that could be under residual stress

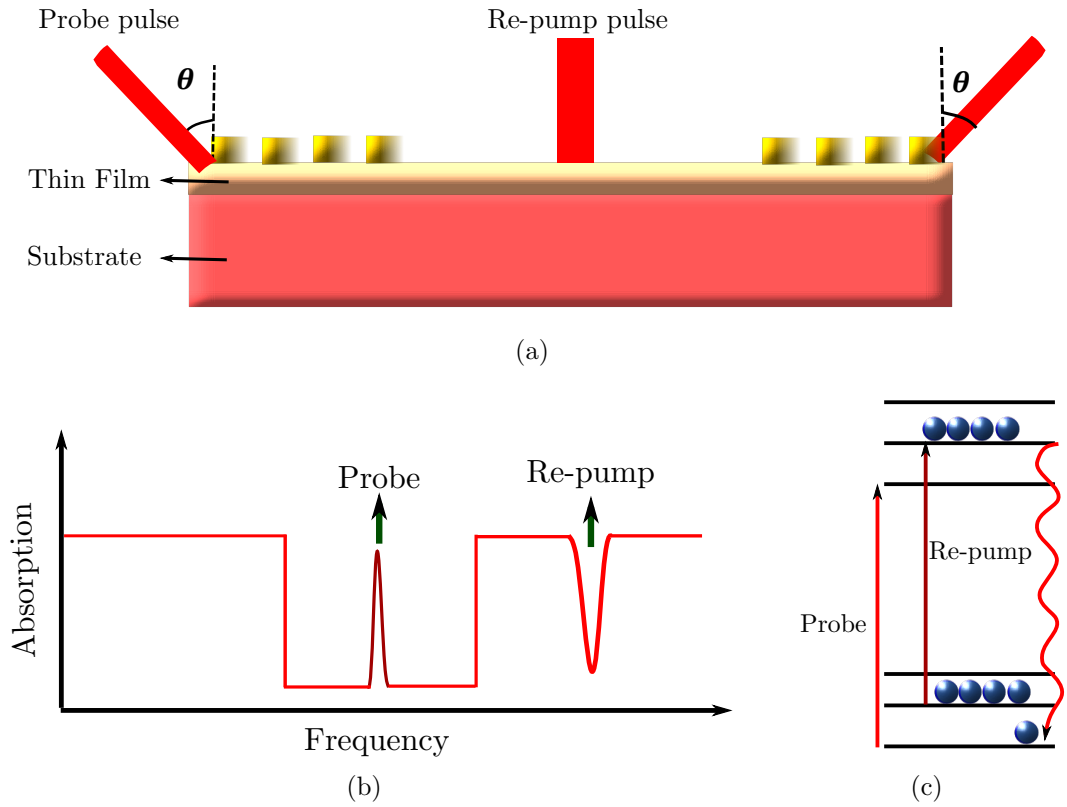

Figure 7.2: An experiment for measuring waveguide properties in different parts of a waveguide. By measuring the relative Rabi frequencies in different locations, the thin film surface quality and the thin film loss can be quantified.(a) Schematic of the waveguide with the input probe beam and re-pump beam shown. (b) A trench can be made in frequency space along the entire waveguide and some ions can be burnt back into the trench at a particular position along the waveguide. By using photon echo techniques, the local field intensity can be measured and so the efficiency of different locations on the waveguide can be calculated. (c) Energy level diagram of probe pulse on a particular transition, with the burn back pulse bringing some ions back into the emptied state.

caused by the side walls of the ridge can be examined. In the experiments performed by Bartholomew, the near-surface ions' optical coherence properties showed very little change compared to bulk sample measurements. However, the results of optical coherence property measurements on a scratch on the surface of the crystal showed large static and dynamic changes to the structure of the crystal, with parts up to about 20 μm to the scratch showing polycrystalline behavior. The scratch on a crystalline material is a far more drastic change induced in the crystal structure compared with the soft glass that we are fabricating on top of these crystals. So the prospect of depositing a ridge glass waveguide onto the crystal surface without affecting the optical coherence properties of the crystalline substrate is very promising.

In optimizing future waveguides, it will be necessary to accurately measure the loss. This is a difficult measurement, and the standard technique, which involves cutting the waveguide into pieces and measuring the efficiency of the pieces, is destructive. The difficulty is in separating the coupling losses into and out of the waveguide from the losses intrinsic to the waveguide. The long ground state hyperfine lifetimes suggest a non-invasive technique to measure the losses in the waveguide. As shown in Figure 7.2, light can be coupled into the thin film and then using another beam one can probe the intensity of light at different parts of the crystal. Then by using photon echo techniques, the relative Rabi frequency can be measured. Using these Rabi frequencies, one can determine the local field intensity in the waveguide in that particular region and from this, the coupling efficiency of the waveguide at these different parts can be calculated. This method of measuring the losses in the waveguide can also be used to measure the decrease of the interaction strengths as the mode is pushed in and lifted out of different devices built by tapering the thin film as described in Section 3.2.

7.1 Grating coupling efficiency

As discussed in Section 5.3, the more suitable method of coupling to quantum processor chips in the long term is taper coupling, it is worth considering the difficulties encountered in achieving good coupling efficiencies with the gratings used here as it indicates general problems with the fabrication processes. Further, we are most likely going to use gratings for the fabrication of cavities in the waveguide structures. The efficiencies of the gratings in my experiments were much lower than expected from the modeling presented in Section 5.3.2. For example, the expected efficiency for a depth of 170 nm was calculated to be about 60%, but was measured to be about 2%. There were a number of factors that could have contributed to the poor coupling efficiency including inaccuracy in the film thicknesses, instability in the periodicity of the gratings, incorrect depth of the gratings, the roughness of the surface on which the gratings were written on, and poor overall shape of the gratings.

The inaccuracy of the film thickness and unstable pitch could have possibly contributed to the loss in efficiency, but is unlikely to be responsible for the 10× reduction seen. From the grating images observed using the SEM system, as shown in Figure 6.15, the pitch is stable. If the periodicity of the pitch was very unstable, one would expect a large band of angles where the coupling efficiency was similar.

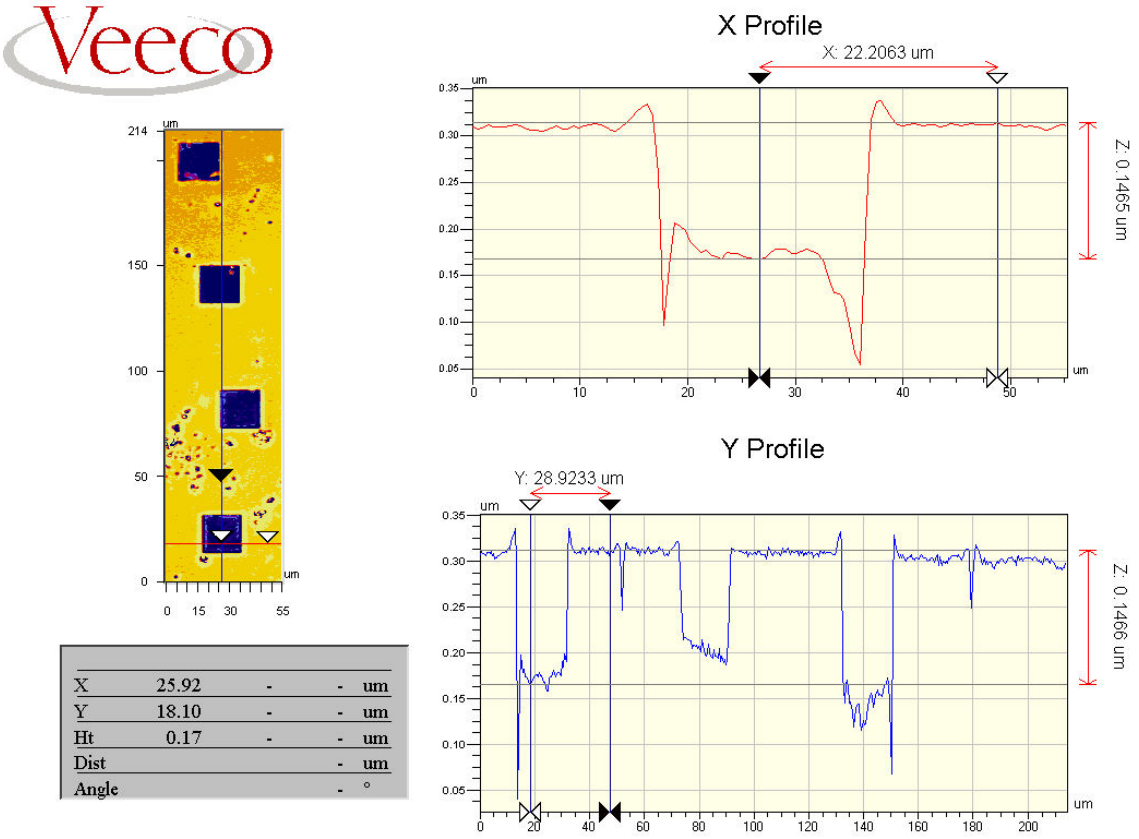

Figure 7.3: Wyko NT9100 Optical Profiling microscope image of four gratings, from top to bottom, with a depths of 110 nm, 130 nm, 150 nm and 170 nm. The x and y profiles were observed for the 170 nm grating. The measured depths shown here were average depths. As can be observed the average depth shown was about 146 nm, which was much larger than expected.

However, the coupling angle was quite sharp to about 0.5°, so any slight drift in the pitch is not the cause of the loss in efficiency. Further, the thickness of the films was 380 ± 10 nm, and this 2.6% change does not account for such a big loss of efficiency at the different depths that have been fabricated.

As can be observed in Figure 5.8, the efficiency of the gratings is very dependent on the depth. To examine this factor further, the gratings were observed under a Wyko NT9100 optical profiling microscope [187]. Figure 7.3 shows the optical profiler image of a sample with four gratings, with depths of 110 nm, 130 nm, 150 nm and 170 nm, respectively from top to bottom. The 170 nm grating was expected to show an efficiency of about 60%, but the actual efficiency of this grating was about 2%. The grating depths shown by the optical profiling microscope are average depths. The optical profiler averages depth over the grating structure. For the particular structure used here, this is expected to result in a depth 50% smaller that the true depth as shown in Figure 7.4(a). For the 170 nm deep grating, the

average depth observed on the optical profiler was about 146 ± 50 nm which is much deeper than the expected value of 85 nm. A likely explanation is that the gratings were eroded during the milling process, resulting in a larger average depth as shown in Figure 7.4(b). This is supported by the fact that the deeper the gratings were, the higher the observed efficiency and that there was no turning point such that a deeper grating was less efficient than a shallower grating before it. This could be caused by the charge buildup in the conductive layer, or because the effective resolution of the FIB is a lot lower than expected, so sharp edges could not be written.

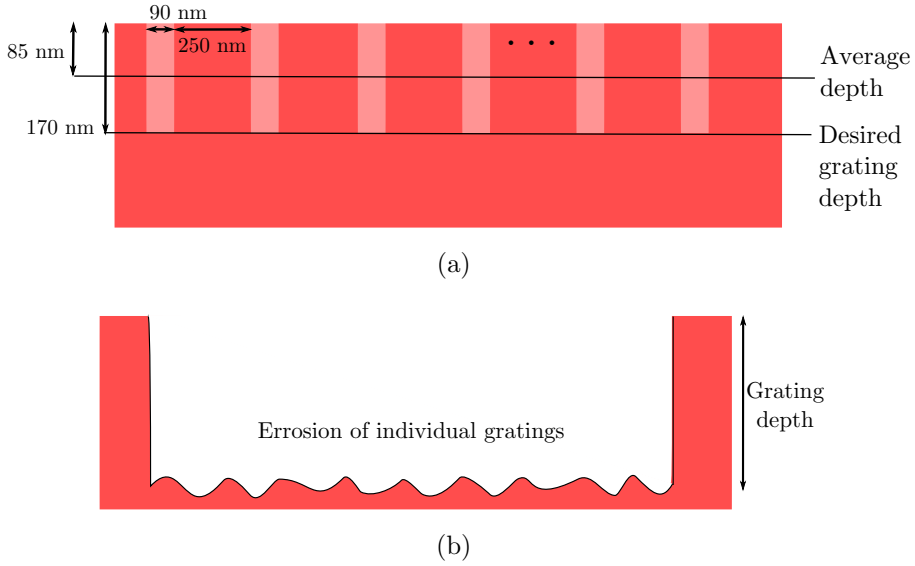

Figure 7.4: (a) Ideal 170 nm grating, average depth should be about 85 nm, (b) Gratings were completely eroded as the grating lines were milled into the thin film, so average depth seen by the optical profiler is about 146 ± 50 nm.

The conductive layer used in this thesis was a thin layer of carbon. Other materials which provide an electrically conductive and smooth surface could also be used for this purpose. The nano-scale and quantum optics group at Caltech [188] are also using a FIB to write different structures on their quantum nano-photonic devices based on rare-earth doped crystals. They are mainly using Chromium (Cr) as their conductive layer, as it forms a very hard homogeneous and flat layer. In their structures, the Cr layer can later be etched off chemically. The problem with Cr in the designed planar waveguides of this thesis is that the Cr etchants are typically mixtures of perchloric acid diluted in water and ceric ammonium nitrate [189], which would also remove the TeO_2 thin film due to its sensitivity to aqueous solutions. Hence, other electrically conductive media have to be explored which form a more homogeneous layer than carbon and can be etched off later without affecting the glass thin film. Another direction that could be taken would be to replace the TeO_2 thin film with one that is less sensitive to water. However, that would mean finding

a thin film with the very low losses achieved in TeO_2 thin films and less sensitive to humidity. This is a question that will be investigated in further experiments.

7.2 Electronic control

I demonstrated electric control of Pr^{3+} ions in a TeO_2 on Pr^{3+}:Y_2SiO_5 waveguide by applying an electric field to the waveguide as mentioned in Section 6.5. The electric field at different parts of the waveguide could be characterized by using the same concept shown in Figure 7.2. By preparing a trench, then using a burn back beam at different parts of the crystal, while the electric field is being turned on and off, one can characterize how the electric field affects the rare-earth ions.

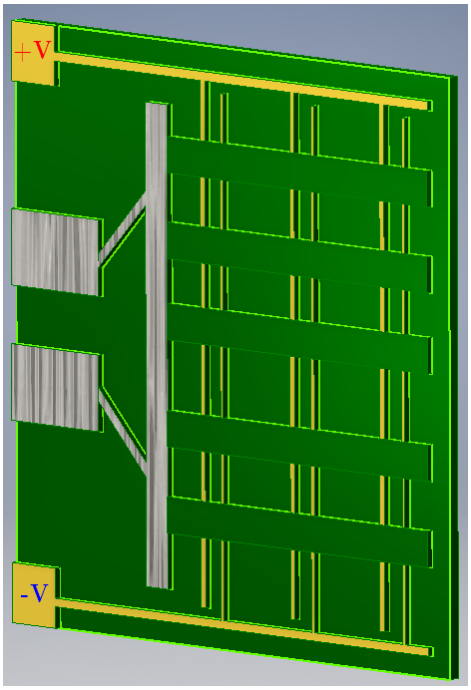

Figure 7.5: Example illustration of a flip on PCB. A similar PCB can be designed and attached on to the top of the thin film, bringing the required voltages to the different devices on chip.

For complex circuits with a lot of components, the electrodes and electrical paths between the electrodes may have to go over the waveguide regions like what is shown in Figure 3.2. Therefore, one might need to find a method of connecting the electrodes on the integrated circuit to voltage without disturbing the waveguide. This can be achieved using a flip on board, like the illustration shown in Figure 7.5 with all the necessary connections, which flips onto the waveguide and attaches the electrodes to the desired voltage. This board could be a printed circuit board (PCB)

with all the relevant connections and electrical paths printed onto the board. This design would be advantageous because it wouldn't disturb the waveguides on the integrated circuit.

Chapter 8

Conclusion

In the architecture proposed in this thesis, a high-refractive-index thin glass film of TeO_2 was deposited on the surface of an active rare-earth ion crystal substrate of Pr^{3+}:Y_2SiO_5. The light guided in the waveguide interacted with the near surface Pr^{3+} ions via the evanescent field which extended into the substrate. The result was an effective waveguide, which has shown no significant undesirable effects on the optical coherence properties of the Pr^{3+} ions in the substrate. In this method, by using the substrate as the active region rather than the core, an alternative way of building a linear optics quantum processor chip incorporating quantum memories and sources is presented.

In order to prove that the proposed waveguide architecture had not significantly changed the coherence properties of the substrate rare-earth ions, a first set of experiments were performed in which the optical coherence properties were compared with bulk samples of the same dopant concentration. These experiments showed that the coherence properties of the near surface rare-earth ions were quite similar to the bulk sample measurements. This proved that depositing a glass thin film on the surface of these crystals had not placed additional stress on the near surface ions which were being probed by the evanescent field penetrating the substrate.

In these initial measurements, prism coupling was used to couple light into the waveguide. With the aim of moving towards practical quantum photonic integrated circuits, the method of coupling light into the waveguide was changed to grating coupling. Similar coherence experiments were performed on these thin films, and the grating efficiencies were measured and compared to the results obtained from modeling the gratings. These experiments were performed in a cold finger cryostat rather than the bath cryostat used for previous measurements. While this means that the waveguide was isolated from contamination, the temperature was higher and difficult to measure. This resulted in lower hyperfine spin lifetimes compared to bulk samples.

After establishing that the deposition of the glass thin films and writing gratings on the surface of these films had not substantially affected the coherence properties of the active Pr^{3+} ions in the substrate, gold electrodes were deposited on these waveguides to perform Stark shifting experiments and demonstrate holewidth broadening with increased voltage. The results obtained in this Section showed that the magnitude of the observed holewidth broadenings were close to what was predicted from the modeling calculations.

The achievement of narrow inhomogeneous and homogeneous linewidths, negligible material-related spectral diffusion and long hyperfine state lifetimes in the waveguides, leads to future research focusing on fabricating and demonstrating waveguide-based devices such as gradient echo quantum memories and single photon sources. The ultimate aim is to combine such quantum components with other active and passive devices into a single, large scale integrated circuit. The achievable photonic circuitry paired with the fast and precise control of the substrate ion ensembles with electric fields will allow new regimes of rare-earth ion quantum optics to be probed in addition to facilitating research towards practical quantum communication and computing technology.

Bibliography

[1] M.P. Hedges. *High Performance Solid State Quantum Memory*. PhD thesis, Australian National University, 2011. (cited on pages vii, 9, 19, 92, 93, 100, 115, and 125)

[2] R. W. Equall, R. L. Cone, and R. M. Macfarlane. Homogeneous broadening and hyperfine structure of optical transitions in Pr^{3+}:Y_2SiO_5. *Physical Review B*, 52(6):3963–3969, August 1995. (cited on pages vii, 18, 35, 69, 70, 71, 102, 117, and 125)

[3] S.R. Mieth. *Preserving Atomic Coherences for Light Storage in Pr^{3+}:Y_2SiO_5 Driven by an OPO Laser System*. PhD thesis, Technische Universität, Darmstadt, 2016. (cited on page vii)

[4] F.R. Graf, A. Renn, U.P. Wild, and M. Mitsunaga. Site interference in stark-modulated photon echoes. *Phys. Rev. B*, 55:11225–11229, May 1997. (cited on pages vii, 16, 54, and 94)

[5] D. Dieks. Communication by epr devices. *Physics Letters A*, 92(6):271 – 272, 1982. (cited on page 1)

[6] N. Sangouard, C. Simon, H. de Riedmatten, and N. Gisin. Quantum repeaters based on atomic ensembles and linear optics. *Reviews of Modern Physics*, 83(1):33–80, March 2011. (cited on pages 1, 2, 6, and 49)

[7] W.K. Wootters and W.H. Zurek. A single quantum cannot be cloned. *Nature*, pages 802 – 803, 1982. (cited on page 1)

[8] H.J. Briegel, W. Dür, J. I. Cirac, and P. Zoller. Quantum repeaters: The role of imperfect local operations in quantum communication. *Phys. Rev. Lett.*, 81:5932–5935, Dec 1998. (cited on page 1)

[9] A.G. Radnaev. Telecom fiber optic interface for long-lived quantum memory. http://people.physics.gatech.edu/~aradnaev3/research.html. (cited on page 4)

[10] Intel updates core i7 line with its first eight-core desktop chip. http://www.v3.co.uk/v3-uk/news/2362508/

intel-updates-core-i7-line-with-its-first-eight-core-desktop-chip. (cited on page 5)

[11] Triode vacuum tubes. http://en.wikipedia.org/wiki/Triode. (cited on page 5)

[12] Twists and turns in the development of the transistor. http://www.todaysengineer.org/2003/May/history.asp. (cited on page 5)

[13] The chip that jack built. http://www.ti.com/corp/docs/kilbyctr/jackbuilt.shtml. (cited on page 5)

[14] M. Zhong, M.P. Hedges, R.L. Ahlefeldt, J.G. Bartholomew, S.E. Beavan, S.M. Wittig, J.J. Longdell, and M.J. Sellars. Optically addressable nuclear spins in a solid with a six hour coherence time. *Nature*, (517):177–180, 2015. (cited on pages 6, 8, 18, 38, 39, 45, 53, and 57)

[15] M. Razavi, M. Piani, and N. Lütkenhaus. Quantum repeaters with imperfect memories: Cost and scalability. *Phys. Rev. A*, 80:032301, Sep 2009. (cited on page 6)

[16] E. Saglamyurek, N. Sinclair, J. Jin, J.A. Slater, D. Oblak, F. Bussières, M. George, R. Ricken, W. Sohler, and W. Tittel. Broadband waveguide quantum memory for entangled photons. *Nature*, 469(7331), January 2011. (cited on pages 6, 36, 38, and 45)

[17] E. Saglamyurek, N. Sinclair, J. A. Slater, K. Heshami, D. Oblak, and W. Tittel. An integrated processor for photonic quantum states using a broadband lightmatter interface. *New Journal of Physics*, 16(6), June 2014. (cited on page 6)

[18] J.E. Geusic, H.M. Marcos, and L.G. Van Uitert. Laser oscillations in nddoped yttrium aluminum, yttrium gallium and gadolinium garnets. *Applied Physics Letters*, 4(10):182–184, 1964. (cited on page 6)

[19] S.R. Hastings-Simon, M.U. Staudt, M. Afzelius, P. Baldi, D. Jaccard, W. Tittel, and N. Gisin. Controlled Stark shifts in Er^{3+}-doped crystalline and amorphous waveguides for quantum state storage. *Optics Communications*, 266(2), October 2006. (cited on page 6)

[20] N. Sinclair, E. Saglamyurek, M. George, R. Ricken, C. La Mela, W. Sohler, and W. Tittel. Spectroscopic investigations of a Ti:Tm:$LiNbO_3$ waveguide for photon-echo quantum memory. *Journal of Luminescence*, 130(9):1586–1593, September 2010. (cited on pages 6 and 36)

[21] G. P. Flinn, K.W. Jang, J. Ganem, M.L. Jones, R.S. Meltzer, and R.M. Macfarlane. Anomalous optical dephasing in crystalline Y_2O_3:Eu^{3+}. *Journal of Luminescence*, 58(1-6), January 1994. (cited on pages 7 and 36)

[22] R.M. Macfarlane and R.M. Shelby. Sub-kilohertz optical linewidths of the $^7F_0 \leftrightarrow {}^5D_0$ transition in Y_2O_3: Eu^{3+}. *Optics Communications*, 39(3), 1981. (cited on pages 7, 36, and 63)

[23] J. Paulraj. *Ongoing project*. PhD thesis, Australian National University. (cited on pages 7, 33, 61, 62, 65, 66, 67, and 68)

[24] S.J. Madden and K.T. Vu. Very low loss reactively ion etched tellurium dioxide planar rib waveguides for linear and non-linear optics. *Opt. Express*, 17(20), Sep 2009. (cited on pages 8, 52, 72, 73, and 127)

[25] R.L. Ahlefeldt, M.R. Hush, and M.J. Sellars. Ultranarrow optical inhomogeneous linewidth in a stoichiometric rare-earth crystal. *Phys. Rev. Lett.*, 117:250504, Dec 2016. (cited on pages 8, 20, 53, and 54)

[26] M.P. Hedges, J.J. Longdell, Y. Li, and M.J. Sellars. Efficient quantum memory for light. *Nature*, 465(7301):1052–1056, June 2010. (cited on pages 8, 38, 39, 43, 53, 54, 70, 92, 94, and 96)

[27] S.E. Beavan, M.P. Hedges, and M.J. Sellars. Demonstration of Photon-Echo Rephasing of Spontaneous Emission. *Physical Review Letters*, 109(9):093603, August 2012. (cited on pages 8 and 39)

[28] S.E. Beavan, E.A. Goldschmidt, and M.J. Sellars. Demonstration of a dynamic bandpass frequency filter in a rare-earth ion-doped crystal. *Journal of the Optical Society of America B*, 30(5), April 2013. (cited on pages 8, 54, and 70)

[29] P.M. Ledingham, W.R. Naylor, and J.J. Longdell. Experimental realization of light with time-separated correlations by rephasing amplified spontaneous emission. *Phys. Rev. Lett.*, 109:093602, Aug 2012. (cited on pages 8 and 39)

[30] P.M. Ledingham, W.R. Naylor, J.J. Longdell, S.E. Beavan, and M.J. Sellars. Nonclassical photon streams using rephased amplified spontaneous emission. *Physical Review A*, 81(1):1–5, January 2010. (cited on pages 8, 39, 43, and 44)

[31] Rare earth elements. http://www.periodni.com/rare_earth_elements.html. (cited on page 11)

[32] G. F. Imbusch and R. Kopelman. *Optical Spectroscopy of Electronic Centers*

in Solids, pages 1–37. Springer Berlin Heidelberg, Berlin, Heidelberg, 1981. (cited on page 12)

[33] A.J. Freeman and R.E. Watson. Theoretical investigation of some magnetic and spectroscopic properties of rare-earth ions. *Phys. Rev.*, 127:2058–2075, Sep 1962. (cited on page 13)

[34] R.M. Macfarlane and R.M. Shelby. Coherent transient and holeburning spectroscopy of rare earth ions in solids. In A. A. Kaplyanskii and R. M. Macfarlane, editors, *Spectroscopy of Solids Containing Rare Earth Ions*. North-Holland, 1987. (cited on pages 13 and 14)

[35] G. Liu. Electronic energy level structure. In G. Liu and B. Jacquier, editors, *Spectroscopic Properties of Rare Earths in Optical Materials*. Springer Berlin Heidelberg, 2005. (cited on pages 13, 14, and 21)

[36] M.A. Teplov. Magnetic resonance on Pr^{141} nuclei in a $Pr_2(SO_4)_3.8H_2O$ single crystal. *Soviet Physics Uspekhi*, 26(5):872–875, 1968. (cited on page 15)

[37] R.M. Macfarlane. Optical stark spectroscopy of solids. *Journal of Luminescence*, 125(12):156 – 174, 2007. Festschrift in Honor of Academician Alexander A. Kaplyanskii. (cited on page 16)

[38] H. Lin, T. Wang, and T. W. Mossberg. Demonstration of 8-gbit/in.^{2} areal storage density based on swept-carrier frequency-selective optical memory. *Opt. Lett.*, 20(15):1658–1660, Aug 1995. (cited on page 16)

[39] T.L. Harris, Y. Sun, R.L. Cone, R.M. Macfarlane, and R.W. Equall. Demonstration of real-time address header decoding for optical data routing at 1536 nm. *Opt. Lett.*, 23(8):636–638, Apr 1998. (cited on page 16)

[40] T.L. Harris, Y. Sun, W.R. Babbitt, R.L. Cone, J.A. Ritcey, and R.W. Equall. Spatial-spectral holographic correlator at 1536 nm using 30-symbol quadriphase- and binary-phase-shift keyed codes. *Opt. Lett.*, 25(2):85–87, Jan 2000. (cited on page 16)

[41] Z. Cole, T. Böttger, R. Krishna Mohan, R. Reibel, W.R. Babbitt, R.L. Cone, and K.D. Merkel. Coherent integration of 0.5 ghz spectral holograms at 1536 nm using dynamic biphase codes. *Applied Physics Letters*, 81(19):3525–3527, 2002. (cited on page 16)

[42] V. Crozatier, G. Gorju, J.-L. Le Gouët, F. Bretenaker, and I. Lorgeré. Wideband and high-resolution coherent optical transients with a frequency-agile laser oscillator. *Opt. Lett.*, 31(22):3264–3266, Nov 2006. (cited on page 16)

[43] F. Schlottau and K.V. Wagner. Demonstration of a continuous scanner and time-integrating correlator using spatialspectral holography. *Journal of Luminescence*, 107(14):90 – 102, 2004. Proceedings of the 8th International Meeting on Hole Burning, Single Molecule, and Related Spectroscopies: Science and Applications. (cited on page 16)

[44] K.D. Merkel, R. Krishna Mohan, Z. Cole, T. Chang, A. Olson, and W.R. Babbitt. Multi-gigahertz radar range processing of baseband and {RF} carrier modulated signals in tm:yag. *Journal of Luminescence*, 107(14):62 – 74, 2004. Proceedings of the 8th International Meeting on Hole Burning, Single Molecule, and Related Spectroscopies: Science and Applications. (cited on page 16)

[45] P. F. Bernath. *Spectra of atoms and molecules (2 Ed.)*. Oxford University Press Inc., New York, 2005. (cited on page 17)

[46] R.M. Macfarlane, C.S. Yannoni, and R.M. Shelby. Optical line narrowing by nuclear spin decoupling in Pr^{3+}:LaF_3. *Optics Communications*, 32(1):101–104, January 1980. (cited on page 18)

[47] D.L. McAuslan, J.G. Bartholomew, M.J. Sellars, and J.J. Longdell. Reducing decoherence in optical and spin transitions in rare-earth-metal-ion-doped materials. *Physical Review A*, 85(3):032339, mar 2012. (cited on page 18)

[48] E. Fraval, M.J. Sellars, and J.J. Longdell. Method of Extending Hyperfine Coherence Times in Pr^{3+}:Y_2SiO_5. *Physical Review Letters*, 92(7):5–8, February 2004. (cited on pages 18, 70, and 72)

[49] J.J. Longdell, A.L. Alexander, and M.J. Sellars. Characterization of the hyperfine interaction in europium-doped yttrium orthosilicate and europium chloride hexahydrate. *Physical Review B*, 74(19):1–7, 2006. (cited on pages 18, 22, and 72)

[50] A.L. Alexander, J.J. Longdell, and M.J. Sellars. Measurement of the ground-state hyperfine coherence time of $^{151}Eu^{3+}$:Y_2SiO_5. *Journal of the Optical Society of America B*, 24(9):2479, 2007. (cited on page 18)

[51] R.L. Ahlefeldt, M. Zhong, J.G. Bartholomew, and M.J. Sellars. Minimizing Zeeman sensitivity on optical and hyperfine transitions in $EuCl_3$. $6H_2O$ to extend coherence times. *Journal of Luminescence*, 143:193–200, nov 2013. (cited on page 18)

[52] L. Viola, E. Knill, and S. Lloyd. Dynamical Decoupling of Open Quantum

Systems. *Physical Review Letters*, 82(12):2417–2421, mar 1999. (cited on page 18)

[53] E. Fraval, M.J. Sellars, and J.J. Longdell. Dynamic decoherence control of a solid-state nuclear-quadrupole qubit. *Physical Review Letters*, 95(3):8–11, 2005. (cited on pages 18 and 72)

[54] G. Heinze, C. Hubrich, and T. Halfmann. Stopped light and image storage by electromagnetically induced transparency up to the regime of one minute. *Physical Review Letters*, 111(3):033601, jul 2013. (cited on pages 18 and 38)

[55] S.E. Beavan, E. Fraval, M.J. Sellars, and J.J. Longdell. Demonstration of the reduction of decoherent errors in a solid-state qubit using dynamic decoupling techniques. *Physical Review A*, 80(3):032308, September 2009. (cited on page 18)

[56] G.A. Alvarez, A. Ajoy, X. Peng, and D. Suter. Performance comparison of dynamical decoupling sequences for a qubit in a rapidly fluctuating spin bath. *Physical Review A*, 82(4):042306, October 2010. (cited on page 18)

[57] A.M. Souza, G.A. Alvarez, and D. Suter. Robust dynamical decoupling for quantum computing and quantum memory. *Physical Review Letters*, 106(24):240501, jun 2011. (cited on page 18)

[58] R. S. Meltzer. Line broadening mechanisms and their measurement. In G. Liu and B. Jacquier, editors, *Spectroscopic Properties of Rare Earths in Optical Materials*. Springer Berlin Heidelberg, 2005. (cited on pages 18 and 19)

[59] J.G. Bartholomew. *Investigation of the scalability of rare-earth-ion quantum hardware*. PhD thesis, Australian National University, 2014. (cited on pages 18, 20, 70, 71, and 127)

[60] H. Bernien, B. Hensen, W. Pfaff, G. Koolstra, M.S. Blok, L. Robledo, Ti.H. Taminiau, M. Markham, D. J. Twitchen, L. Childress, and R. Hanson. Heralded entanglement between solid-state qubits separated by three metres. *Nature*, 497(7447):86–90, May 2013. (cited on pages 19 and 38)

[61] F.R. Graf, A. Renn, G. Zumofen, and U.P. Wild. Photon-echo attenuation by dynamical processes in rare-earth-ion-doped crystals. *Phys. Rev. B*, 58:5462–5478, Sep 1998. (cited on page 19)

[62] R. M. Macfarlane, R. S. Meltzer, and B. Z. Malkin. Optical measurement of the isotope shifts and hyperfine and superhyperfine interactions of Nd in the solid state. *Physical Review B*, 58(9):5692–5700, 1998. (cited on page 20)

[63] R.M. Macfarlane and R.M. Shelby. Magnetic field dependent optical dephasing in LaF_3:Er^{3+}. *Optics Communications*, 42(5):346 – 350, 1982. (cited on page 20)

[64] R. Wannemacher, R.S. Meltzer, and R.M. Macfarlane. Time-resolved spectral holeburning in LaF_3:Ho^{3+} and $YLiF_4$:Er^{3+} . *Journal of Luminescence*, 45(16):307 – 309, 1990. (cited on page 20)

[65] J. Ganem, Y. P. Wang, D. Boye, R. S. Meltzer, W. M. Yen, and R. M. Macfarlane. Nonexponential photon-echo decays of paramagnetic ions in the superhyperfine limit. *Phys. Rev. Lett.*, 66:695–698, Feb 1991. (cited on pages 20 and 34)

[66] R. Yano, M. Mitsunaga, and N. Uesugi. Stimulated-photon-echo spectroscopy. I. Spectral diffusion in Eu^{3+}:$YAlO_3$. *Phys. Rev. B*, 45:12752–12759, Jun 1992. (cited on page 20)

[67] G. Liu and B. Jacquier. *Spectroscopic Properties of Rare Earths in Optical Materials*. Springer, 2005. (cited on page 20)

[68] F. Könz, Y. Sun, C.W. Thiel, R.L. Cone, R.W. Equall, R.L. Hutcheson, and R.M. Macfarlane. Temperature and concentration dependence of optical dephasing, spectral-hole lifetime, and anisotropic absorption in Eu^{3+}:Y_2SiO_5. *Physical Review B*, 68(8):1–9, 2003. (cited on pages 21, 35, and 126)

[69] K. Holliday, M. Croci, E. Vauthey, and U.P. Wild. *Physical Review B*, 47(22), June 1993. (cited on pages 21, 71, 72, 103, and 118)

[70] E. Fraval. *Minimising the Decoherence of Rare Earth Ion Solid State Spin Qubits*. PhD thesis, Australian National University, 2005. (cited on page 21)

[71] R.M. Macfarlane, D.P. Burum, and R.M. Shelby. New determination of the nuclear magnetic moment of ^{141}Pr. *Phys. Rev. Lett.*, 49:636–639, Aug 1982. (cited on page 21)

[72] Dr. W. E. Moerner. *Persistent Spectral Hole-Burning: Science and Applications*. Springer Berlin Heidelberg, 1988. (cited on page 22)

[73] N.A. Kurnit, I.D. Abella, and S.R. Hartmann. Observation of a photon echo. *Physical Review Letters*, 13(19):567–568, 1964. (cited on pages 23 and 28)

[74] R.G. Brewer and R.L. Shoemaker. Optical free induction decay. *Phys. Rev. A*, 6:2001–2007, Dec 1972. (cited on pages 23, 27, 28, and 54)

[75] D. Allen and J.H. Eberly. *Optical resonace and two-level atoms.* Wiley, New York, 1975. (cited on page 24)

[76] R.W. Boyd. *Nonlinear optics.* Academic press limited, London, England, 1992. (cited on page 24)

[77] R.L. Shoemaker. *Coherent Transient Infrared Spectroscopy, in Laser and Coherence Spectroscopy.* Steinfeld, J. I. (Ed.), Plenum Press, New York, 1978. (cited on pages 24 and 27)

[78] R.M. Macfarlane and R.M. Shelby. *Spectroscopy of solids containing rare earth ions.* North-Holland, Amsterdam, 1987. (cited on page 27)

[79] R.M. Macfarlane. High-resolution laser spectroscopy of rare-earth doped insulators: a personal perspective. *Journal of Luminescence*, 100(14):1 – 20, 2002. (cited on page 28)

[80] E.L. Hahn. Spin echoes. *Phys. Rev.*, 80:580–594, Nov 1950. (cited on page 28)

[81] T.W. Mossberg, R. Kachru, S.R. Hartmann, and A.M. Flusberg. Echoes in gaseous media: A generalized theory of rephasing phenomena. *Phys. Rev. A*, 20:1976–1996, Nov 1979. (cited on page 28)

[82] R. Beach, S.R. Hartmann, and R. Friedberg. Billiard-ball echo model. *Phys. Rev. A*, 25:2658–2666, May 1982. (cited on page 28)

[83] M. Mitsunaga and R.G. Brewer. Generalized perturbation theory of coherent optical emission. *Phys. Rev. A*, 32:1605–1613, Sep 1985. (cited on page 28)

[84] A.V. Durrant, J. Manners, and P.M. Clark. Understanding optical echoes using schrodinger's equation: Ii. three pulse echoes and collision effects. *European Journal of Physics*, 12(5):234, 1991. (cited on page 28)

[85] T.W. Mossberg. Time-domain frequency-selective optical data storage. *Opt. Lett.*, 7(2):77–79, Feb 1982. (cited on page 31)

[86] Y.S. Bai, W.R. Babbitt, N.W. Carlson, and T.W. Mossberg. Realtime optical waveform convolver/cross correlator. *Applied Physics Letters*, 45(7):714–716, 1984. (cited on page 31)

[87] T.W. Mossberg. Swept-carrier time-domain optical memory. *Opt.Lett.*, 17:535–537, 1992. (cited on page 31)

[88] M.J. Sellars, R.S. Meltzer, P.T.H. Fisk, and N.B. Manson. Time-resolved

ultranarrow optical hole burning of a crystalline solid, Y_2O_3:Eu^{+3} . *J. Opt. Soc. Am. B*, 11(8):1468–1473, Aug 1994. (cited on pages 32, 33, and 63)

[89] R.S. Meltzer and K.S. Hong. Electron-phonon interactions in insulating nanoparticles: Eu_2O_3. *Physical Review B*, 61(5):3396–3403, 2000. (cited on page 33)

[90] G. Malovichko, V. Grachev, and O. Schirmer. Interrelation of intrinsic and extrinsic defects – congruent, stoichiometric, and regularly ordered lithium niobate. *Applied Physics B*, 68(5):785–793, 1999. (cited on page 34)

[91] V. Dierolf and M. Koerdt. Combined excitation-emission spectroscopy of er^{3+} ions in stoichiometric $linbo_3$: the site selectivity of direct and up conversion excitation processes. *Phys. Rev. B*, 61:8043–8052, Mar 2000. (cited on page 34)

[92] C.W. Thiel, Y. Sun, T. Böttger, W.R. Babbitt, and R.L. Cone. Optical decoherence and persistent spectral hole burning in Tm^{3+}:$LiNbO_3$. *Journal of Luminescence*, 130(9):1598–1602, September 2010. (cited on pages 34 and 36)

[93] Y. Sun, C.W. Thiel, and R.L. Cone. Optical decoherence and energy level structure of 0.1%Tm^{3+}:$LiNbO_3$. *Phys. Rev. B*, 85:165106, Apr 2012. (cited on page 34)

[94] C.W. Thiel, Y. Sun, R.M. Macfarlane, T. Böttger, and R.L. Cone. Rare-earth-doped $LiNbO_3$ and $KTiOPO_4$ (KTP) for waveguide quantum memories. *Journal of Physics B: Atomic, Molecular and Optical Physics*, 45(12), jun 2012. (cited on page 34)

[95] R.M. Macfarlane, F. Knz, Y. Sun, and R.L. Cone. Spectral hole burning and optical dephasing in disordered crystals Pr^{3+} : $LiNbO_3$ and Pr^{3+} : $Sr_{.6}Ba_{.4}Nb_2O_6$ (SBN) . *Journal of Luminescence*, 86(34):311 – 315, 2000. (cited on page 34)

[96] S.K. Watson. Tunneling states in crystals with large random strains. *Phys. Rev. Lett.*, 75:1965–1968, Sep 1995. (cited on page 34)

[97] R.M. Macfarlane, Y. Sun, R.L. Cone, C.W. Thiel, and R.W. Equall. Optical dephasing by disorder modes in yttrium orthosilicate (Y_2SiO_5) doped with Eu^{3+} . *Journal of Luminescence*, 107(14):310 – 313, 2004. Proceedings of the 8th International Meeting on Hole Burning, Single Molecule, and Related Spectroscopies: Science and Applications. (cited on page 34)

[98] A. Szabo, T. Muramoto, and R. Kaarli. ^{27}Al nuclear-spin dephasing in the

ruby frozen core and Cr^{3+} spin-flip-time measurements. *Phys. Rev. B*, 42:7769–7776, Nov 1990. (cited on page 34)

[99] R. Yano, M. Mitsunaga, and N. Uesugi. Nonlinear laser spectroscopy of Eu^{3+}:Y_2SiO_5 and its application to time-domain optical memory. *Journal of the Optical Society of America B*, 9(6):992, June 1992. (cited on page 34)

[100] J. G. Bartholomew. *Development of Coherent Spectroscopic Techniques to Characterise Near Surface Rare Earth Ions in Crystalline Hosts*. Honours thesis, Australian National University, 2007. (cited on pages 35, 98, and 99)

[101] D.L. McAuslan, D. Korystov, and J.J. Longdell. Coherent spectroscopy of rare-earth-metal-ion-doped whispering-gallery-mode resonators. *Physical Review A*, 83(6):063847, June 2011. (cited on page 35)

[102] M.B. Korzenski, Ph. Lecoeur, B. Mercey, P. Camy, and J.-L. Doualan. Low propagation losses of an Er:Y_2O_3 planar waveguide grown by alternate-target pulsed laser deposition. *Applied Physics Letters*, 78(9):1210, 2001. (cited on page 36)

[103] R.M. Macfarlane and R.M. Shelby. Homogeneous line broadening of optical transitions of ions and molecules in glasses. *Journal of Luminescence*, 36:179–207, 1987. (cited on pages 36 and 126)

[104] N Sinclair, D Oblak, C.W. Thiel, R.L. Cone, and W. Tittel. A rare-earth-ion-doped waveguide based on a standard photonics technology for quantum signal processing. *arXiv*, 2016. (cited on pages 36 and 45)

[105] S. Marzban, J.G. Bartholomew, S. Madden, K. Vu, and M.J. Sellars. Observation of photon echoes from evanescently coupled rare-earth ions in a planar waveguide. *Phys. Rev. Lett.*, 115:013601, Jul 2015. (cited on pages 37 and 126)

[106] T. Zhong, J.M. Kindem, E. Miyazono, and A. Faraon. Nanophotonic coherent lightmatter interfaces based on rare-earth-doped crystals. *Nature Communications*, Sept 2015. (cited on page 37)

[107] G. Corrielli, A. Seri, M. Mazzera, R. Osellame, and H. de Riedmatten. Integrated optical memory based on laser-written waveguides. *Phys. Rev. Applied*, 5:054013, May 2016. (cited on pages 37 and 45)

[108] H.P. Specht, C. Nlleke, A. Reiserer, M. Uphoff, E. Figueroa, S. Ritter, and G. Rempe. A single-atom quantum memory. *Nature*, (473):190–193, 2015. (cited on page 38)

[109] T. Chanelire, D.N. Matsukevich, S.D. Jenkins, S.Y. Lan, T.A. Kennedy, and A. Kuzmich. Storage and retrieval of single photons transmitted between remote quantum memories. *Nature*, (43):833–836, 2015. (cited on page 38)

[110] M. Afzelius, C. Simon, H. de Riedmatten, and N. Gisin. Multimode quantum memory based on atomic frequency combs. *Physical Review A*, 79(5):1–9, May 2009. (cited on pages 38, 39, and 40)

[111] K.R. Ferguson, S.E. Beavan, J.J. Longdell, and M.J. Sellars. Generation of light with multimode time-delayed entanglement using storage in a solid-state spin-wave quantum memory. *Phys. Rev. Lett.*, 117:020501, Jul 2016. (cited on pages 38, 39, 45, and 56)

[112] M. Steger, K. Saeedi, M.L.W. Thewalt, J.J.L. Morton, H. Riemann, N.V. Abrosimov, P. Becker, and H.-J. Pohl. Quantum information storage for over 180 s using donor spins in a ^{28}si "semiconductor vacuum". *Science*, 336(6086):1280–1283, 2012. (cited on page 38)

[113] P.C. Maurer, G. Kucsko, C. Latta, L. Jiang, N.Y. Yao, S.D. Bennett, F. Pastawski, D. Hunger, N. Chisholm, M. Markham, D.J. Twitchen, J.I. Cirac, and M.D. Lukin. Room-temperature quantum bit memory exceeding one second. *Science*, 336(6086):1283–1286, 2012. (cited on page 38)

[114] K. Saeedi, S. Simmons, J.Z. Salvail, P. Dluhy, H. Riemann, N.V. Abrosimov, P. Becker, H.J. Pohl, J.J. L. Morton, and M.L.W. Thewalt. Room-temperature quantum bit storage exceeding 39 minutes using ionized donors in silicon-28. *Science*, 342(6160):830–833, 2013. (cited on page 38)

[115] Y.H. Chen, M.J. Lee, I.C. Wang, S. Du, Y.F. Chen, Y.C. Chen, and I.A. Yu. Coherent optical memory with high storage efficiency and large fractional delay. *Phys. Rev. Lett.*, 110:083601, Feb 2013. (cited on page 38)

[116] E. Bimbard, R. Boddeda, N. Vitrant, A. Grankin, V. Parigi, J. Stanojevic, A. Ourjoumtsev, and P. Grangier. Homodyne tomography of a single photon retrieved on demand from a cavity-enhanced cold atom memory. *Phys. Rev. Lett.*, 112:033601, Jan 2014. (cited on pages 38 and 45)

[117] N. Sinclair, E. Saglamyurek, H. Mallahzadeh, J. A. Slater, M. George, R. Ricken, M. P. Hedges, D. Oblak, C. Simon, W. Sohler, and W. Tittel. Spectral multiplexing for scalable quantum photonics using an atomic frequency comb quantum memory and feed-forward control. *Phys. Rev. Lett.*, 113:053603, Jul 2014. (cited on pages 38, 39, and 45)

[118] C. Clausen, I. Usmani, F. Bussières, N. Sangouard, M. Afzelius, H. de Riedmatten, and N. Gisin. Quantum storage of photonic entanglement in a crystal. *Nature*, 469(7331):508–11, January 2011. (cited on page 38)

[119] I. Usmani, C. Clausen, F. Bussieres, N. Sangouard, M. Afzelius, and N. Gisin. Heralded quantum entanglement between two crystals. *Nature Photonics*, 6, April 2012. (cited on page 38)

[120] W. Pfaff, B.J. Hensen, H. Bernien, S. B. van Dam, M.S. Blok, T.H. Taminiau, M.J. Tiggelman, R.N. Schouten, M. Markham, D.J. Twitchen, and R. Hanson. Unconditional quantum teleportation between distant solid-state quantum bits. *Science*, 345(6196):532–535, 2014. (cited on page 38)

[121] B. Kraus, W. Tittel, N. Gisin, M. Nilsson, S. Kröll, and J. I. Cirac. Quantum memory for nonstationary light fields based on controlled reversible inhomogeneous broadening. *Physical Review A*, 73(2):1–4, February 2006. (cited on pages 39 and 41)

[122] N. Sangouard, C. Simon, M. Afzelius, and N. Gisin. Analysis of a quantum memory for photons based on controlled reversible inhomogeneous broadening. *Physical Review A*, 75(3):1–8, March 2007. (cited on page 39)

[123] J.J. Longdell, G. Hétet, P.K. Lam, and M.J. Sellars. Analytic treatment of controlled reversible inhomogeneous broadening quantum memories for light using two-level atoms. *Physical Review A*, 78(3):1–6, September 2008. (cited on page 39)

[124] D. L. McAuslan, P. M. Ledingham, W. R. Naylor, S. E. Beavan, M. P. Hedges, M. J. Sellars, and J. J. Longdell. Photon-echo quantum memories in inhomogeneously broadened two-level atoms. *Phys. Rev. A*, 84:022309, Aug 2011. (cited on page 39)

[125] V. Damon, M. Bonarota, A. Louchet-Chauvet, T. Chanelire, and J.L. Le Gout. Revival of silenced echo and quantum memory for light. *New Journal of Physics*, 13(9):093031, 2011. (cited on page 39)

[126] Yan Fu, Ming-Feng Wang, and Yi-Zhuang Zheng. Cavity-assisted revival of silenced echo quantum memory. *Optics Communications*, 321:162 – 166, 2014. (cited on page 39)

[127] M. Afzelius, I. Usmani, A. Amari, B. Lauritzen, A. Walther, C. Simon, N. Sangouard, J. Minář, H. de Riedmatten, N. Gisin, and S. Kröll. Demonstration of

Atomic Frequency Comb Memory for Light with Spin-Wave Storage. *Physical Review Letters*, 104(4):040503, January 2010. (cited on pages 39 and 40)

[128] T. Chanelire, J. Ruggiero, M. Bonarota, M. Afzelius, and J.L. Le Gout. Efficient light storage in a crystal using an atomic frequency comb. *New Journal of Physics*, 12, Feb 2010. (cited on page 39)

[129] W.H. Hesselink and D.A. Wiersma. Picosecond photon echoes stimulated from an accumulated grating. *Phys. Rev. Lett.*, 43:1991–1994, Dec 1979. (cited on page 40)

[130] A. Rebane, R. Kaarli, P. Saari, A. Anijalg, and K. Timpmann. Photochemical time-domain holography of weak picosecond pulses. *Optics Communications*, 47(3):173 – 176, 1983. (cited on page 40)

[131] M. Mitsunaga, R. Yano, and N. Uesugi. Spectrally programmed stimulated photon echo. *Optics Letters*, 16:264–266, 1991. (cited on page 40)

[132] M. Gündoğan, P.M. Ledingham, K. Kutluer, M. Mazzera, and H. de Riedmatten. Solid state spin-wave quantum memory for time-bin qubits. *Phys. Rev. Lett.*, 114:230501, Jun 2015. (cited on page 40)

[133] W. Tittel, M. Afzelius, T. Chanelire, R.L. Cone, S. Krll, S.A. Moiseev, and M.J. Sellars. Photon-echo quantum memory in solid state systems. *Laser & Photon. Rev.*, 4:244–267, 2010. (cited on page 41)

[134] G. Hétet, J.J. Longdell, M.J. Sellars, P.K. Lam, and B.C. Buchler. Multimodal properties and dynamics of gradient echo quantum memory. *Phys. Rev. Lett.*, 101:203601, Nov 2008. (cited on page 41)

[135] A.L. Alexander, J.J. Longdell, M.J. Sellars, and N.B. Manson. Photon echoes produced by switching electric fields. *Phys. Rev. Lett.*, 96:043602, Feb 2006. (cited on page 42)

[136] A.L. Alexander, J.J. Longdell, M.J. Sellars, and N.B. Manson. Coherent information storage with photon echoes produced by switching electric fields. *Journal of Luminescence*, 127(1):94 – 97, 2007. Proceedings of the Ninth International Meeting on Hole Burning, Single Molecule, and Related Spectroscopies: Science and Applications Hole Burning, Single Molecule, and Related Spectroscopies: Science and Applications. (cited on page 43)

[137] G. Hétet, J.J. Longdell, A.L. Alexander, P.K. Lam, and M.J. Sellars. Electro-optic quantum memory for light using two-level atoms. *Phys. Rev. Lett.*, 100:023601, Jan 2008. (cited on page 43)

[138] B. Lauritzen, J. Minář, H. de Riedmatten, M. Afzelius, N. Sangouard, C. Simon, and N. Gisin. Telecommunication-Wavelength Solid-State Memory at the Single Photon Level. *Physical Review Letters*, 104(8):1–4, February 2010. (cited on page 43)

[139] K.R. Ferguson. *Generation and storage of optical entanglement in a solid state spin-wave quantum memory*. PhD thesis, Australian National University, 2016. (cited on pages 44 and 56)

[140] M. Steger, K. Saeedi, M. L. W. Thewalt, J. J. L. Morton, H. Riemann, N. V. Abrosimov, P. Becker, and H.-J. Pohl. Quantum information storage for over 180 s using donor spins in a ^{28}Si Semiconductor Vacuum. *Science*, 336(6086):1280–3, June 2012. (cited on page 45)

[141] K. Saeedi, S. Simmons, J. Z. Salvail, P. Dluhy, H. Riemann, N. V. Abrosimov, P. Becker, H.-J. Pohl, J. J. L. Morton, and M. L. W. Thewalt. Room-temperature quantum bit storage exceeding 39 minutes using ionized donors in silicon-28. *Science (New York, N.Y.)*, 342(6160):830–3, November 2013. (cited on page 45)

[142] M. Sabooni, Q. Li, S. Kröll, and L. Rippe. Efficient quantum memory using a weakly absorbing sample. *Phys. Rev. Lett.*, 110:133604, Mar 2013. (cited on page 45)

[143] S. Probst, A. Tkalčec, H. Rotzinger, D. Rieger, J-M. Le Floch, M. Goryachev, M. E. Tobar, A. V. Ustinov, and P. A. Bushev. Three-dimensional cavity quantum electrodynamics with a rare-earth spin ensemble. *Phys. Rev. B*, 90:100404, Sep 2014. (cited on page 46)

[144] E. Knill, R. Laflamme, and G.J. Milburn. A scheme for efficient quantum computation with linear optics. *Nature*, Nov 2000. (cited on page 49)

[145] P. Kok, W. J. Munro, K. Nemoto, T. C. Ralph, J.P. Dowling, and G. J. Milburn. Linear optical quantum computing with photonic qubits. *Rev. Mod. Phys.*, 79:135–174, Jan 2007. (cited on page 49)

[146] J. Carolan, C. Harrold, C. Sparrow, E. Martín-López, N.J. Russell, J.W. Silverstone, P.J. Shadbolt, N. Matsuda, M. Oguma, M. Itoh, G.D. Marshall, M.G. Thompson, J.C.F. Matthews, T. Hashimoto, J.L. O'Brien, and A. Laing. Universal linear optics. *Science*, 349(6249):711–716, 2015. (cited on page 50)

[147] K. Vu and S. Madden. Tellurium dioxide erbium doped planar rib waveg-

uide amplifiers with net gain and 2.8db/cm internal gain. *Opt. Express*, 18(18):19192–19200, Aug 2010. (cited on page 52)

[148] S. Shen, A. Jha, X. Liu, M. Naftaly, K. Bindra, H.J. Bookey, and A.K. Kar. Tellurite glasses for broadband amplifiers and integrated optics. *Journal of the American Ceramic Society*, 85(6):1391–1395, 2002. (cited on page 52)

[149] S. Madden, Z. Jin, D. Choi, S. Debbarma, D. Bulla, and B. Luther-Davies. Low loss coupling to sub-micron thick rib and nanowire waveguides by vertical tapering. *Opt. Express*, 21(3):3582–3594, Feb 2013. (cited on page 52)

[150] M. Razavi, M. Piani, and N. Lütkenhaus. Quantum repeaters with imperfect memories: Cost and scalability. *Phys. Rev. A*, 80:032301, Sep 2009. (cited on page 53)

[151] D.C. Burnham and D.L. Weinberg. Observation of simultaneity in parametric production of optical photon pairs. *Phys. Rev. Lett.*, 25:84–87, Jul 1970. (cited on page 55)

[152] C. K. Hong and L. Mandel. Theory of parametric frequency down conversion of light. *Phys. Rev. A*, 31:2409–2418, Apr 1985. (cited on page 55)

[153] C.K. Hong, Z.Y. Ou, and L. Mandel. Measurement of subpicosecond time intervals between two photons by interference. *Phys. Rev. Lett.*, 59:2044–2046, Nov 1987. (cited on page 55)

[154] S.E. Beavan. *Photon-echo rephasing of spontaneous emission from an ensemble of rare-earth ions*. PhD thesis, Australian National University, 2012. (cited on pages 56, 99, 102, and 125)

[155] S. Manning. *A study of tellurite glasses for electro-optic optical fibre devices*. PhD thesis, University of Adelaide, School of Chemistry and Physics, 2011. (cited on page 58)

[156] L. Redaelli, G. Bulgarini, S. Dobrovolskiy, S.N. Dorenbos, V. Zwiller, E. Monroy, and J.M. Grard. Design of broadband high-efficiency superconducting-nanowire single photon detectors. *Superconductor Science and Technology*, 29(6):065016, 2016. (cited on page 59)

[157] S. Bär, G. Huber, J. Gonzalo, A. Perea, and M. Munz. Pulsed laser deposition of Eu:Y_2O_3 thin films on (0001) α-Al_2O_3. *Applied Physics A*, 80(2):209–216, September 2004. (cited on pages 63, 64, 66, and 68)

[158] W. R. Babbitt, A. Lezama, and T. W. Mossberg. Optical dephasing, hyperfine

structure, and hyperfine relaxation associated with the 580.8-nm $^7F_0$–$^5D_0$ transition of europium in Eu^{3+}:Y_2O_3. *Phys. Rev. B*, 39:1987–1992, Feb 1989. (cited on page 63)

[159] R. Eason. *Pulsed Laser Deposition of Thin Films: Applications-Led Growth of Functional Materials*. Wiley, 2006. (cited on page 64)

[160] S. Bär. *Crystalline, Rare-Earth-doped Sesquioxide PLD-Films on α-Alumina*. Phd thesis, University of Hamburg, 2004. (cited on page 67)

[161] F. R Graf. *Investigations of spectral dynamics in rare earth ion doped crystals using high resolution laser techniques*. PhD thesis, Diss. Naturwiss. ETH Zürich, Nr. 12623, 1998. Ref.: Urs P. Wild; Korref.: Richard R. Ernst, 1998. (cited on page 69)

[162] X-ray Structure Determination of $Tm : Y_2SiO_5$. Technical report, Scientific Materials Corp., Bozeman, MT, 1995. (cited on page 69)

[163] Z. Sun, J. Wang, M. Li, and Y. Zhou. Mechanical properties and damage tolerance of $\{Y_2SiO_5\}$. *Journal of the European Ceramic Society*, 28(15):2895 – 2901, 2008. (cited on page 69)

[164] Y. C. Sun. Rare earth materials in optical storage and data processing applications. In G. Liu and B. Jacquier, editors, *Spectroscopic Properties of Rare Earths in Optical Materials*. Springer Berlin Heidelberg, 2005. (cited on page 70)

[165] C. Li, C. Wyon, and R. Moncorge. Spectroscopic properties and fluorescence dynamics of Er^{3+} and Yb^{3+} in Y_2SiO_5. *IEEE Journal of Quantum Electronics*, 28(4):1209–1221, April 1992. (cited on page 70)

[166] J.J. Longdell, E. Fraval, M.J. Sellars, and N.B. Manson. Stopped Light with Storage Times Greater than One Second Using Electromagnetically Induced Transparency in a Solid. *Physical Review Letters*, 95(6):2–5, August 2005. (cited on page 70)

[167] G. H. Dieke, H. M. Crosswhite, and B. Dunn. Emission Spectra of the Doubly and Triply Ionized Rare Earths. *Journal of the Optical Society of America*, 51(8):820, August 1961. (cited on pages 70 and 71)

[168] M. Nilsson, L. Rippe, and S. Kröll. Hole-burning techniques for isolation and study of individual hyperfine transitions in inhomogeneously broadened solids demonstrated in Pr^{3+}:Y_2SiO_5. *Physical Review B*, 70(21), December 2004. (cited on pages 70 and 71)

[169] K.T. Vu. *Fabrication and characterisation of nonlinear tellurite planar waveguides*. PhD thesis, Australian National University, 2011. (cited on pages 72 and 73)

[170] Dr khu vu. https://physics.anu.edu.au/people/profile.php?ID=466. (cited on page 73)

[171] Scientific materials corp. http://www.scientificmaterials.com. (cited on page 73)

[172] J. Cognard. Adhesion to gold: A review. *Gold Bulletin*, 17(4):131–139, 1984. (cited on page 74)

[173] Australian national fabrication facility. http://anff-act.anu.edu.au. (cited on page 74)

[174] Comsol multiphysics modeling software. https://www.comsol.com/. (cited on pages 77, 93, 94, and 95)

[175] A.W. Snyder and J.D. Love. *Optical Waveguide Theory*. Springer US, 1983. (cited on page 78)

[176] P. K. Tien and R. Ulrich. Theory of prism–film coupler and thin-film light guides. *J. Opt. Soc. Am.*, 60(10):1325–1337, Oct 1970. (cited on pages 84 and 87)

[177] K.R. Harper. *Theory, design, and fabrication of diffractive grating coupler for slab waveguide*. PhD thesis, Brigham Young University, 2003. (cited on page 88)

[178] P. Bienstman. *Rigorous and efficient modelling of wavelength scale photonic components*. PhD thesis, University of Gent, 2001. (cited on pages 88, 90, and 91)

[179] P. Bienstman. *CAMFR manual*, 2007. (cited on pages 90 and 91)

[180] M. J. Sellars. *Ultra-High Resolution Laser Spectroscopy of Rare Earth Doped Solids*. PhD thesis, Australian National University, 1995. (cited on pages 103, 113, and 120)

[181] D.L. McAuslan. *Quantum Computing Hardware based on Rare-Earth-Ion Doped Whispering-Gallery Mode Resonators*. PhD thesis, University of Otago, 2011. (cited on pages 103 and 125)

[182] Helios nanolab^{TM} dualbeam^{TM}. http://www.fei.com/products/dualbeam/helios-nanolab. (cited on page 108)

[183] Fib-sem. https://www.embl.de/services/core_facilities/em/services/fibsem/. (cited on page 110)

[184] R.M. Macfarlane and R.M. Shelby. Measurement of optical dephasing of Eu^{3+} and Pr^{3+} doped silicate glasses by spectral holeburning. *Optics Communications*, 45(1):46 – 51, 1983. (cited on page 126)

[185] P.J. Van der Zaag, B.C. Schokker, Th. Schmidt, R.M. Macfarlane, and S. Vlker. Dynamics of glasses doped with rare earth ions: A study by permanent and transient hole-burning. *Journal of Luminescence*, 45(16):80 – 82, 1990. (cited on page 126)

[186] E. Miyazono, I. Craiciu, A. Arbabi, T. Zhong, and A. Faraon. Coupling erbium dopants in yttrium orthosilicate to silicon photonic resonators and waveguides. *Opt. Express*, 25(3):2863–2871, Feb 2017. (cited on page 126)

[187] Wyko nt9100 optical profiling microscope. http://www.veeco.com/pdfs/brochures/B506-Rev_A7-Wyko_NT_Series_Optical_Profilers-Brochure_(HiRes).pdf. (cited on page 130)

[188] nanoscale and quantum optics. http://photonics.caltech.edu/rareearth.html. (cited on page 131)

[189] Microchemicals GmbH. Photoresists, ancillaries, etchants, solvents, and technical support for all stages of microstructuring and lithography. (cited on page 131)